TÉCNICO LISBOA

Scaling and numerical analysis of non-isothermal sloshing for space propulsion

Pedro Afonso Duque Morgado Marques

Thesis to obtain the Master of Science Degree in

Aerospace Engineering

Supervisors: Prof. Luís Rego da Cunha de Eça
Prof. Miguel Alfonso Mendez

Examination Committee

Chairperson: Prof. Filipe Szolnoky Ramos Pinto Cunha
Supervisor: Prof. Luís Rego da Cunha de Eça
Members of the Committee: Prof. João Carlos de Campos Henriques
Dr. Alessia Simonini

October 2020

Acknowledgments

I would first like to thank my supervisors, Prof. Miguel Mendez and Prof. Luís Eça, for their guidance, and support in overcoming the numerous challenges that I encountered while working on this thesis. Also, a very special thanks to Alessia, who continuously helped me throughout this journey and pushed me to do my best the whole way through.

I am very thankful to Jorge Sousa. Without him I would not have been in VKI in the first place, and I would have missed out on a lot of new experiences and on meeting all the amazing people from the institute.

For my family and friends back home, I would like to express my deep gratitude for their patience and for their emotional support from far away. To my mother, especially, since she was the one to always push for me to go out and take on this challenge in Belgium. Finally, a very big thank you to my girlfriend, Sivan, with whom I spent several months during the lock-down, and who always gave me the motivation to push through the difficult times.

Resumo

O movimento de líquidos dentro de reservatórios é chamado 'sloshing'. Este fenómeno é de interesse para a indústria aeroespacial, dada a prevalência de sistemas de propulsão com combustíveis líquidos em aeronaves modernas. O deslocamento dos líquidos gera forças e momentos destabilizadores que devem ser compensados pelos sistemas de controlo de atitude. Adicionalmente, quando fluidos criogénicos são utilizados, as suas elevadas sensibilidades térmicas, aliadas ao movimento do líquido, promovem a transferência de calor entre as fases gasosa e líquida. Para condições críticas, observam-se grandes flutuações de pressão, e a estabilidade estrutural do tanque pode ser comprometida.

O objectivo deste trabalho foi estudar a problemática de 'sloshing' não-isotérmico e investigar se um modelo de laboratório de pequena-escala consegue reproduzir os fenómenos observados em tanques de combustíves criogénicos de foguetões modernos. A análise é realizada através de simulações numéricas com o software OpenFOAM. As taxas de amortecimento, posição da interface, forças e momentos gerados são analisados, e a semelhança no movimento é comparada entre ambas as instalações. O problema da destratificação térmica é estudado para diferentes campos térmicos iniciais, diferentes excitações externas e diferentes condições térmicas das paredes do tanque. Para condições de sloshing linear, o comportamento mecânico do escoamento, bem como a evolução termodinâmica do sistema, foram semelhantes para ambas as instalações. Contudo, observou-se que, apesar de a instalação em tamanho-real não ter sido muito afetada pela presença de fluxos-térmicos normais às paredes do tanque, o modelo em pequena-escala foi significativamente afetado, revelando diferenças nas evoluções da pressão e temperatura dos sistemas.

Palavras-chave: 'Sloshing', fluídos criogénicos, efeito da queda de pressão, destratificação térmica, CFD, OpenFOAM.

Abstract

The motion of liquids inside a reservoir is called sloshing. This phenomenon is of interest to the aerospace industry given the prevalence of liquid-based propulsion systems in modern spacecraft. The fluid displacement generates destabilizing forces and moments which must be compensated by the attitude control systems. Moreover, when cryogenic fluids are considered, their high thermal sensitivities coupled with the liquid motion causes thermal mixing to take place between the gas and liquid phases. For critical conditions, large pressure fluctuations are observed, and the structural stability of the tank can be compromised.

The aim of this work was to study the scaling laws of non-isothermal sloshing and investigate whether a small-scale laboratory model can reproduce the phenomena observed in the cryogenic stages of modern launch vehicles. This was done through Computational Fluid Dynamics simulations with OpenFOAM. The damping rates, interface position, sloshing forces and moments were analysed and similarity in the motion was compared between both facilities. The thermal destratification problem was studied for different initial thermal fields, different sloshing excitations and different thermal responses of the solid container walls. For planar sloshing conditions, the scaling approach yielded good similarity in terms of the flow dynamics as well as the thermodynamic evolution of the system. While the full-size facility was found to be less affected by the presence of wall-normal heat fluxes, the small-scale model was significantly impacted by this, leading to differences in the pressure and thermal evolutions of the systems.

Keywords: Sloshing, cryogenic fluids, pressure-drop effect, thermal destratification, CFD, OpenFOAM.

Contents

List of Figures

List of Tables

Nomenclature

Abbreviations and Acronyms

CFD Computational Fluid Dynamics.

DFT Discrete Fourier Transform.

FCT Flux-Corrected Transport.

MULES Multidimensional Universal Limiter for Explicit Solution.

TVD Total Variation Diminishing.

VKI von Karman Institute for Fluid Dynamics.

VOF Volume of fluid.

Greek symbols

α Thermal diffusivity coefficient.

β Volumetric thermal expansion coefficient.

δ_s Stokes boundary layer.

η Interface displacement.

γ Damping rate.

κ Surface curvature.

Λ Logarithmic decrement.

λ Bulk viscosity.

$\mathbb{T}$ Shear stress tensor.

$\mathfrak{B}$ Frequency offset parameter.

μ Dynamic viscosity coefficient.

ν Kinematic viscosity coefficient.

Ω Imposed frequency.

ω Natural frequency.

Φ Velocity potential function.

ρ Density.

σ Surface tension.

ξ Root of Bessel function derivative ($J'(\xi) = 0$).

Roman symbols

$\mathbb{I}$ Identity matrix.

$\mathbb{K}$ Kinetic energy.

$\mathbf{F}$ Force vector (F_x, F_y, F_z).

$\mathbf{g}$ Volumetric force vector.

$\mathbf{M}$ Moment vector (M_x, M_y, M_z).

$\mathbf{u}$ Velocity vector (u_x, u_y, u_z).

A_0 Excitation amplitude.

C_p Specfic heat capacity at constant pressure.

C_v Specfic heat capacity at constant volume.

e Internal energy.

g Gravitational acceleration.

H Sloshing tank total height.

h Liquid height inside tank.

I_s Specific impulse.

k Thermal diffusivity.

p Pressure.

R Sloshing tank radius.

R_s Ideal gas constant.

T Temperature.

Bo Bond number.

Co Courant number.

Fo Fourier number.

Fr Froude number.

Gr Grashof number.

Oh Ohnesorge number.

Pe Peclet number.

Re Reynolds number.

We Weber number.

Subscripts

bulk Liquid bulk.

gas Gas properties.

i Gas-liquid interface.

lid Sloshing tank lid.

liq Liquid properties.

ref Reference conditions.

sat Saturation conditions.

Chapter 1

Introduction

1.1 Framework

Liquid sloshing can be defined as the movement of the free liquid surface in a container or reservoir when subjected to a disturbance. This motion is associated with the displacement of a certain "sloshing mass" that produces forces and moments on the container's walls. These disturbances may be vibrations, acceleration changes, and pitch, roll or yaw motions.

This phenomenon is of particular interest to the aerospace industry given the great number of spacecraft which use liquid-based propulsion systems. These systems function by burning chemical propellants at high pressures, thus releasing large amounts of energy. Thrust is generated through the discharge of hot combustion products at high speeds through the nozzle located aft the combustion chamber. Figure 1.1 shows the schematic of a generic liquid propulsion system.

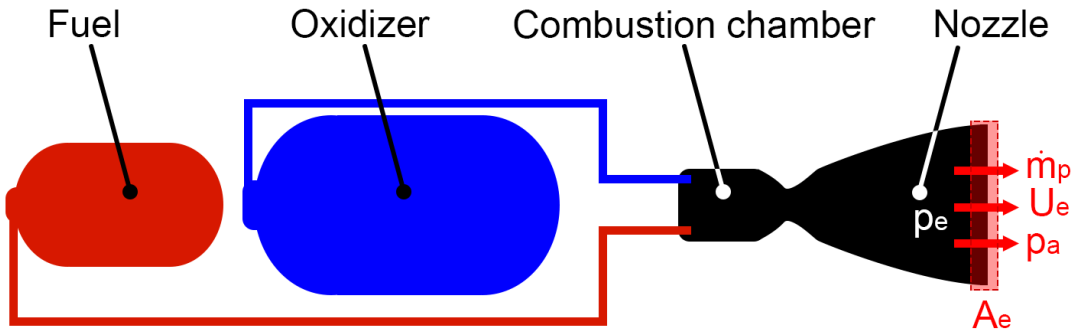

Figure 1.1: Schematic of a generic liquid based propulsion system. Adapted from [1].

Applying a momentum balance on the exit of the rocket's nozzle, the generated thrust can be obtained through Equation 1.1, where $\dot{m}_e$ is the mass flux of the propellant at the exit section, U_e is the velocity of the exhaust gases, A_e is the cross-sectional area of the nozzle at the exit section, p_e is the pressure at the exit section, and p_a is the ambient pressure [1].

$$F = \dot{m}_p U_e + A_e(p_e - p_a) \tag{1.1}$$

The impulse of the rocket $I(t)$ due to the engine's thrust can be calculated by integrating the generated force over time. This is given by Equation 1.2.

$$I(t) = \int_0^t F(t)dt \tag{1.2}$$

Furthermore, the specific impulse I_s provides a measure of the stored propulsive energy with respect to the corresponding fuel weight. High values for this parameter are desirable since they indicate that more energy is stored in the propellant, thus requiring a smaller fuel load and allowing for additional weight to be used in other areas of the spacecraft. For constant thrust, and constant propellant mass flux, the specific impulse is given by:

$$I_s = \frac{|F|}{g\dot{m}_\mathrm{p}}. \tag{1.3}$$

Although the exact value of the specific thrust is dependent on the operating conditions, it is nonetheless a useful measure to compare the performance of different propulsive systems. As a result, Table 1.1 shows the specific impulse, I_s, as well as the specific impulse at sea level, I_s (SL), of several rocket stages which use different propulsion solutions.

Table 1.1: Information regarding the propulsion systems used in several rocket stages

	Stage	**Oxidizer/Propellant**	**Kind**	I_s **[s]**	I_s **(SL) [s]**
Saturn V [2]	S-IC	LOx/RP-1	semi-cryogenic	304	265
	S-II	LOx/LH2	cryogenic	421	200
	S-IVB	LOx/LH2	cryogenic	421	200
Ariane 5 ECA [3]	EAP	Solid propellant	solid	275	250
	EPC	LOx/LH2	cryogenic	434	335
	ESC-A	LOx/LH2	cryogenic	446	-
Atlas V [4]	Booster	Solid propellant	solid	275	245
	CCB	LOx/RP-1	semi-cryogenic	338	311
	Centaur	LOx/LH2	cryogenic	451	-
Space shuttle [5]	Booster	Solid propellant	solid	269	237
	Orbiter	LOx/LH2	cryogenic	455	363

Of the presented spacecraft, the Ariane 5 ECA, and Atlas V launch vehicles are still currently in use for a wide range of applications such as communications, military, observation, among others [3, 4]. The space shuttle was retired in 2011 [5], and Saturn V had its last flight in 1973 [2]. The presented data shows that the combination of liquid hydrogen (LH_2) as propellant, and liquid oxygen (LOx) as oxidizer generates the highest specific impulse when compared to the other propulsive solutions. This explains why cryogenic fluids have become standard for space propulsion in recent years.

However, there are risks and challenges which must be overcome when adopting cryogenic propulsive solutions. Firstly, when ignited, hydrogen is known to react very violently in the presence of oxygen, causing very strong explosions if the amount of reactants is high [6]. Therefore, strong safety measures must be implemented to reduce the risk of hazardous handling of the propellant and oxidizer. Moreover,

the characteristic low saturation temperatures ($T_{sat} \sim 20K = -253.15^{\circ}$ C for H_2 at a pressure of ~ 1 bar) make long term storage complicated due to evaporation if residual heat fluxes are present outside the tank. In order to counter-act this issue, a great deal of thermal insulation and shielding must be employed, which adds to the complexity, cost and weight of the system.

During the propelled flight phase of the launcher, lateral sloshing is a critical motion exhibited by the fluids inside the cryogenic stages [7]. The cryogenic tanks can be full up to 95% [8], and the resulting fluid displacement generates destabilizing forces and moments, which must be counteracted by the attitude control system. In fact, there have been several instances throughout history where propellant sloshing led to complete or momentary loss of control in spacecraft.

An early example is the Apollo-11 Lunar Module in 1969. Sloshing of the remaining propellant induced an oscillatory motion onto the Lunar Module during the last seconds of the first lunar landing. This hampered the ability to control the module during the crucial landing manoeuvrer. As the propellant level decreased to about fifty percent, the fluid gained more space to slosh, yet retained enough mass to generate strong forces and moments, demanding harsher control requirements [9].

A more recent case took place on March 21st, 2007. During its second flight, the SpaceX Falcon-1 launcher lost control 2 minutes 10 seconds into the vehicle's second stage burn and, as a result, failed to reach orbit. After investigating the mission failure, it was found that propellant sloshing caused the oscillation. The LOx slosh frequency coupled with the thrust vectoring control system gradually amplified the vehicle's oscillations until flight control was completely lost [10].

Figure 1.2: Successful launch of a Falcon 1 rocket from the SpaceX launch site in Kwajalein Atoll, September 28, 2008 [10].

Another problematic point is related to the high thermal sensitivity of cryogenic fluids. Prior to launch, the cryogenic containers are pressurized from atmospheric conditions up to 3.1-3.3 bar [11, 12, 13]. This pressurization leads to the increase of the gas temperature in the fuel tank. Then, as the system evolves towards thermal equilibrium, the warmer gas exchanges heat with the container walls and with the liquid propellant leading to a thermally stratified field in the container. The exact shape of this thermal field depends on the pressurization method, its duration and the fluids used.

Figures 1.3a and 1.3b shows two examples of thermally stratified fields inside cryogenic containers after active pressurization with gaseous nitrogen (a), and oxygen (b). The data was obtained from

experimental measurements performed by Lacapere *et. al* (2009) [14] inside a cryostat with 19cm of radius and 800cm of height. The gas phase is characterized by a large temperature drop between the top of the container and the free surface, whereas the thermal gradient in the liquid is focused only in the region below the interface. Due to liquid sloshing the stratified field is disturbed leading to thermal mixing between the warmer gas and the colder liquid. The heat transfer rate between both fluids depends on their thermal properties and initial temperature, as well as the excitation conditions the container is subjected to.

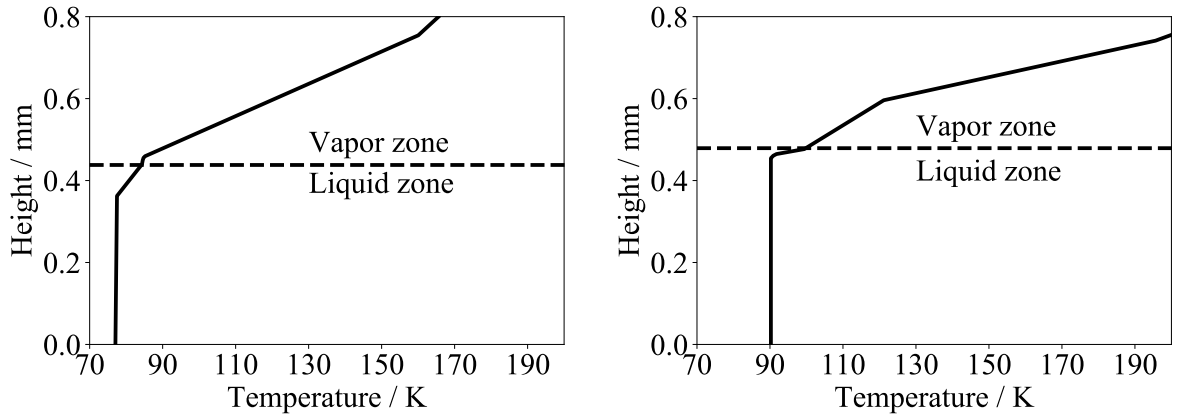

Figure 1.3: Initial stratification in the cryostat just before sloshing for LN_2 pressurized with GN_2 (a) and LOx pressurized with GOx (b) [14].

As a result of the mixing, the gas region cools down, decreasing its density. Consequently, the gas mass is no longer enough to maintain the current tank pressure, so this quantity must also decrease. This effect is accentuated by condensation effects between the vapour and liquid phases [14, 8, 15].

This phenomenon is often referred to, in the literature, as the 'pressure drop effect', and it has been observed to take place in several flights of the Ariane 4 and 5 launchers [13]. The magnitude of this drop depends on a series of factors, and it may cause several unwanted effects such as compromising the structural integrity of the propellant tank [8], and affecting the performance of cold gas thrusters, if they are used [16].

In addition to the previously mentioned effects, the presence of external heat fluxes (due to radiation, or thermal conduction within the rocket structure) must also be considered. These fluxes lead to the formation of wall normal temperature gradients in the container which cause the fluids to warm up, and liquid evaporation to take place at the contact line [17]. In isolation, these effects are associated with an increase in the tank pressure. However, if liquid sloshing is also present both effects must be accounted for in order to accurately determine the thermodynamic evolution of the system.

In summary, sloshing of cryogenic fluids is a flow phenomenon which causes adverse mechanical and thermodynamic effects in modern spacecrafts which requires further investigations.

1.2 Motivation and objectives

The goal for this work is to analyse the scaling laws of non-isothermal sloshing and investigate whether a small scale laboratory model is capable of reproducing the main phenomena encountered in a full-size cryogenic fuel tank. The analysis is carried out through CFD (Computational Fluid Dynamics) simulations with OpenFOAM. The focus is on understanding the role of sloshing in the thermal destratification process, and the effect that this has in the pressure evolution. Therefore, no phase change effects are considered in the computational models. This approach is identical to assuming that the container is partly filled with a cryogenic liquid, while using a non-condensable gas for the ullage pressurization.

The numerical study is carried out in two separate phases. First, the isothermal sloshing case is analysed in order to assess the scaling of the wave response between both facilities. The interface displacement, sloshing forces and moments are analysed both in the time and frequency domains, and numerical estimates are given for the damping rates of the systems.

Then, the non-isothermal problem is approached. This is also decomposed in two stages: first, thermal stratification simulations are performed in order to compare the similarity of this process between both facilities, and then the sloshing-induced mixing simulations are executed. In an effort to decrease the computational load, the container walls are not modeled in this analysis. Instead, two sets of boundary conditions, A and B, are considered in order to account for both extremes of wall heat transfer conditions. Case A assumes that the lateral walls are adiabatic, while case B assumes that these are at fixed temperatures, equal to the gas temperature T_{gas} in the portion initially in contact with the gas, and equal to T_{liq} in the portion initially in contact with the liquid. In both cases, the upper and the bottom walls of the tank are assumed at uniform temperature T_{gas} and T_{liq} respectively.

Chapter 2

Sloshing background

2.1 State of the Art

During the space race in the 1960s, a lot of work was developed by the National Aeronautics and Space Administration (NASA) concerning liquid sloshing in space vehicles. Bauer (1964) [18] and Abramson (1966) [19] developed a compendium of the work done up to that point regarding analytical and mechanical models to describe liquid sloshing for several container configurations. Furthermore, Abramson also compiled a large amount of experimental data with the aim of complementing and validating the theoretical models.

Regarding the existence of different sloshing regimes, Miles (1984) [20] developed a theoretical model to study the effect of the excitation parameters in the expected fluid response. The different sloshing regimes (planar, non-planar *swirl*, and chaotic) were found to depend on the frequency offset parameter $\mathfrak{B}$. This parameter is a measure of the proximity to resonance conditions, and is a function of the excitation amplitude, the excitation and natural frequencies, as well as the tank radius.

Moran (1994) [21] performed large scale experiments with LH_2 in a partly filled pressurized spherical tank. The goal was to study the pressure evolution in the container for different lateral sloshing conditions. The effect of the sloshing regime was studied, and it was found that while both chaotic and stable sloshing modes led to a pressure drop inside the tank, the chaotic motion had a much stronger effect on this phenomenon. The impact of using a non-condensable gas for the pressurization was also tested. It was found that for these conditions, with gaseous Helium (GHe) as the non-condensable pressurant, the container's pressure would increase during the sloshing experiment. This was mostly attributed to the presence of environmental heat fluxes surrounding the tank. Moreover, the effect of the ullage volume was studied, and it was found that as the liquid fill level increases, so does the pressure drop since initially there is less available vapor mass to maintain the tank pressure.

The pressure drop effect in lateral sloshing was studied by Lacapere *et. al* (2009) [14] using LN_2 and LOx to model the behaviour of cryogenic sloshing at a smaller scale. The pressure drop was verified, and thermal mixing could be observed in the vicinity of the liquid-vapor interface. Computational simulations were also performed to model the flow, and showed good agreement with the experimental results.

Himeno *et. al* (2011) [15] performed a series of experiments on the pressure drop phenomenon under different conditions. Different degrees of excitation were used in order to test their effect on the pressure drop and on the free surface shape. Physical damping devices were introduced to limit the sloshing motion and, consequently, inhibit the pressure drop effect. Moreover, similarly to what was done in the work of Moran (1994), the use of Helium as a non-condensable gas was also tested and proved to strongly mitigate the measured pressure drop.

Arndt (2011) [8] further investigated the pressure drop for lateral sloshing of LN_2 near the first natural frequency with different tank pressurization methods. Passive pressurization was compared against active methods using gaseous nitrogen (GN_2) and helium (GHe). The temperature stratification generated by the tank pressurization proved to be crucial in determining the pressure evolution. For the case of GHe pressurization, different partial pressures of helium were tested. From this, Arndt (2011) found that as the partial pressure of helium increased, the tank's pressure evolution became less sensitive to sloshing. In fact, from a certain amount of GHe, the pressure drop effect was able to be completely neutralized. These results are analogous with LH_2 and may be scaled up to analyse data from full size facilities.

Still in this thesis, Arndt (2011) experimentally measured the damping ratio for different fill levels and found good agreement with the theoretical expressions presented in Abramson (1966) [19]. Following on the conclusions taken by Arndt (2011) [8], van Foreest (2010) [22] built a 1D model capable of predicting the pressure drop and thermal distribution inside the liquid phase. The 1D model was compared to both experimental results and CFD simulations, and overall good agreement was found. Later, this model was used by Montsarrat (2017) [13] to understand the pressure and thermal evolution in several flights of the Ariane 5 ECA launch vehicle.

2.2 The pressure drop effect

The pressure drop effect is a well-documented problem that takes place within cryogenic stages of launch vehicles during the initial propelled flight phase. There are two main triggers for this phenomenon to take place:

1. Tank pressurization prior to launch, which causes a thermal stratification to set in the container.
2. Flight perturbations, or trajectory changes which induce oscillations in the cryogenic container's motion. This results in the unwanted displacement of the liquid mass known as liquid sloshing.

The presence of this initial thermal field coupled with liquid sloshing leads to thermal mixing inside the cryogenic stage. The colder bulk liquid mixes with the warmer gas, leading to a general cooling down of this region and promoting condensation of the vapour phase. Both these mechanisms contribute to a decrease of the tank pressure, however the aim of this thesis is study only the impact of the sloshing-induced thermal mixing.

The magnitude of this pressure drop is dependent on a series of factors such as the pressurization technique, the type of pressurant gas used, the excitation conditions, and the volume of gas present

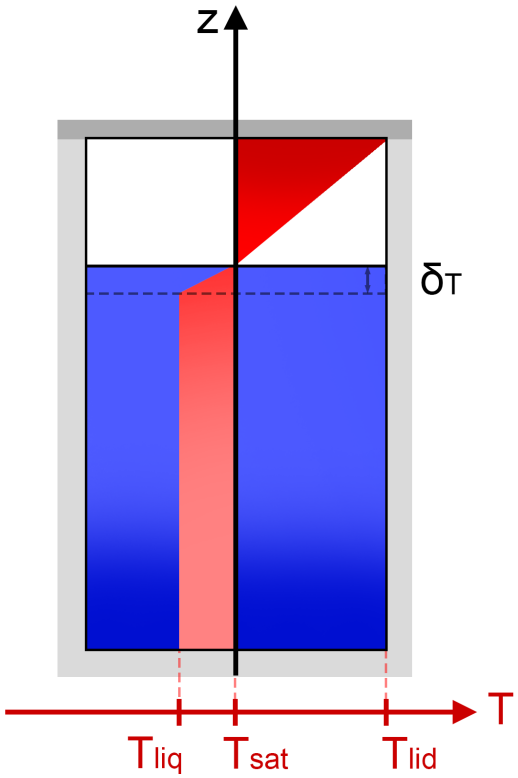

Figure 2.1: Schematic illustration of thermal stratification that sets in the fluids after the pressurization of the container.

within the tank [8, 21].

Pressurization methods

- **Passive pressurization:** Tank pressure increases due to presence of residual heat fluxes that lead to expansion of the vapour phase. Takes a long time for the required pressure to be achieved in the container. Consequently there is more time for the temperature to be transported along the container, meaning that the thermal gradient in the liquid will be smoother along a larger distance δ_T under the interface. As a result, the thermal mixing effect will be less severe. Thus, the pressure drop effect is reduced.

- **Active pressurization with vapour of the same species as the liquid:** Tank pressurization achieved by the introduction of gas from an external reservoir. Fast method to achieve the required pressure. As a result, there will not be as much time for the temperature to be transported throughout the liquid under the interface. This results in a very sharp thermal gradient along a small distance δ_T. This sharp thermal gradient leads to very effective heat transfer promoted by liquid sloshing, and thus to a larger pressure drop.

- **Active pressurization with non-condensible gas:** Identical to the previous method, however the use of a non-condensible gas reduces the pressure drop effect since condensation effects should not be present. Thermal mixing will only be responsible for cooling down the vapour phase through heat transfer. This is the situation that is modeled in the computational section of this thesis.

Ullage volume

The proportion of gas to liquid volume in the cryogenic container can be crucial in assessing the magnitude of the pressure drop [21]. For large ullage volumes, the pressure drop has been observed to be more severe. This is attributed to the fact that there is less vapour mass to maintain the tank pressure.

Excitation conditions

As discussed in Section 2.7, different sloshing wave responses can be obtained by varying the imposed excitation conditions. Stable wave modes are characterized by a predictable free surface motion, whereas unstable modes lead to violent and dynamic wave responses.

Experimental observations show that high amplitude chaotic slosh responses increase the pressure drop effect when compared to stable wave modes [21] . These cause a more significant circulation of the subcooled bulk liquid towards the interface, which has the consequence of increasing the thermal mixing, thus cooling down the vapor region more efficiently and increasing the condensation rate.

2.3 Mathematical modeling

The sloshing problem analysed in this work is the lateral excitation of a partially filled cylindrical reservoir which has its axis aligned with the gravitational acceleration. Consider the cylinder to have radius R, fill level h, and total height H.

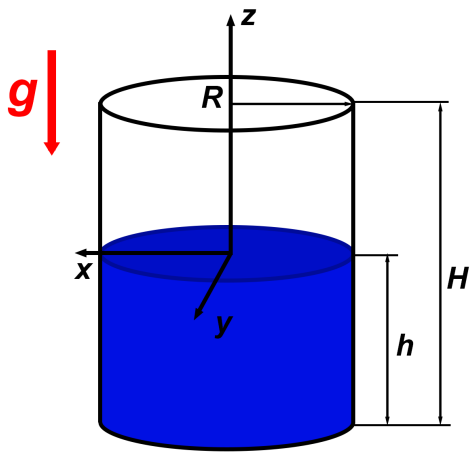

Figure 2.2: Partly filled cylinder of radius R, fill height h, and total hieght H [23]

For a lateral harmonic excitation with amplitude A_0 and imposed frequency Ω, the corresponding tank position, velocity and acceleration are determined by Equations 2.1, 2.2 and 2.3, respectively.

$$X_0(t) = A_0 \sin(\Omega t) \tag{2.1}$$

$$\dot{X}_0(t) = A_0 \Omega \cos(\Omega t) \tag{2.2}$$

$$\ddot{X}_0(t) = -A_0 \Omega^2 \sin(\Omega t) \tag{2.3}$$

Thus, lateral sloshing may be modeled through two possible methods:

1. Impose excitation through rigid body motion of the container. An inertial reference frame is considered, and the fluid velocity at the container walls must match the velocity of the walls themselves. This is the method employed in the work of Hansinger (2016) [24] and Jaguer (2019) [25].

2. Impose excitation in a non-inertial reference frame where the container is considered stationary. Here, sloshing is induced by lateral acceleration changes given by Equation 2.3. This is the approach followed by Agui (2015) [26], and Kartuzova (2018) [27]. It is implemented by considering an additional source term in the momentum equations which corresponds to the lateral force the container exerts on the fluid when it moves.

Both approaches were tested and implemented in OpenFOAM, and a comparison of both methods is presented in Section 4.3.

2.4 Governing equations

This section is devoted to explaining the governing equations and relevant boundary conditions for the non-isothermal sloshing problem. The expressions derived below provide the fundamental basis for the derivation of the scaling laws and the definition of the dimensionless groups controlling the flow similarity. In the most general sense, fluid motion problems can be described by three transport equations that are given through the conservation of mass, conservation of momentum and conservation of energy.

For the work developed in this master's thesis, the problem is divided in two steps. First, isothermal simulations were performed with the goal of studying the scaling of the sloshing dynamics and assessing the effect of the numerical discretization in this context. Then, non-isothermal simulations were conducted in order to evaluate the scaling of the thermal destratification process and the pressure evolution of the system. Since the governing equations and the physical assumptions are different for both cases, they are presented separately in this section.

2.4.1 Isothermal sloshing

For isothermal sloshing, the fluids are considered to be incompressible. Thus, the density of both phases is assumed to be constant, ρ = cte. As a result, for this situation, the differential form of the mass conservation equation is simplified into the following [28]:

$$\nabla \cdot \mathbf{u} = \frac{\partial u_x}{\partial x} + \frac{\partial u_y}{\partial y} + \frac{\partial u_z}{\partial z} = 0. \tag{2.4}$$

Where $\mathbf{u} = (u_x, u_y, u_z)$ is the flow velocity vector. The momentum conservation equation is derived from Newton's second law of motion, which relates the rate of change of momentum of a fluid with the sum of forces acting on the control volume. For a generic fluid system, the external forces can act on the boundaries of the control volume, such as pressure and shear stresses, or throughout the volume itself, which is the case for gravity.

The differential form of the incompressible momentum balance is given by Equation 2.5, where p is the pressure, $\mathbb{T}$ is shear stress tensor, and $\mathbf{g}$ is the imposed acceleration on the fluid. The two terms on the left hand size represent the temporal and spatial rate of change of momentum due to convective transport, respectively. The term $\nabla \cdot p$ represents the normal stresses applied on the fluid element due to pressure, $\nabla \cdot \mathbb{T}$ accounts for viscous dissipation/diffusion of momentum and $\rho\mathbf{g}$ is the source term for volumetric forces.

$$\rho\frac{\partial \mathbf{u}}{\partial t} + \rho\mathbf{u}(\nabla \cdot \mathbf{u}) = -\nabla p + \nabla \cdot \mathbb{T} + \rho\mathbf{g} \tag{2.5}$$

For incompressible Newtonian fluids with constant viscosity μ, the shear stress tensor, $\mathbb{T}$, is directly related to the local velocity gradients, through Equation 2.6 [29, 30].

$$\nabla \cdot \mathbb{T} = \nabla \cdot \left(\mu[\nabla\mathbf{u} + (\nabla\mathbf{u})^{\mathsf{T}}]\right) = \mu\nabla^2\mathbf{u} \tag{2.6}$$

The $\rho\mathbf{g}$ term represents the volumetric forces which act on the flow. Depending on the modeling approach for the sloshing excitation, different acceleration components can be considered within $\mathbf{g}$. For the inertial reference frame approach, $\mathbf{g} = (0, 0, g)^{\mathsf{T}}$, meaning only the gravitational acceleration is considered to act on the flow. Then, the excitation is established by displacing the domain through rigid body motion and correcting the equations to account for this displacement. However, for the non-inertial reference frame approach, the volumetric forces account for the change in lateral acceleration of the domain. Thus, in these conditions, $\mathbf{g} = (\ddot{X}_0, 0, g)^{\mathsf{T}}$, where $\ddot{X}_0$ is defined in Equation 2.3.

The above equations are valid for both phases, however boundary conditions are required at the interface in order to establish compatibility in the motion and in the applied stresses. Thus, the velocity of both fluids at this boundary must match the velocity of the free surface itself, and the pressure difference between both phases must be balanced with surface tension. This is established through the Young-Laplace equation [31]:

$$\Delta p = p_{\text{liq}} - p_{\text{gas}} = -\sigma\kappa. \tag{2.7}$$

Where Δp is the pressure difference between the liquid and gas phases, σ is the surface tension, and κ is the free surface curvature. Moreover, no-slip boundary conditions are assumed for the velocity at the tank walls.

2.4.2 Non-isothermal sloshing

2.4.2.1 Governing equations for the compressible gas phase

The non-isothermal sloshing case requires a different treatment for the gas and liquid phases. The gas phase is modeled as being compressible, through the ideal gas law:

$$p = \rho R_s T. \tag{2.8}$$

Where, R_s is the ideal gas constant and T is the flow temperature. The compressible mass and momentum balance equation must be considered for the gas phase:

$$\frac{\partial \rho}{\partial t} + \nabla \cdot (\rho \mathbf{u}) = 0 \tag{2.9}$$

$$\frac{\partial}{\partial t}(\rho \mathbf{u}) + \mathbf{u}(\rho \nabla \cdot \mathbf{u}) = -\nabla p + \nabla \cdot \mathbb{T} + \rho \mathbf{g}. \tag{2.10}$$

For these conditions, $\nabla \cdot \mathbf{u} \neq 0$ and the viscous stress tensor $\mathbb{T}$ takes the form [29]:

$$\mathbb{T} = \mu \left[\nabla \mathbf{u} + (\nabla \mathbf{u})^T \right] + \left(\left[-\frac{2}{3}\mu + \lambda \right] (\nabla \cdot \mathbf{u}) \right) \mathbb{I}. \tag{2.11}$$

Where λ is the bulk viscosity of the fluid and $\mathbb{I}$ is the identity matrix. According to Bird et. al (2006) [32], the bulk viscosity term can be neglected, hence simplifying the expression in order to depend purely on the velocity field as well as the $(-\frac{2}{3}\mu)$ term, which is commonly referred to as the dilatation viscosity [29].

The total fluid energy can be decomposed in three main components: internal (e), kinetic ($\mathbb{K}$), and potential. Thus, if potential energy effects are treated as the work done by body forces [33], the rate of change of total energy in the control volume only takes into account the internal and kinetic components. The flow of energy through the control volume boundaries is possible due to the presence of external heat fluxes or due to the application of work involving body and surface forces. Thus, the total energy conservation equation is written in differential form in Equation 2.12.

$$\frac{\partial(\rho e)}{\partial t} + \nabla \cdot (\rho \mathbf{u} e) + \frac{\partial(\rho \mathbb{K})}{\partial t} + \nabla \cdot (\rho \mathbf{u} K) = \nabla(k \nabla T) + \nabla \cdot (\mathbb{T} \cdot \mathbf{u}) - \nabla \cdot (p\mathbf{u}) + \rho \mathbf{g} \cdot \mathbf{u} \tag{2.12}$$

Where k is the thermal conductivity of the fluid. For sloshing applications, the kinetic energy contribution can be neglected [8, 27], and introducing the ideal gas relation between internal energy and temperature, $\partial e = C_v \partial T$ [34], the thermal energy transport equation is retrieved:

$$\frac{\partial}{\partial t}(\rho C_v T) + \nabla \cdot (\rho C_v \mathbf{u} T) = \nabla(k \nabla T) + \nabla \cdot (\mathbb{T} \cdot \mathbf{u}) - \nabla \cdot (p\mathbf{u}) + \rho \mathbf{g} \cdot \mathbf{u}. \tag{2.13}$$

Where C_v is the specific heat capacity at constant volume.

2.4.2.2 Governing equations for the incompressible liquid phase

On the other hand, the liquid phase is still modeled as being incompressible. However, the Boussinesq approximation is introduced in order to account for thermally-induced density variations in the liquid. The core idea of this model is that density changes produce negligible difference in terms of inertia, however significant variations are expected in terms of buoyancy:

$$\rho = \rho_0[1 - \beta(T - T_0)] \text{ , with } \beta = -\frac{1}{\rho}\left(\frac{\partial \rho}{\partial T}\right)_p. \tag{2.14}$$

Where, ρ_0 is the density at reference temperature T_0 and β is thermal expansion coefficient. The

mass conservation balance retains the form of the continuity equation shown in Equation 2.4 but the buoyancy term of the incompressible momentum balance is modified:

$$\rho_0 \frac{\partial \mathbf{u}}{\partial t} + \rho_0 \mathbf{u}(\nabla \cdot \mathbf{u}) = -\nabla p + \mu \nabla^2 \mathbf{u} + \rho_0 [1 - \beta(T - T_0)]\mathbf{g}. \tag{2.15}$$

The thermal energy transport equation is simplified by removing the spatial and temporal dependency on the density, by neglecting the compressive and shear work done on the fluid by the $\nabla \cdot (p \cdot \mathbf{u})$ and $\nabla \cdot (\mathbb{T} \cdot \mathbf{u})$ terms, respectively:

$$\rho \frac{\partial}{\partial t}(C_v T) + \rho \nabla \cdot (C_v \mathbf{u} T) = \nabla (k \nabla T) + \rho \mathbf{g} \cdot \mathbf{u}. \tag{2.16}$$

The $\rho \mathbf{g} \cdot \mathbf{u}$ term represents the work done by volumetric forces. When the sloshing motion is modeled in the inertial reference frame, this quantity is neglected, since only the gravitational acceleration acts on the fluid. However, for the non-inertial reference frame approach, this term is included in the thermal energy transport equation in order to account for the changes in lateral acceleration that the fluid experiences.

2.4.2.3 Boundary conditions

The kinematic and dynamic boundary conditions for the interface are retained from the isothermal case, and the no-slip boundary condition for the velocity is also considered. Moreover, the temperature of the free surface is assumed to be at saturation conditions, $T_{\text{liq}} = T_{\text{gas}} = T_{\text{i}} = T_{\text{sat}}$. Therefore, the required pressurization level to achieve a certain interface temperature can be computed through the Clausius-Clapeyron law [34]:

$$\ln\left(\frac{p}{p_0}\right) = \frac{\Delta h_v}{R_s}\left(\frac{1}{T_{\text{sat},0}} - \frac{1}{T_{\text{sat}}}\right). \tag{2.17}$$

Where p and p_0, respectively, are the tank pressure after and before the pressurization stage, T_{sat} and $T_{sat,0}$, respectively, are the saturation temperature after and before pressurization, Δh_v is the latent heat of vaporization, and R_s is ideal gas constant for the pressurant.

Phase change effects are not considered in the modeling of the non-isothermal analysis since the goal of this work is to understand purely the role of sloshing in the thermal destratification problem. Nonetheless, the presence of condensation or evaporation can be qualitatively assessed by monitoring the temperature of the interface and relating it to the Clausius-Clapeyron equation. For example, if the interface temperature decreases, in order to remain in equilibrium conditions, the pressure of the vapour phase must decrease, promoting condensation to take place in the ullage. On the other hand, an increase in T_i is associated with a rise in vapour pressure, which should be established through evaporation of the liquid.

2.5 Linearised incompressible potential flow theory

This section is devoted to the introduction of simplified models for liquid sloshing. The goal of these approaches is to simplify the set of governing equations by imposing several restrictions on the problem, thus allowing for a clearer understanding of the mechanics and key parameters involved. This analysis is very important in understanding the frequency response of the sloshing waves when lateral excitation are applied.

In the linearised theory of liquid sloshing, flow irrotationality is assumed, $\nabla \times \mathbf{u} = 0$. This property coupled with the incompressible nature of the fluid, allows the velocity field to be described through a potential function Φ.

$$\nabla \Phi = \mathbf{u} \tag{2.18}$$

The complete set of considerations for the linearised potential model is presented below:

1. Irrotational flow: $\nabla \times \mathbf{u} = 0$
2. Incompressible fluid: ρ = constant $\Rightarrow \nabla \cdot \mathbf{u} = 0$
3. Small displacements and velocities
4. Gravity-dominated flow
5. Rigid cylindrical container walls
6. Harmonic container oscillation: $X_0(t) = A_0 \sin(\Omega t)$

Applying these conditions to the momentum balance of Equation 2.5 yields the linearised potential equation of motion (Equation 2.19), where g is the gravitational acceleration. The full derivation is shown in Appendix A.2.

$$\frac{\partial \Phi}{\partial t} + \frac{p}{\rho} - gz + \ddot{X}_0 r \cos(\theta) = 0 \tag{2.19}$$

2.5.1 Velocity potential function

The velocity potential Φ is calculated in cylindrical coordinates by writing it as a product of functions of its independent variables [35]:

$$\Phi = f_1(r) f_2(\theta) f_3(z) T(t). \tag{2.20}$$

The mathematical expression for Φ is computed with by solving the continuity equation, and by applying the problem's boundary conditions:

- Continuity equation for potential flow: $\nabla^2 \Phi = 0$
- Zero velocity normal to the tank's side walls: $\left(\frac{\partial \Phi}{\partial r}\right)_{r=R} = 0$

- Zero velocity normal to the tank's bottom wall: $\left(\frac{\partial \Phi}{\partial z}\right)_{z=-h} = 0$
- At the liquid's free surface, consider that the normal z component of the fluid velocity is equal to the normal component of the velocity of the surface itself: $\frac{\partial z}{\partial t} = -\left(\frac{\partial \Phi}{\partial z}\right)_{z=0}$

Thus, the velocity potential function is given by Equation 2.21. The complete derivation is presented in the work of Ibrahim (2005) [36].

$$\Phi(r,\theta,z,t) = \sum_{m=0}^{\infty}\sum_{n=1}^{\infty} \alpha_{mn}(t)\cos(m\theta)J_m\left(\frac{\xi_{mn}r}{R}\right)\frac{\cosh\left[\xi_{mn}(z+h)/R\right]}{\cosh\left(\xi_{mn}h/R\right)} \tag{2.21}$$

Where m, n are parameters that define the sloshing mode, J_m is the Bessel function of the m^{th} order, ξ_{mn} is the n^{th} zero of the first derivative of the m^{th} order Bessel function (i.e. $J'_m(\xi_{mn}) = 0$), and $\alpha_{mn}(t)$ is a temporal function, that is determined through the imposed excitation parameters. This result highlights the fact that the sloshing response is given by an infinite sum of harmonic modes. The following subsections will provide further insight on the way the excitation conditions lead to different wave responses.

2.5.2 Natural frequencies

Two-dimensional free surface oscillations in closed cylindrical containers can be considered as standing waves between two walls. As a result, the calculation of the natural sloshing frequencies is crucial in understanding the expected motion.

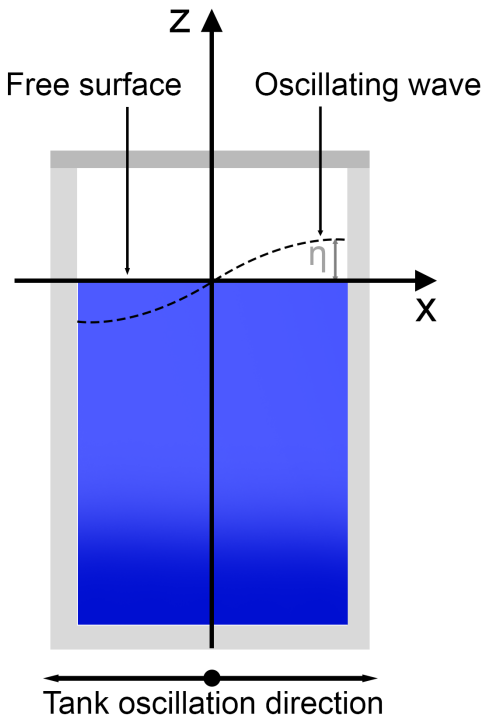

Figure 2.3: Schematic illustration of a sloshing standing wave (adapted from [23])

For a cylindrical container with radius R, filled with liquid at height h, subjected to a lateral harmonic

excitation, the natural frequencies of the linear sloshing problem are given by Equation 2.22 [36]. The derivation of this expression is shown in Appendix A.3.

$$\omega_{mn}^2 = \left(\frac{g\xi_{mn}}{R} + \frac{\sigma}{\rho}\frac{\xi_{mn}^3}{R^3}\right)\tanh\left(\frac{\xi_{mn}h}{R}\right) \tag{2.22}$$

For gravity-dominated sloshing, $g\xi_{mn}/R \gg \sigma\xi_{mn}^3/\rho R^3$, meaning that the natural frequencies can be considered independent of the fluid properties. Moreover, if the fill level is such that $h/R \gg 1$, they become independent of this parameter as well. Thus, for highly-filled containers under normal gravity conditions the natural sloshing frequencies are simply given by:

$$\omega_{mn}^2 = \frac{g\xi_{mn}}{R}. \tag{2.23}$$

Table 2.1 shows the values of the dimensionless natural frequencies $\omega_{mn}^* = \omega_{mn}(gR)^{-1/2}$, as well as the zeros ξ_{mn} for different sloshing modes (m, n).

Table 2.1: Zeros ξ_{mn} for the first derivative of the m^{th} order Bessel function of the first kind, and dimensionless sloshing frequencies ω_{mn}, for the (m, n) sloshing modes.

ξ_{mn}		m				
		0	**1**	**2**	**3**	**4**
n	**0**	0	0	0	0	0
	1	3.832	1.841	3.054	4.201	5.318
	2	7.016	5.331	6.706	8.015	9.282
	3	10.174	8.536	9.970	11.346	12.682

ω_{mn}^*		m				
		0	**1**	**2**	**3**	**4**
n	**0**	0	0	0	0	0
	1	1.957	1.357	1.748	2.050	2.306
	2	2.649	2.309	2.590	2.831	3.047
	3	3.190	2.922	3.157	3.368	3.561

2.5.3 Sloshing modes

The free surface shape η for each (m, n) mode in planar sloshing is given by Equation 2.24. This expression is obtained by writing Equation 2.19 in free vibration conditions around the initial undisturbed interface (z = 0) and by inserting the potential definition from Equation 2.21. The potential solution is assumed to be of the form $\Phi \sim \Phi e^{i\omega_{mn}t}$, where i is the imaginary unit [36].

$$\eta_{mn}(r, \theta, t) = i\omega_{mn}\alpha_{mn}\cos(m\theta)J_m\left(\frac{\xi_{mn}r}{R}\right)e^{i\omega_{mn}t}. \tag{2.24}$$

Expanding the complex exponential argument in the form $e^{i\omega_{mn}t} = \cos(\omega_{mn}t) + i\sin(\omega_{mn}t)$ allows for the determination of the real solution only. Furthermore, with the goal of only visualizing the free surface shapes for the different sloshing modes, the terms that do not depend on spatial or temporal coordinates are grouped together: $A_{mn} = \omega_{mn}\alpha_{mn}$.

$$\mathrm{Re}(\eta_{mn}) = -A_{mn}\cos(m\theta)J_m\left(\frac{\xi_{mn}r}{R}\right)\sin(\omega_{mn}t). \tag{2.25}$$

Figure 2.4 shows the expected surface shape for different sloshing modes (m, n). The number of waves in the tangential direction is determined by m, whereas the number of radial waves is determined by n. Moreover, the free surface's radial profile is determined exclusively by the shape of the m^{th} order

Bessel function of the first kind.

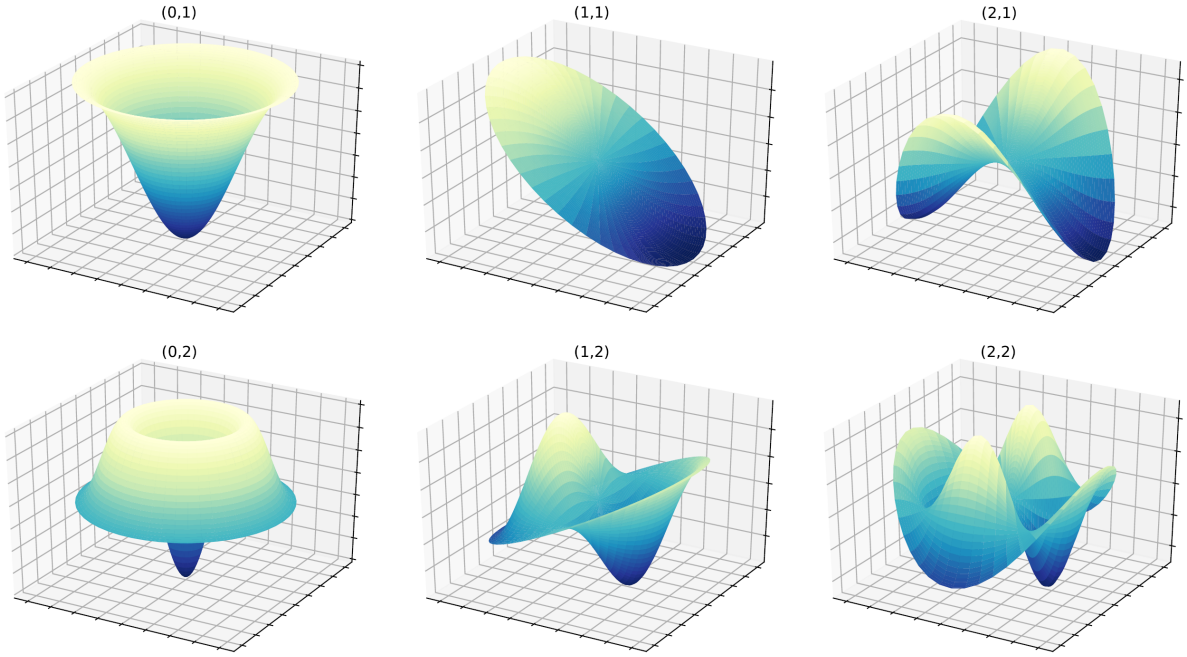

Figure 2.4: Free surface shape for different sloshing modes (m, n). Figures generated in Python by inserting different (m, n) values in Equation 2.25.

From Table 2.1, the lowest wave mode that can be excited in lateral sloshing conditions is the first asymmetrical one $m = n = 1$. This mode is characterized as an approximately flat wave that moves along with the direction of excitation. Observations on the initial propelled phase of launch vehicle flights show that this $(1, 1)$ mode is the primary fluid response in cryogenic stages as the spacecraft ascends through the atmosphere [14, 8, 13, 37]. As such, the focus of this work will be on sloshing excitations close to this natural frequency, ω_{11}.

2.5.4 Forced lateral vibration

This subsection presents the potential solutions for the free surface displacement and sloshing force in lateral excitation conditions. These quantities are later used as a form of comparison with the numerical results.

The velocity potential of the first asymmetrical sloshing mode, derived in Appendix A.4, is given by Equation 2.26.

$$\Phi(r,\theta,z,t) = \sum_{n=1}^{\infty} \frac{2R}{(\xi_{1n}^2 - 1)} \frac{A_0\Omega^3}{(\omega_{1n}^2 - \Omega^2)} \frac{J_1(\xi_{1n} r/R)}{J_1(\xi_{1n})} \frac{\cosh\left[\xi_{1n}(z+h)/R\right]}{\cosh\left(\xi_{1n} h/R\right)} \cos(\theta)\cos(\Omega t) \tag{2.26}$$

Free surface displacement

For forced lateral excitations, the free surface equation of motion is written as:

$$\left(\frac{\partial \Phi}{\partial t} - \frac{\sigma\kappa}{\rho}\right)_{z=0} - g\eta = -\ddot{X}_0 r\cos(\theta). \tag{2.27}$$

Neglecting surface tension effects, and inserting the velocity potential definition in the expression above allows for the determination of the free surface displacement for the first asymmetrical sloshing mode.

$$\eta(r,\theta,t) = \frac{A_0\Omega^2\cos(\theta)\sin(\Omega t)}{g}\left(\sum_{n=1}^{\infty}\frac{2R\Omega^2}{(\xi_{1n}^2-1)(\omega_{1n}^2-\Omega^2)}\cdot\frac{J_1(\xi_{1n}r/R)}{J_1(\xi_{1n})}+r\right) \tag{2.28}$$

Lateral sloshing force

The pressure on the walls due to liquid sloshing is obtained by solving Equation 2.19 with respect to p. Then, the force applied on the container is obtained by integrating the pressure distribution along the walls.

$$F_x = \int_{\theta=0}^{\theta=2\pi}\int_{z=-h/2}^{z=0} p(r=R)\cdot R\cos(\theta)dzd\theta \tag{2.29}$$

For the problem of lateral liquid sloshing, one is typically more concerned with the lower modes since these are achieved at lower excitation frequencies. The most relevant case is the first asymmetric mode since for symmetric waves the resulting force is zero [23], [8]. As such, for lateral excitation conditions and $m = 1$ [36]:

$$F_x = \rho\pi R^2 hX_0\Omega^2\sin(\Omega t)\left[1+\sum_{n=1}^{\infty}\frac{1}{\xi_{1n}h}\frac{2R\Omega^2}{(\xi_{1n}^2-1)(\omega_{1n}^2-\Omega^2)}\tanh\left(\xi_{1n}\frac{h}{R}\right)\right]. \tag{2.30}$$

It should be reiterated that this analysis concerns only linear sloshing, which is valid for flow oscillations very far from resonance conditions. Once the first natural frequency is reached, the liquid motion becomes chaotic or the planar waves turn into a swirl motion [8]. The topics regarding the different sloshing regimes (planar, non-planar and chaotic) are covered in Section 2.7.

2.6 Equivalent mechanical approach

Liquid sloshing dynamics can be described through equivalent mechanical models. These approximate the oscillating fluid mass as spring-mass or pendulum-mass systems. The simpler mathematical expressions used in this approach allow for their implementation in spacecraft control systems [38, 39]. Moreover, unlike the classical potential analysis, these models allow for the consideration of viscous effects in the sloshing response.

Mechanical models consider that the total fluid mass, m, is composed by a fixed mass, m_0, alongside several masses, m_n, which are excited during sloshing.

$$m = m_0 + \sum_{n=1}^{\infty} m_n \tag{2.31}$$

For the first asymmetrical sloshing mode $m = 1$, the sloshing masses are given as a function of the

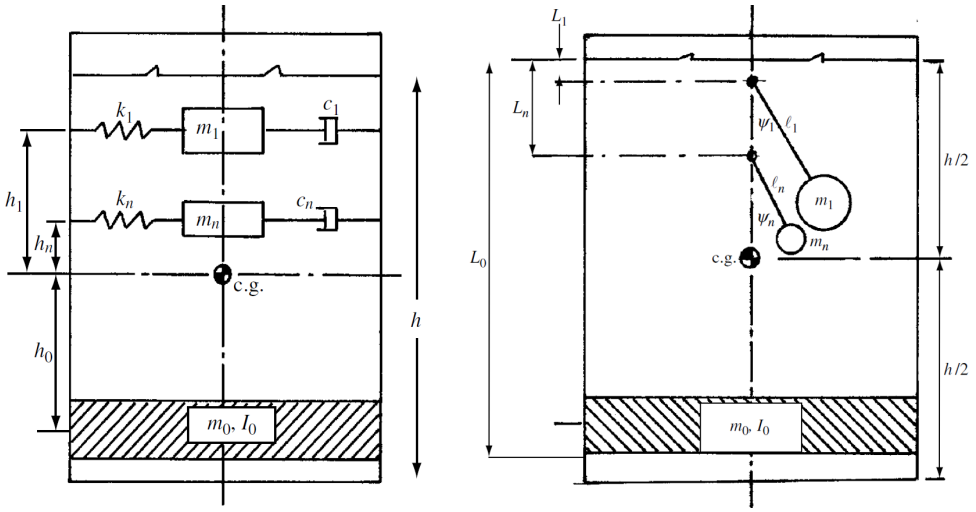

Figure 2.5: Schematic illustration of both equivalent mechanical sloshing models: spring-mass (left) pendulum-mass (right) systems [36]

geometry as well as the excitation conditions [38]:

$$m_n = m\frac{2R\tanh(\xi_{1n}h/R)}{\xi_{1n}h(\xi_{1n}^2-1)}. \tag{2.32}$$

Both the spring-mass and pendulum-mass approaches are equivalent and provide identical results. However, it should be noted that, similarly to the potential analysis discussed in the previous section, these models are only valid for linear sloshing, and for the first asymmetrical mode, $m = 1$.

Spring-mass system

The equation of motion for the nth spring is given by the second order ODE (ordinary differential equation) shown in Equation 2.33.

$$m_n\ddot{x}_n = -k_n x_n - d_n\dot{x}_n + F(t) \tag{2.33}$$

Where $k_n = m_n\omega_{1n}^2$ is the spring's stiffness, $d_n = 2m_n\gamma\omega_{1n}$ is the damping rate, γ is the damping ratio, and $F(t)$ is the excitation force, which in lateral sloshing conditions is given by:

$$F(t) = m_n A_0\Omega^2\cos(\Omega t). \tag{2.34}$$

For the first asymmetric sloshing mode, the damping ratio, γ, is given by the empirical correlation presented in Equation 2.35, where ν is the liquid's kinematic viscosity, and C_1, n_1 are parameters that depend on the problem's geometry. For a closed cylindrical container without baffles, $C_1 = 0.79$ and $n_1 = 1/2$ [19].

$$\gamma = C_1\left(\frac{\nu}{R^{3/2}g^{1/2}}\right)^{n_1}\left(1+\frac{0.318}{\sinh(\xi_{1n}h/R)}\left(1+\frac{1-h/R}{\cosh(\xi_{1n}h/R)}\right)\right) \tag{2.35}$$

The solution of Equation 2.33 is given by the superposition of the homogeneous solution x_{n_h} with the

particular one x_{n_p}.

$$x_n(t) = x_{n_h}(t) + x_{n_p}(t) \tag{2.36}$$

Where x_{n_p} is the steady-state response to the forced excitation:

$$x_{n_p}(t) = \frac{A_0}{\sqrt{\left[\left(\frac{\omega_{1n}}{\Omega}\right)^2 - 1\right]^2 + 4\gamma^2\left(\frac{\omega_{1n}}{\Omega}\right)^2}} \cos(\Omega t - \phi), \tag{2.37}$$

with

$$\phi = \arctan\left(\frac{2\gamma(\omega_{1n}/\Omega)}{(\omega_{1n}/\Omega)^2 - 1}\right). \tag{2.38}$$

And x_{n_h} represents the initial transient displacement. During this transient regime, the natural frequencies are excited, leading to an additional oscillatory contribution that is exponentially damped during the first moments of the motion:

$$x_{n_h}(t) \propto e^{-\gamma\omega_{1n}t}\cos(\omega_{1n}\sqrt{1-\gamma^2}t). \tag{2.39}$$

The duration of this initial transient phase is dependent on the damping ratio of the system and on the natural frequency that is being excited.

Free damping

When the tank excitation is stopped, the liquid inside the container enters free damping conditions. The fluid displacement is described by a damped oscillatory motion that satisfies Equation 2.39.

Consequently, as the fluid motion decreases its amplitude, the free surface displacement, η, as well as the sloshing force, F_x, will also be described by decay functions [8] such that:

$$\eta(t) \propto e^{-\omega_n t} \quad \text{and} \quad F_x(t) \propto e^{-\omega_n t}. \tag{2.40}$$

The damping ratio, γ, is often measured indirectly through the logarithmic decrement Λ. This parameter measures the ratio between the peak amplitude of a signal for two sequential time periods [38].

$$\Lambda = \ln\left(\frac{\text{Current Peak Response}}{\text{Next Peak Response}}\right) \tag{2.41}$$

Therefore, the damping ratio is computed as:

$$\gamma = \frac{\Lambda}{\sqrt{4\pi^2 + \Lambda^2}}. \tag{2.42}$$

2.7 Sloshing regimes

According to Miles' weakly nonlinear theory [20], the fluid response to a forced lateral motion is strongly dependent on the excitation parameters, namely the amplitude A_0, and frequency Ω of the movement.

Three different sloshing regimes may be observed, depending on the selection of these two parameters [13, 40, 41]:

1. **Linear sloshing (planar waves):** Observed for low amplitudes and frequencies very far from resonance. Characterized by a steady harmonic motion where the peak wave height is constant over time. The free surface remains planar, the nodal diameter is fixed and perpendicular to direction of excitation, and the oscillation frequency is equal to the excitation frequency. This is the regime that is characterized with potential and mechanical models outlined throughout this chapter.

2. **Chaotic sloshing:** Typically takes place near resonance conditions. Characterized by a rotary motion that never becomes constant or harmonic. Peak wave height and nodal diameter change with time. Wave height increases until the moving wave's acceleration equals the gravitational forces. After wave breaking, the process restarts until the critical amplitude is reached again.

3. **Swirl wave:** Very stable regime that typically develops when the excitation frequency is higher than resonance conditions. Constant rotary motion of the free surface along the axial direction. Nodal diameter rotates with constant angular velocity.

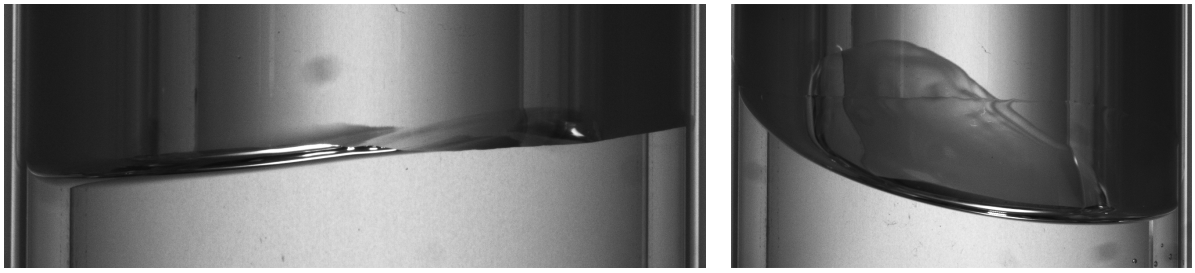

(a) (b)

Figure 2.6: Experimental observations of sloshing regimes: (a) Planar (b) Swirl wave. Image acquisition performed at VKI with a 16-bit sCMOS camera at 100Hz.

For lateral sloshing, deep waters and low damping conditions, Miles determined that the boundaries between these regimes are defined by Equation 2.43, where $\mathfrak{B}_i$ are the fixed values of the frequency offset parameter that separate the different sloshing regimes: $\mathfrak{B}_2 = -0.36$, $\mathfrak{B}_3 = -1.55$, and $\mathfrak{B}_4 = 0.735$.

$$\frac{A_0}{R} = \frac{1}{1.684}\left(\frac{(\Omega/\omega_{11})^2 - 1}{\mathfrak{B}_i}\right)^{3/2} \tag{2.43}$$

Figure 2.7 shows the phase diagram for the different sloshing regimes that can be obtained by varying the dimensionless excitation amplitude A_0/R and frequency Ω/ω_{11}.

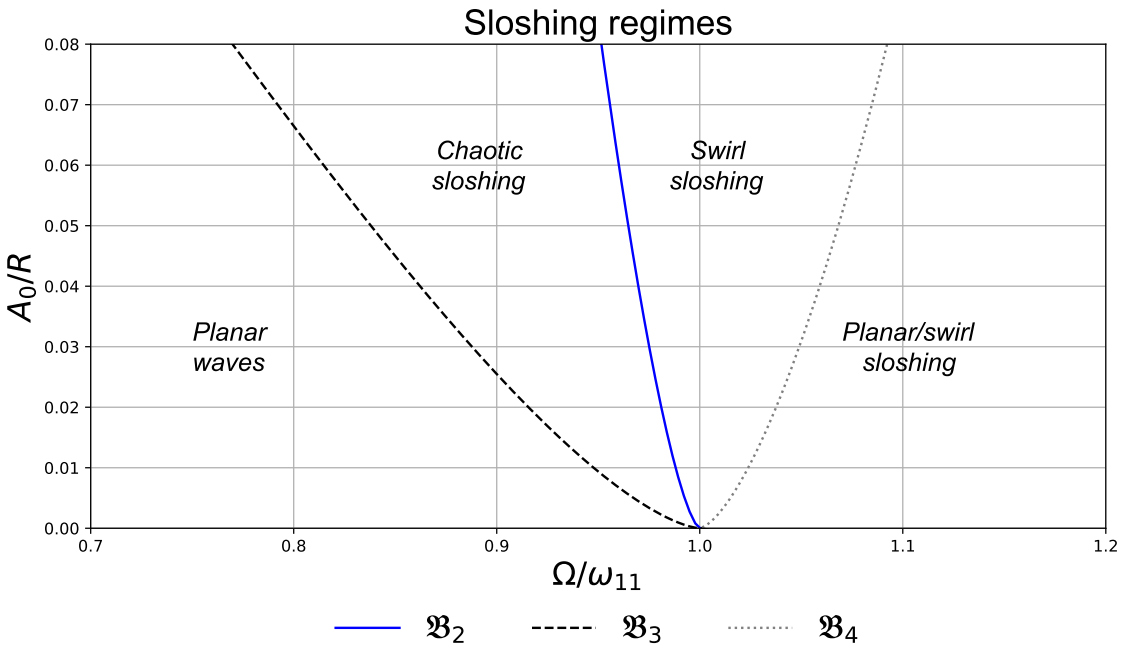

Figure 2.7: Phase diagram for the different sloshing regimes.

Chapter 3

Scaling the problem

The main purpose of this work is to analyse the scaling for the sloshing-induced thermal mixing phenomenon that takes place inside cryogenic stages of launch vehicles. Given the typical dimensions of these stages, it is typically not viable to create full-size prototypes to experiment with in laboratorial settings. Thus, small-scale models must be created. The challenge is to preserve similarity in terms of the flow conditions that take place between the small-scale model and the real life full-size facility.

There are two main approaches in order to develop scaling laws: dimensional analysis (DA), and scaling of equation (SE) [42]. Dimensional analysis consists of three main steps:

1. Development of a list of dimensional variables that describe the system
2. Conversion of these dimensional quantities into dimensionless numbers
3. Determination of a physical law that relates these dimensionless numbers

The main drawback of the DA approach is that the entire list of dimensional variables to consider must come from the individual. There is no guarantee that the quantities chosen are the most relevant, or that they completely model the physics related to the problem. On the other hand, in the SE approach these variables are directly given by the governing equations as well as the boundary and initial conditions of the system. However, this approach is still not infallible since simplifications are often made to the governing equations of the system and their true impact on problem might not be fully known *a priori*.

For this work, dimensionless numbers will be obtained through the SE approach.

3.1 Dimensionless numbers

This section is dedicated to explaining the relevant dimensionless numbers for the non-isothermal lateral sloshing problem. Two main assumptions are considered for the scaling approach followed in this work. The first is the assumption that the gas phase produces a negligible impact in the sloshing motion. This is attributed to the large difference in the inertia of the gas compared to the liquid. The second is the consideration that the main driver for the thermodynamic evolution of the system is the mixing that takes place between the interface and the sub-cooled liquid region underneath it [8]. As a result,

the dimensionless numbers are generated by scaling only the equations and boundary conditions which govern the liquid phase.

Therefore, neglecting phase change effects, the set of relevant governing equations and boundary conditions for the non-isothermal scaling problem is summarized below. The dimensionless numbers which control the isothermal problem can still be retrieved from this analysis by neglecting the parameters which arise from the energy equation as well as the Boussinesq approximation.

$$\nabla \cdot \mathbf{u} = 0 \tag{3.1}$$

$$\rho_0 \frac{\partial \mathbf{u}}{\partial t} + \rho_0 \mathbf{u}(\nabla \cdot \mathbf{u}) = -\nabla p + \mu \nabla^2 \mathbf{u} + \rho_0 [1 - \beta(T - T_0)]\mathbf{g} \tag{3.2}$$

$$\rho \frac{\partial}{\partial t}(C_v T) + \rho \nabla \cdot (C_v \mathbf{u} T) = \nabla (k \nabla T) \tag{3.3}$$

$$\Delta p = p_{\text{liq}} - p_{\text{gas}} = -\sigma \kappa. \tag{3.4}$$

Table 3.1 contains the list of reference quantities used for the nondimensionalization of these equations. The tank radius (R) was chosen as the reference length, and the excitation velocity ($A_0\Omega$) was used as the reference velocity. The dimensionless temperature in the gas and liquid was defined based on the boundaries of these phases.

Table 3.1: Reference parameters considered for the scaling analysis.

Physical parameter	**Reference**	**Definition**
Length	R	Container radius
Velocity	$A_0\Omega$	Tank excitation velocity
Acceleration	g	Gravitational acceleration
Time	$R/A_0\Omega$	Length scale divided by the velocity scale
Pressure	$\rho_0(A_0\Omega)^2$	Dynamic pressure scaling
Temperature	$T_{\text{top}} - T_{\text{bot}}$	Difference between the tank top (warm) and bottom (cold)

The dimensionless expressions are obtained by inserting the reference quantities from Table 3.1 in the dimensional equations and manipulating the terms until they are dimensionless. This is shown below from Equations 3.5 to 3.8.

$$\nabla^* \cdot \mathbf{u}^* = 0 \tag{3.5}$$

$$\frac{\partial \mathbf{u}^*}{\partial t^*} + \vec{u}^*(\nabla^* \cdot \mathbf{u}^*) = -\nabla^* p^* + \underbrace{\frac{\mu}{\rho_0(A_0\Omega)R}}_{1/\pi_1} \mu \nabla^{*2}\mathbf{u}^* + \underbrace{\frac{gR}{A_0^2\Omega^2}}_{1/\pi_2} \mathbf{f}^* - \underbrace{\frac{A_0^2\Omega^2}{gR\beta\Delta T_{ref}}}_{1/\pi_3} (\Delta T)^* \mathbf{g}^* \tag{3.6}$$

$$\frac{\partial T^*}{\partial t^*} + \mathbf{u}^*(\nabla^* T^*) = \underbrace{\frac{k}{\rho C_v (A_0\Omega) R}}_{1/\pi_4} \nabla^{*2} T^* \tag{3.7}$$

$$\Delta p^* = \underbrace{\frac{\sigma}{\rho (A_0\Omega)^2 R}}_{1/\pi_5} \kappa^* \tag{3.8}$$

The full set of dimensionless numbers is shown in Table 3.2. The Reynolds number (Re) is associated with the π_1 parameter and it relates the relative strength of viscous forces when compared to inertial ones. This parameter is crucial in sloshing applications since it offers an estimate for the damping that the liquid experiences as it moves along the container walls. This is important for the initial moments of sloshing since the wave solution is the superposition of the excited frequency wave-mode with higher frequency modes which are gradually damped throughout time. Thus, differences in the system's damping ratio will yield different transient wave responses.

The Froude (Fr) and Weber (We) numbers are connected to the π_2 and π_5 parameters, respectively. These dimensionless numbers compare the relative strength of hydrodynamic forces, thus determining which hydrodynamic regime may be expected. The scheme shown in Figure 3.1 synthesizes this analysis by classifying the flow as gravity, inertia or capillary dominated. For sloshing applications, it is common to consider two different dimensionless numbers: the Bond (Bo), and Ohnesorge (Oh) numbers. Both of these can be obtained from the already derived set of dimensionless parameters, and they directly relate the importance of surface tension with respect to the other hydrodynamic forces.

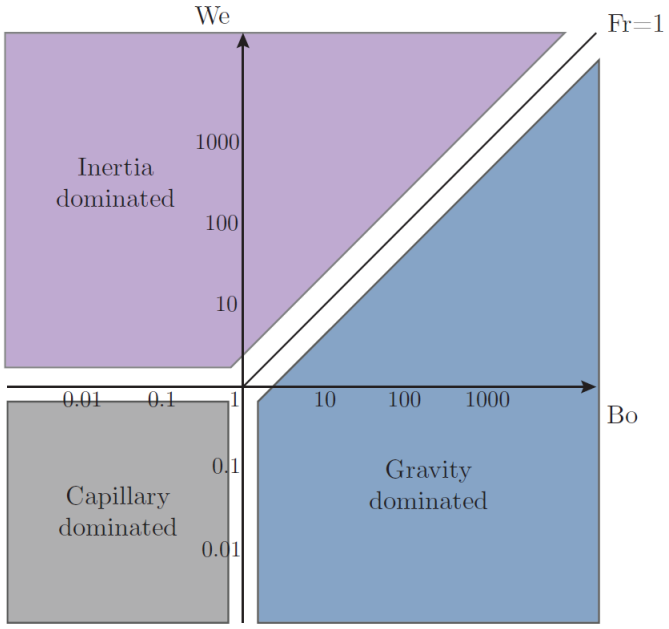

Figure 3.1: Hydrodynamic regimes [23].

The Bond number is in the horizontal axis of Figure 3.1. It can be obtained through the ratio of the Reynolds and Weber numbers, and it relates the importance of gravitational forces with respect to

capillary ones [31].

$$\mathrm{Bo} = \frac{\mathrm{We}}{\mathrm{Fr}} = \frac{\rho g R^2}{\sigma} \tag{3.9}$$

The Ohnesorge number on the other hand, is the ratio of the Weber and Reynolds numbers and it relates viscous, inertial and capillary forces [31]. This parameter is especially important for strong capillary flows, and for these conditions it takes the place of the Reynolds number in assessing the effect of damping in the flow motion [43, 44].

$$\mathrm{Oh} = \frac{\sqrt{\mathrm{We}}}{\mathrm{Re}} = \frac{\mu}{\sqrt{\rho \sigma R}} \tag{3.10}$$

Buoyancy driven convection is related to inertial forces through the π_3 parameter. This may be described as the ratio of the Grashof (Gr) with the square of the Reynolds number. Where Gr is defined as:

$$\mathrm{Gr} = \frac{g \beta \Delta T_{\mathrm{ref}} L^3}{\nu}. \tag{3.11}$$

With L being the reference length. Finally, the ratio of thermal diffusion to advection is related to the π_4 parameter which may be seen as the Peclet number (Pe) for heat transfer [33].

Table 3.2: Dimensionless numbers for the nonisothermal lateral sloshing problem

	DN	Expression	Definition
π_1	Re	$\frac{\rho_0 (A_0 \Omega) R}{\mu}$	Inertial forces / Viscous forces
π_2	Fr	$\frac{A_0^2 \Omega^2}{gR}$	Inertial forces / Volume forces
π_3	$\frac{\mathrm{Gr}}{\mathrm{Re}^2}$	$\frac{gR\beta \Delta T_{\mathrm{ref}}}{A_0^2 \Omega^2}$	Buoyancy forces / Inertial forces
π_4	Pe	$\frac{\rho_0 C_v (A_0 \Omega) R}{k}$	Advection / Diffusion
π_5	We	$\frac{\rho_0 (A_0^2 \Omega^2) R}{\sigma}$	Pressure forces / Surface tension

This analysis was developed by scaling the conservation equations and boundary conditions applied to the sloshing problem. However, the same exercise could be applied to the potential flow and to the equivalent mechanical models. However, it must be noted that not every parameter would be able to be reproduced with the standard simplified expressions. For example, neither the potential or mechanical models take thermal effects into account, and the linearised potential flow assumption neglects viscous damping.

3.2 Scaling approach

Geometric similarity

The goal for this work is to establish scaling laws between a large-scale cryogenic tank and a small-scale laboratorial model. Thus, geometric similarity is established between both facilities by scaling up the already existing laboratorial model.

The VKI sloshing cell consists of a quartz cylindrical container with flat top and bottom with a radius R = 40 mm, and a total height H = 104 mm. The large-scale facility considered in this work is obtained by scaling up the small-scale model by a factor of fifty. This results in a cylindrical sloshing tank with radius R = 2000 mm, and total height H = 5200 mm. These dimensions are in agreement with typical full-size cryogenic containers found in the literature [7, 45, 46, 47].

Moreover, the liquid fill ratio is considered fixed and equal to 80% for both facilities and all test cases. This value was chosen in order to mimic the high fill levels of cryogenic stages in launch vehicles during the initial propelled flight phase. Moreover, this assures that h/R = 2.08 $>$ 1, meaning that the bottom shape of the container produces a negligible effect in the sloshing response [8, 48]. The geometric constraints for this study are summarized in Table 3.3.

Table 3.3: Dimensions for the full-size cryogenic tank and the small-scale laboratorial model

	R (m)	H (m)	Fill level (%)
VKI sloshing cell	0.04	0.104	80
Full size facility	2	5.2	

Kinematic similarity

Kinematic similarity is enforced by selecting excitation parameters such that the wave response (i.e. sloshing regime) is identical in both the large and small-scale facilities. This is achieved by guaranteeing that the frequency offset parameter $\mathfrak{B}$, is the same for both facilities [41]:

$$\mathfrak{B} = \frac{\left(\frac{\Omega}{\omega_{11}}\right)^2 - 1}{\left(1.684\frac{A_0}{R}\right)^{2/3}}. \tag{3.12}$$

Thus, kinematic similarity is satisfied provided that the dimensionless excitation amplitude A_0/R and frequency Ω/ω_{11} are imposed. As a result of fixing these quantities, the dimensional excitation parameters may be written as follows:

$$A_0 = \underbrace{\left(\frac{A_0}{R}\right)}_{const.} R \quad \text{and} \quad \Omega = \underbrace{\left(\frac{\Omega}{\omega_{11}}\right)}_{const.} \Omega. \tag{3.13}$$

Recalling that for normal gravity conditions and deeply filled tanks $\omega_{11} \sim \sqrt{g/R}$, the excitation velocity is written as:

$$A_0\Omega \sim \underbrace{\left(\frac{A_0}{R}\right)\left(\frac{\Omega}{\omega_{11}}\right)}_{const.} \sqrt{gR}. \tag{3.14}$$

Thus, $[u] \sim \sqrt{gR}$ is found as an excitation-independent characteristic velocity for gravity-dominated sloshing. This result shows that the π_2 parameter (Froude number) is always preserved between large and small-scale sloshing facilities provided that the dimensionless excitation parameters are kept constant.

Dynamic similarity

Dynamic similarity is assured if all dimensionless numbers are equal for both the small-scale model and the large cryogenic tank. As stated above, fixing the dimensionless excitation parameters for both facilities allows for equality to be maintained in terms of the Froude number. This guarantees that the relative importance of inertia and volume forces in the flow is the same.

Analysing parameters π_1, π_4 and π_5, it is evident that these are exclusively dependent on the tank dimensions and on the fluid's properties. As a result, given that the container dimensions are imposed on the problem, similarity with respect to these quantities can only be attempted through the adequate choice of fluid for the small-scale model.

On the other hand, π_3 is additionally dependent on the reference temperature difference ΔT_{ref}. Thus, similarity for this parameters may be improved by imposing adequate values for the initial thermal field in the sloshing containers. The relationship between the reference temperature difference in the small-scale model $(\Delta T_{ref})_m$ and the full-size facility $(\Delta T_{ref})_p$ that guarantees perfect similarity in terms of π_3 is given by Equation 3.15

$$(\Delta T_{ref})_m = \left(\frac{A_0^2 \Omega^2}{gR\beta} \right)_m (\pi_3)_p. \tag{3.15}$$

Scaling approach

The scaling approach used in this work is the following:

1. Select fixed values for the dimensionless excitation parameters: A_0/R and Ω/ω_{11}. This assures that the sloshing regime is respected, and that the Froude number (π_2) will be the same for both facilities.

2. Select a fluid to be used for the small-scale facility such that dimensionless parameters π_1, π_4, and π_5 are as similar as possible.

3. Consider an initial thermal field in the small-scale facility such that the reference temperature difference (ΔT_{ref}) yields for good similarity in terms of the π_3 parameters.

The first step of this approach is simple to execute since it only requires adjusting the excitation amplitude and frequency that are imposed on the container. However, step 2 raises several difficulties since there is no known fluid which can lead to perfect matching of the dimensionless numbers in both sloshing facilities. As mentioned in Chapter 1, the full size facility is filled with cryogenic H_2, and the small-scale model is typically operated with engineering fluids (HFE7000, HFE7200) or cryogenic N_2 [14, 8, 16]. The properties of theses fluids for atmospheric pressure and saturation conditions are shown in Table 3.4.

Figures 3.2 to 3.4 show the similarity in terms of the Reynolds, Peclet and Weber numbers for both facilities considering N_2, HFE7000 and HFE7200 as replacement fluids for H_2, and assuming a linear sloshing excitation with $A_0/R = 0.045$ and $\Omega/\omega_{11} = 0.7$. When comparing the dimensionless numbers for the full-size and small-scale cases, a difference of 2 to 3 orders of magnitude can be observed for the chosen replacement fluids.

Table 3.4: Fluid properties for gas and liquid H_2, gas and liquid N_2, liquid HFE7000 and liquid HFE7200 at atmospheric pressure and saturation conditions. Information from the NIST database [49], and Rausch *et. al* (2015) [50].

	T_{ref} (K)	ρ_0 (kg/m^3)	ν (m^2/s)	σ (N/m)	C_p (J/kgK)	k (W/mK)	α (m^2/s)	β (1/K)
LH2	20.6	70.58	1.85E-7	1.91E-3	9904.74	0.104	1.49E-7	0.016
GH2	20.6	1.42	7.71E-7		12134.22	0.017	1.01E-6	0.264
LN2	77.94	803.43	1.95E-7	8.74E-3	2044.36	0.144	8.8E-8	0.006
GN2	77.94	4.91	1.12E-6		1128.29	0.008	1.36E-6	0.107
HFE7000	293.15	1418.14	3.29E-7	0.012	1294.94	0.075	4.08E-8	0.002
HFE7200	293.15	1433.91	4.83E-7	0.014	1213.36	0.067	3.85E-8	1.58E-3

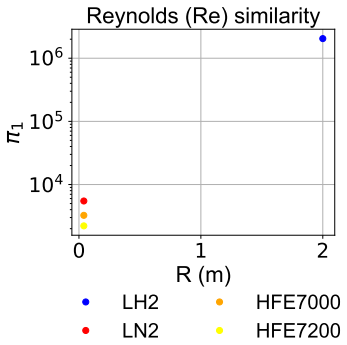

Figure 3.2: π_1 similarity.

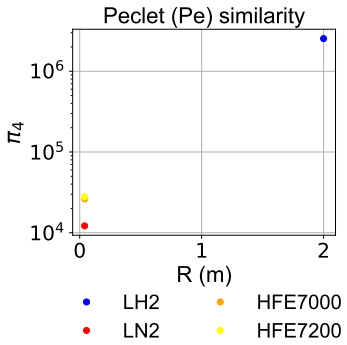

Figure 3.3: π_4 similarity.

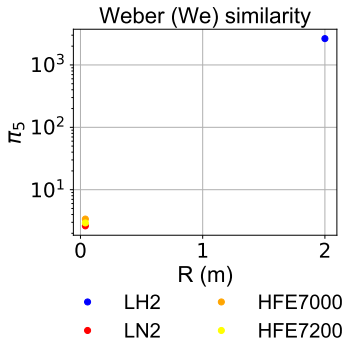

Figure 3.4: π_5 similarity.

The difference in terms of the Reynolds number suggests that the small sloshing cell suffers significantly more damping than the full-size facility due to the stronger relative strength of viscous forces compared to inertial ones. Moreover, the difference in the Peclet indicates that thermal diffusion has a stronger effect on the heat transfer that takes place in the smaller geometry relative to advection. Intuitively this is attributed to the fact that the smaller container allows for the thermal information to propagate throughout the domain by diffusion more quickly than in the larger container. Finally, assessing the difference in the Weber number, one can conclude that, once again due to the smaller scale, surface tension effects are more important in the VKI sloshing cell. However, provided that the tank diameter is much larger than the capillary length of the problem, surface tension is expected to play a negligible role.

Step 3 allows for similarity to be assured in terms of the π_3 dimensionless number (Gr/Re^2). This is achieved through Equation 3.15, which relates the temperature difference between the top and bottom of the containers for both sloshing facilities.

Given this relationship, a simplified approach is used for the physical modeling of the thermal stratification process. An initial state is set for the container, where both the gas and liquid regions are assumed to have constant temperature. The temperature in the gas phase is assumed to be equal to the temperature in the top of the container, $T_{gas} = T_{top}$, and the liquid is assumed to have the temperature of the bottom, $T_{liq} = T_{bot}$ (Figure 3.5a). Then, the system is allowed to evolve towards equilibrium

with heat transfer taking place between the warm gas and the cold liquid. This leads to the formation of the thermally stratified field shown in Figure 3.5b, where the black dotted line indicates the position of the interface.

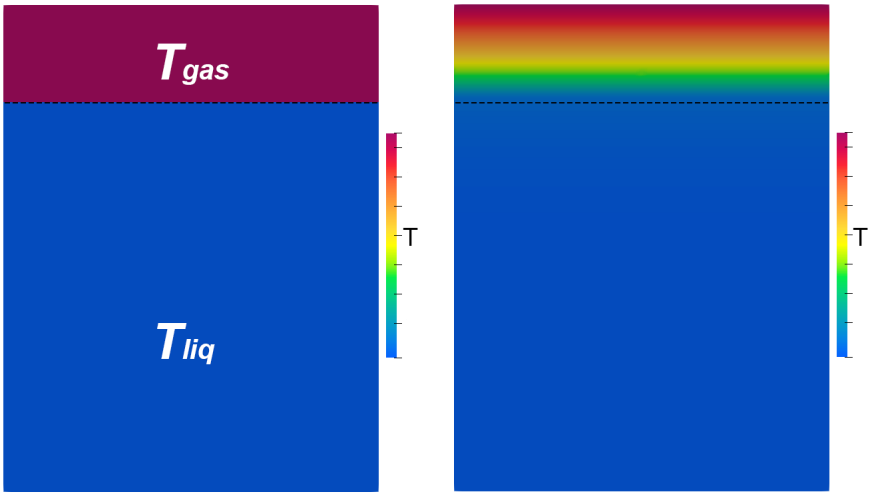

(a) (b)

Figure 3.5: Simplified model to determine the thermally stratified field: a) Initial thermal profile with constant temperature in the gas and liquid b) Stratified thermal field at a more advanced point in time.

The temperature of the gas and liquid is known for the full-size H_2 facility from the master's thesis of Hoppe (2013) [11]. In this document, a performance study is executed for the pressurization of the ESC-A cryogenic stage from the Ariane 5 ECA launch vehicle. The average temperature of the gaseous hydrogen is measured to be at 47.3 K and the liquid is at 20.6 K for tank pressures between 3.1-3.3 bar.

Table 3.5: Temperature information for H_2 and the replacement fluids in order to guarantee perfect similarity in terms of the π_3 dimensionless parameter.

	H_2	N_2	HFE 7200	HFE 7000
ΔT (K)	26.7	77.65	271.83	218.91
T_{liq} (K)	20.6	77.35	-	-
T_{gas} (K)	47.3	155	-	-

The simplified model requires T_{gas} and T_{liq} to be introduced as inputs in order to start the non-isothermal analysis. As such, these values are calculated for the potential replacement fluids (N_2, HFE700 and HFE7200) through similarity with the π_3 dimensionless number in the liquid phase. Table 3.5 shows the required values for the temperature difference between the gas and liquid regions in order guarantee perfect similarity in terms of $(\pi_3)_{liq}$. These results highlight the difficulty in using non-cryogenic fluids for the current non-isothermal analysis given the impractically large ΔT required by this scaling approach. Consequently, for the remainder of this work, only H_2 and N_2 were considered in the numerical analysis.

Chapter 4

Numerical methods

4.1 The Volume of Fluid Method

The Volume of Fluid Method (VOF) was first developed by Hirt and Nichols in 1981 [51] with the goal of modeling immiscible multiphase flows in CFD (Computational Fluid Dynamics). The VOF method defines a volume fraction variable α_f which varies between 0 and 1 in order to represent the volumetric proportion of fluid phase *f* in a given cell of a CFD mesh [23]. If α_f = 1, the cell is fully filled with fluid *f*, whereas if α_f = 0 there is no amount of this fluid contained in the cell. Therefore, cells which contain α_f values between 0 and 1 indicate the presence of the free-surface. For N immiscible phases, the total sum of all volume fractions in a given cell must amount to unity.

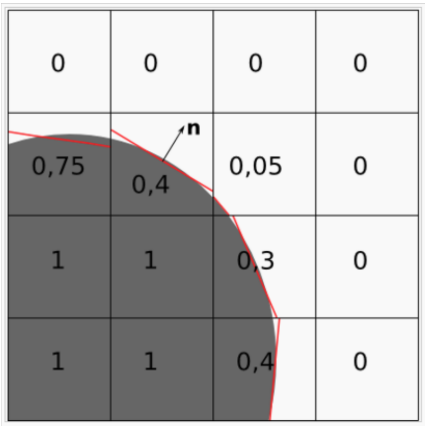

Figure 4.1: Interface discretization with the VOF method [52].

Figure 4.1 shows the fluid interface being captured in a two-phase flow with the VOF method. The dark shaded cells represent the liquid, whereas the light grey cells correspond to the gas. The number in each cell is the volumetric fraction of the liquid α_l, the straight lines show the estimated placement of the free surface, and **n** is the calculated interface normal vector in the respective cell.

The VOF method allows for a single set of continuity, momentum and energy equations to be solved for the entire multiphase flow. The position of fluid *f* and the movement of the free surface is determined

by solving the typical conservation equations alongside the advection equation for α_f:

$$\frac{\partial \alpha_f}{\partial t} + \nabla \cdot (\alpha_f \mathbf{u}) = 0. \tag{4.1}$$

After the determination of the α_f field, equivalent fluid properties are computed in each cell based on the individual fluid properties and on the volume fraction field. For the case of a two phase flow composed by liquid and gas, the cell density and kinematic viscosity required by the momentum equation are given by:

$$\rho = \rho_l \alpha_l + \rho_g (1 - \alpha_l) \tag{4.2}$$

$$\nu = \nu_l \alpha_l + \nu_g (1 - \alpha_l) \tag{4.3}$$

Where, the *l* subscript refers to the liquid, and *g* refers to the gas. This procedure is applied to any property that is used in the governing equations and can be easily extended to more than two phases.

The VOF method in OpenFOAM

The simplest implementation of the VOF method in OpenFOAM is done through the `interFoam` solver. This is a two-phase solver for immiscible, incompressible and isothermal fluids that solves a single set of continuity and momentum equations alongside the α advection equation. The continuity equation is implemented as shown in Equation 2.4, however both the momentum and α equations have some modifications.

In order to give stability to the solution and to simplify the definition of boundary conditions, the pressure is treated through the `p_rgh` variable [53]:

$$p_{rgh} = p - \rho \mathbf{g} \cdot \mathbf{x}. \tag{4.4}$$

Where **x** is the position vector and p_{rgh} is the modified pressure obtained by removing the hydrostatic component $\rho \mathbf{g} \cdot \mathbf{x}$ from the total value. An additional source term is also added to the momentum equation in order to account for capillary forces near the interface. This is achieved through the Continuum Surface Model (CSF) developed by Brackbill *et. al* (1992) [54], which is shown in Equation 4.5.

$$F_\sigma = \sigma \kappa \nabla \alpha_f \tag{4.5}$$

Where σ is the surface tension, α_f is the volumetric fraction for fluid *f* and κ is the mean free surface curvature given by:

$$\kappa = \nabla \cdot \left(\frac{\nabla \alpha_f}{|\nabla \alpha_f|} \right). \tag{4.6}$$

Thus, the momentum equation solved in `interFoam` is the following:

$$\frac{\partial}{\partial t}(\rho \mathbf{u}) + \mathbf{u}\nabla \cdot (\rho \mathbf{u}) = -\nabla p_{rgh} + \nabla \cdot \mathbb{T} - \mathbf{g} \cdot \mathbf{x}(\nabla \rho) + \sigma \kappa \nabla \alpha_f. \tag{4.7}$$

The interface is captured by solving the volumetric phase fraction advection equation with an additional compression term that aims to reduce numerical diffusion and smearing of the interface [55]. Thus, the α advection equation considered by the solver is shown in Equation 4.8, where $\mathbf{u}_c$ is the relative velocity that acts perpendicular to the free surface, calculated through Equation 4.9.

$$\frac{\partial \alpha_f}{\partial t} + \nabla \cdot (\alpha_f \mathbf{u}) + \underbrace{\nabla \cdot [\alpha_l(1-\alpha_l)\mathbf{u}_c]}_{\text{Additional compression term}} = 0. \tag{4.8}$$

$$\vec{u_c} = C_\alpha |\mathbf{u}| \frac{\nabla \alpha_f}{|\nabla \alpha_f|} \tag{4.9}$$

The C_α parameter is a user defined value which quantifies the magnitude of the compression term [52]. It is usually set to 1 corresponding to a "compression velocity" of the same order as the local flow velocity [56].

In order to further minimize numerical diffusion in the transport of the volumetric phase fraction and to guarantee boundedness in the solution, the MULES (Multidimensional Universal Limiter with Explicit Solution) scheme is applied to solve the α advection equation. This is an implementation of the FCT (Flux Corrected Transport) theory developed by Zalesak (1979) [57], and is extensively detailed in the work of Márquez Damián (2014) [53].

The `interFoam` algorithm in `OpenFOAM-v1912` is described in Appendix B.1

4.2 Numerical Grids

The three-dimensional numerical grid was generated using the `blockMesh` utility included with the installation of `OpenFOAM-v1912`. A total of 36 regions (or blocks) were generated in order to adequately model the cylindrical container. As shown in Figure 4.2, each transversal section of the geometry is defined by an inner square region, four intermediate sections, and four exterior sections close to the container walls. The axial direction was decomposed in four main sections: liquid (Z01), bottom-interface (Z12), upper-interface (Z23), and main gas (Z34).

The number of cells in the inner box region is controlled by the n_T parameter, whereas the number of cells in the radial direction for the intermediate and exterior regions are defined by n_R and n_{R2}, respectively. Identically, parameters n_{Z01}, n_{Z12}, n_{Z23}, and n_{Z34} control the number of cells in the axial direction for their respective regions. The total mesh dimensions (i.e. inner box side length, cylinder radius and height) were scaled by a given factor such that the grid proportions were kept the same for both the large and small-scale sloshing facilities. This allowed for the grid density to be the same for both situations. Moreover, the base time-step was scaled based on Equation 4.10, where T_e is the period of excitation and N is the user-selected number of time-steps per period. This procedure ensured that the same

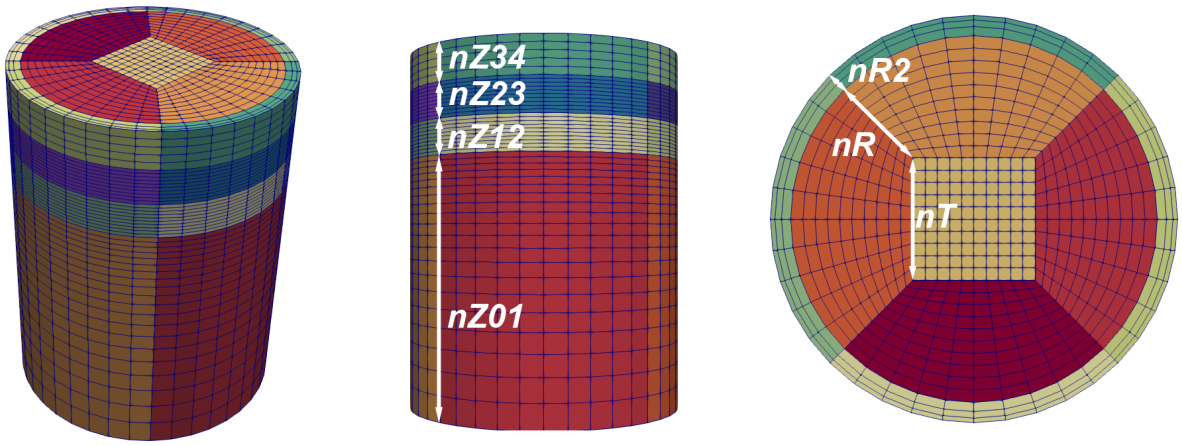

Figure 4.2: Three-dimensional mesh generated with the `blockMesh` utility.

temporal resolution was applied to both sloshing containers.

$$\Delta t = \frac{T_e}{N} \tag{4.10}$$

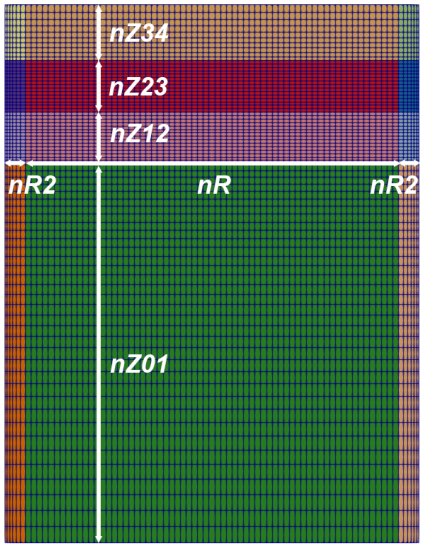

Figure 4.3: Two-dimensional mesh generated with the `blockMesh` utility.

Chapter 5 contains the grid independence study which was conducted for both the large H2 and small N2 containers. The objective was to assess the impact of the grid spacing and temporal resolution on the sloshing response. For this purpose, the time-step was adjusted in order to guarantee the Courant number was maintained constant between all simulations. OpenFOAM calculates this parameter through Equation 4.11, where Δt is the simulation's time step, V is the cell volume, and ϕ_i is the volumetric face flux.

$$\mathrm{Co} = 0.5 \frac{\Delta t}{V} \sum_{faces} |\phi_i| \tag{4.11}$$

The '0.5' factor arises from the fact that the magnitude of the cell face flux $|\phi_i|$ is considered. In

reality ϕ_i is either negative or positive depending on whether the flux is entering or exiting the cell face. Therefore, an average of the incoming and outgoing fluxes is estimated by summing them together and dividing by two [58].

In order to test the effects of finer grids and more reduced time-steps without severely increasing the computational time and resources, two-dimensional grids were also generated using `blockMesh`. The 2D simulations are not perfectly equivalent to the 3D ones since instead of representing a cylinder, these consider the domain to be more akin to a rectangular container. Nonetheless, for linear sloshing conditions, the potential theory indicates that the flow solutions should be identical [36]. Figure 4.3 shows the generated two-dimensional grid, which inherits an identical generation process to the 3D case.

The chosen temporal scheme was the first-order implicit Euler, the gradient and laplacian terms were discretized with second-order Gauss linear, and the divergence terms were treated with the second-order TVD (Total Variation Diminishing) flux-limiting van Leer scheme. This scheme limits the cell face fluxes, thus eliminating numerical oscillations (i.e. wiggles) in the flow field [59]. Moreover, no turbulence model was considered for this analysis [60].

4.3 Modeling of isothermal lateral sloshing

As mentioned in Chapter 2, liquid sloshing in a closed reservoir can be modeled through two methods:

1. Imposed excitation through rigid body motion of the container using Equation 2.1.
2. Imposed excitation in a non-inertial reference frame where the container is stationary and the motion is introduced through source terms in the momentum equations. The source terms account for the changes in acceleration expressed by Equation 2.3.

In order to check if both approaches produce identical results in `OpenFOAM`, two sloshing simulations were performed using the methods stated above. The numerical grid, discretization schemes, solution methods, and time-step were kept the same for both cases, with the only difference being in the method of exciting the fluid. The simulations were performed in the linear sloshing regime for 120 seconds, with $(A_0/R) = 0.1$ and $(\Omega/\omega_{11}) = 0.5$ for the large H_2 tank. The base time-step used was 0.006 seconds, and the maximum allowed Courant number was set to 0.1.

The rigid body motion is available with the default `interFoam` solver that comes installed with `OpenFOAM v1912`. The lateral oscillatory motion is applied through the `dynamicMeshDict` file shown in Listing 4.1. The amplitude of the oscillating motion is set to 0.2 meters, and the frequency is roughly 1.502 rad/s.

Listing 4.1: `dynamicMeshDict` file required to model the oscillating rigid body motion.

```
dynamicFvMesh      dynamicMotionSolverFvMesh;
motionSolver      solidBody;
solidBodyMotionFunction    oscillation;
solidBodyMotionFunction    oscillatingLinearMotion;
oscillatingLinearMotionCoeffs
```

```
{
        amplitude (0.2 0 0);
        omega  1.501717859;
}
```

On the other hand, the implementation of the non-inertial sloshing method requires modification to the solver's source code in order to account for time-varying body forces. The modified solver is named `interModGFoam`, and it works by reading a new acceleration field at each time-step from a tabulated list [23]. The time-varying acceleration field is then added to the momentum equation in the form of the **g** vector that is shown in Equation 4.7, such that:

$$\mathbf{g} = \left(\ddot{X}_0(t), 0, g\right)^{\mathsf{T}} \text{, where } g \approx 9.8 \text{ m/s}^2. \tag{4.12}$$

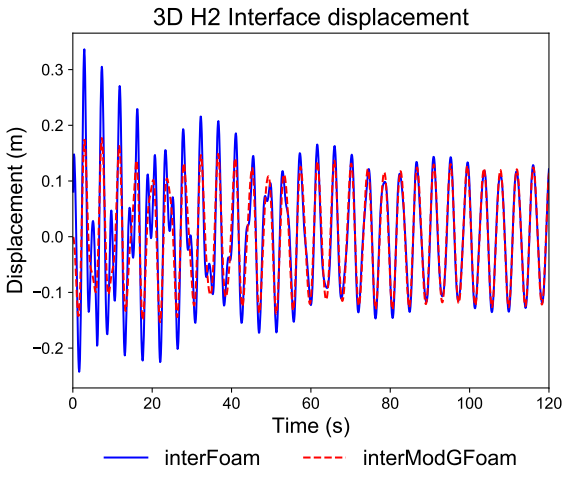

Figure 4.4: Interface displacement with the `interFoam` and `interModGFoam` solvers

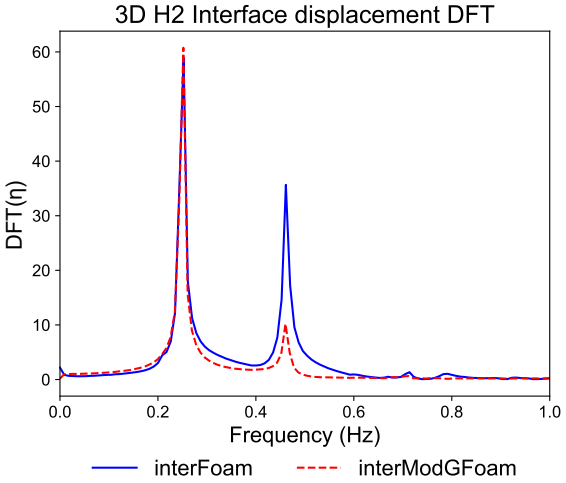

Figure 4.5: Interface displacement DFT with the `interFoam` and `interModGFoam` solvers

Figure 4.4 shows the temporal evolution of the interface displacement using both methods. The chosen temporal scheme is the first-order implicit Euler, the gradient and laplacian terms are discretized with second-order Gauss linear, and the divergence terms are treated with the second-order TVD (Total Variation Diminishing) flux-limiting van Leer scheme. The base time-step is of 0.006 seconds, with a maximum courant number of 0.1.

The initial sloshing response is the result of the superposition of the 'steady-state' periodic solution where the fluid sloshes according to the excitation frequency $\Omega = 2\pi f_e$, with the initial transient response which develops according to the natural frequency $\omega_{11} = 2\pi f_{11}$ and that is damped at a rate of $\gamma\omega_{11}$ s^{-1} [13]. This initial transient phase is observed in both cases, however its intensity appears to depend on the excitation method.

The `interModGFoam` static mesh approach results in considerably smaller wave amplitudes and the solution as whole appears to be less sensitive to this initial superposition of modes. This can be checked by computing the Discrete Fourier Transform (DFT) of the signal, which is shown in Figure 4.5. The excitation frequency $f_e = 0.239$ Hz is both the first and largest spike visible in this plot. The signal

amplitude at frequency f_e is the same for both excitation methods. This can be explained by the fact that the steady-state periodic solution,

$$\eta(t) = \eta_{max} \sin(\Omega t) \tag{4.13}$$

is equally present since the start of the simulation, as is predicted by the simplified mechanical. However, the second spike, which corresponds to the natural frequency f_{11} = 0.478 Hz and that is associated with the initial transient motion, has a much higher amplitude in the moving mesh approach than in the static one.

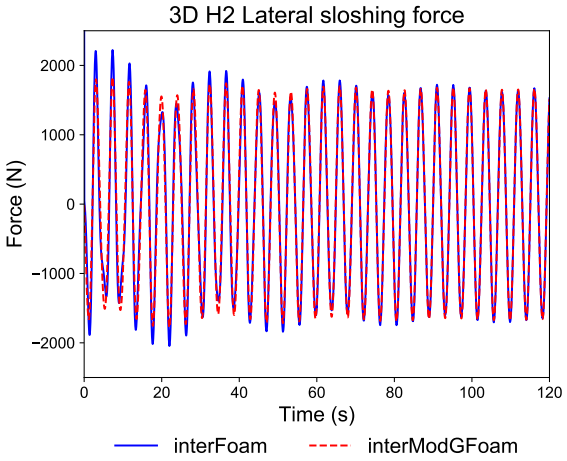

Figure 4.6: Lateral sloshing force with the `interFoam` and `interModGFoam` solvers

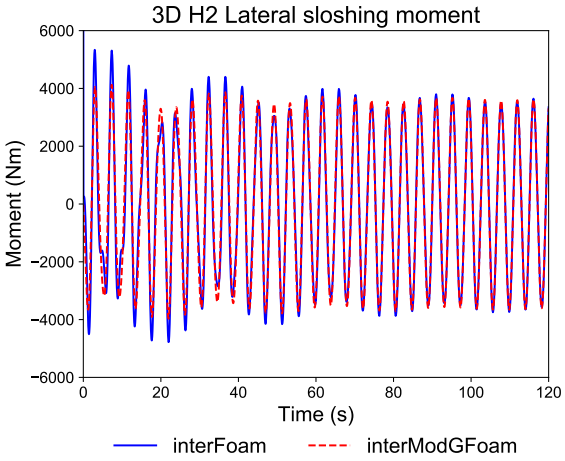

Figure 4.7: Lateral sloshing moment with the `interFoam` and `interModGFoam` solvers

When analysing the lateral sloshing force (F_x) and moment (M_y) with respect to the container's base, identical results are obtained. Figures 4.6 to 4.7 show that although the periodic sloshing response is the same using both methods, the initial transient period results in different estimations for the sloshing force and moment. This suggests that the simulation start-up might not be perfectly identical for both approaches since different responses are observed only in the transient regime, while identical solutions are obtained for steady periodic conditions.

The moving mesh approach with the `interFoam` solver was used for the remainder of this work.

4.4 Modeling of non-isothermal lateral sloshing

One of the most crucial aspects of liquid sloshing in cryogenic stages is the thermodynamic evolution of the system that is created triggered by the fluid motion. In order to model the non-isothermal effects and pressure fluctuations that take place inside these containers when they slosh, the pressure-based `compressibleInterDyMFoam` solver was considered. As the name suggests, this is a variation of the `interFoam` solver which is aimed at compressible flow problems and solves the energy balance alongside the momentum, continuity and α advection equations.

Using this solver, the Boussinesq approximation was used for the liquid phase, and the ullage gas was treated with the perfect gas model. This approach was used in the works of Himeno (2011) [15],

Agui (2015) [26], and Kartuzova (2018) [27]. However, unlike those cases, mass transfer effects are not considered in this work since the focus is to study the impact of sloshing on the thermal de-stratification effect. The numerical simulations presented in this work allow for the decoupling of the momentum and energy exchanges from the mass transfer effects, which is not possible for real life experimental conditions.

The description of the `compressibleInterDyMFoam` solver is presented in Appendix B.2.

4.5 Moving contact line problem

In a partially filled container, the contact line is known as the region which separates wet portions of the wall from dry ones. Surface tension is the result of the molecular forces in this region that arise due to a normal stress anisotropy in the vicinity of the interface [61]. This leads to a pressure difference Δp at the interface that can be calculated by the Young-Laplace equation.

The moving contact line problem arises due to the incompatibility of the no-slip boundary condition at the walls with the fact that the liquid-gas interface must be allowed move (slip) [62]. Physically speaking, if the flow velocity at the walls was indeed zero, the contact line would theoretically be pinned down as well and remain static until the end of time. However, in reality we know that this is not the case.

Numerically, this issue is resolved using the VOF method through the α advection equation. Even though the no-slip boundary condition is used at the walls, since the flow properties are stored in the cell centroids, there will be a non-zero velocity in the cell centre next to the wall which promotes the advection of the volumetric phase fraction along the solid boundary. The issue with this approach is that the contact line movement may become overly damped if the grid becomes too refined close to the walls, as was verified by the work of Hansinger (2016) [24]. He used the `interFoam` solver to numerically determine the damping ratio γ of water in a partly-filled container after a lateral sloshing excitation. The numerical γ was found to increase as the mesh was refined near the walls, meaning that the coarsest grids tested offered better agreement with the theoretical results. This problematic is exemplified by Figure 4.8, where the velocity gradient near the wall is shown for a coarse and fine mesh.

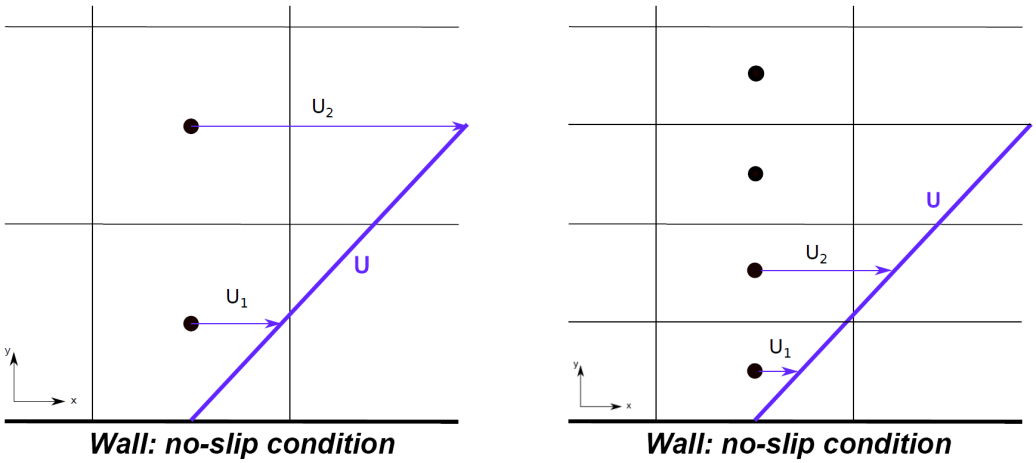

Figure 4.8: Schematic for the wall velocity gradient in a coarse mesh (left) and fine mesh (right) [24].

The advancement of the contact line along the wall is computed based on velocity U_1 which is included in the α advection equation. Assuming a no-slip condition at the wall, for a very fine grid $U_1 \to 0$, meaning that the contact line will tend to stick to the boundary. This leads to additional resistance to the free surface motion, which may then be interpreted as artificial damping.

The moving contact line problem is a well-known challenge in the simulation of two-phase flows. The problem stems from the fact that the dynamics involved are the result of molecular interactions, and applying a typical continuum mechanics approach leads to a stress singularity to be found on the contact line [61]. The Navier-slip model is a mechanism that was developed in order to relax this singularity and to eliminate the contradiction of employing a no-slip boundary condition on an moving contact line. The core idea of this model is to consider the fluid to have a given slip-velocity $\vec{u}_{slip}$ tangent to the solid surface that is proportional to the strain-rate.

$$\mathbf{u}_{\text{slip}} = \lambda \mathbf{n} \cdot \left[\nabla \mathbf{u} + (\nabla \mathbf{u})^T \right] \tag{4.14}$$

Equation 4.14 gives the slip-velocity for the proposed Navier-slip model, where **n** is the surface normal vector, and λ is called the slip-length [63]. The slip-length was first theorized by Maxwell (1878), who argued it should be proportional to the mean free path. This was later demonstrated experimentally by Andrew & Harris (1995) [64] and analytically by Bocquet (1993) [65].

Due to grid refinement limitations, numerical simulations require unrealistically large values for the slip-length in order to resolve the shear stress singularity problem. Thus, the slip length λ becomes merely an adjustable parameter for the simulation, which depends on the grid spacing [66]. Moreover, in order to provide accurate results, this method should be employed alongside a dynamic contact angle model [66, 67].

OpenFOAM allows for the implementation of a similar model through the `partialSlip` boundary condition. This allows for a given amount of slip to be considered based on the user input `valueFraction`, which may range between 0 and 1. If the `valueFraction` is set to 1, the no-slip boundary condition is recovered, whereas setting this parameter to 0 imposes the free-slip state. By inspection of the source code, this boundary condition does not seem equivalent to the Navier-slip condition since it defines the wall-normal velocity gradient (`snGrad`) and the slip-velocity as:

$$\frac{\partial U}{\partial n} = \frac{U_{slip} - U_c}{\Delta/2} \tag{4.15}$$

$$U_{slip} = \texttt{valueFraction} \cdot \texttt{refValue} + (1 - \texttt{valueFraction}) \cdot U_c \tag{4.16}$$

Where n is the surface normal vector, U_c is the velocity at the cell centroid adjacent to the wall, $\Delta/2$ is the distance between the cell centroid and the wall, and `refValue` is a user defined reference value for the velocity at the wall.

For the simulations performed in this work, the classical no-slip boundary condition was employed. The consequences of this choice are discussed in Chapter 5.

Chapter 5

Results and discussion

5.1 Isothermal sloshing

5.1.1 3D sloshing simulations

5.1.1.1 Effect of the grid refinement

The effect of the grid refinement on the sloshing motion was assessed. Four different meshes were generated following the methodology explained in Chapter 4. Figure 5.1 shows the tested numerical grids alongside their respective number of cells and Table 5.1 summarizes the time-step control parameters.

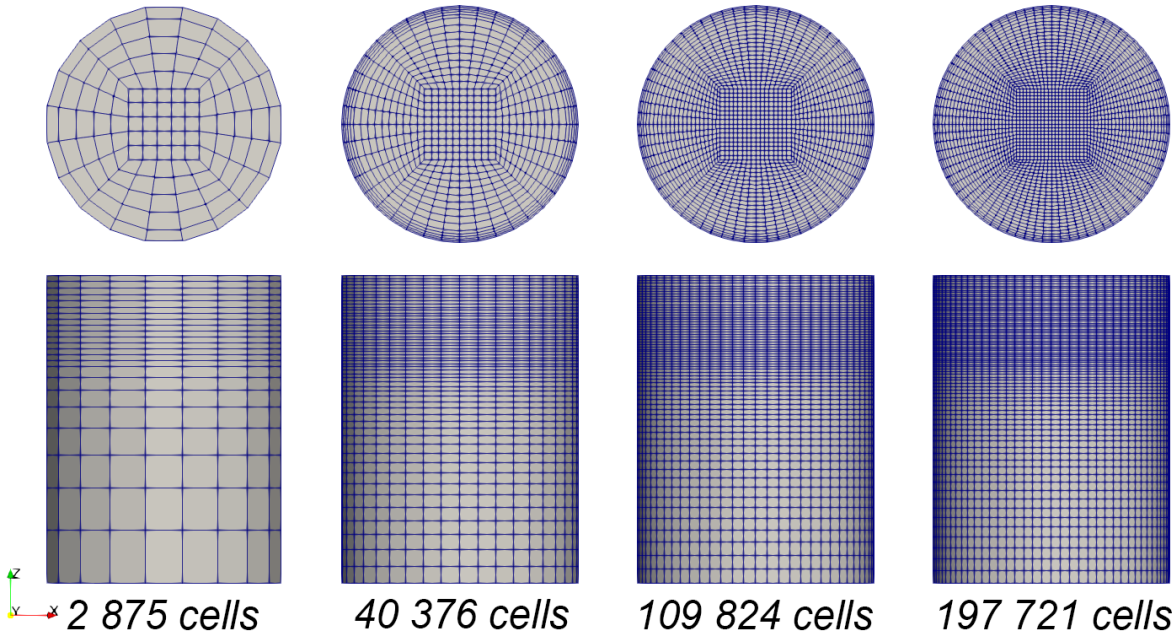

Figure 5.1: Numerical grids used for the 3D sloshing simulations and their respective hexahedral cell count.

Table 5.2 shows the fluid properties considered for H_2 and N_2 alongside the excitation conditions and tank dimensions considered for both sloshing facilities. The simulations were carried out in the linear sloshing regime with dimensionless excitation parameters: $(A_0/R) = 0.045$ and $(\Omega/\omega_{11}) = 0.7$. The fluid

Table 5.1: 3D mesh parameters for time-step control.

	Number of cells	dt (H2)	dt (N2)	max(Co)
Mesh 00	2 875	0.0144	0.002	0.1
Mesh 01	40 376	0.0072	0.001	
Mesh 02	109 824	0.006	8E-4	
Mesh 03	197 721	0.0048	6.8E-4	

properties were obtained from the NIST (National Institute of Standards and Technology) database [49] at ambient pressure and saturation conditions.

Table 5.2: Fluid properties for H_2 and N_2, their respective container dimensions, and the excitation parameters considered for both cases.

	ρ (kg/m^3)	ν (m$^2/s$)	σ (N/m)	R (m)	H (m)	A_0 (m)	ω_{11} (rad/s)	f_{11} (Hz)	Ω (rad/s)	f_e (Hz)
LH2	70.58	1.85E-7	0.002	2	5.2	0.09	2.774	0.442	1.942	0.309
GH2	1.417	7.71E-7								
LN2	803.43	1.95E-7	0.009	0.04	0.104	0.0018	21.238	3.38	14.866	2.366
GN2	4.913	1.12E-6								

Figures 5.2 and 5.3 show the interface displacement during the first instants of sloshing for the large H_2 tank and the small N_2 sloshing cell, respectively. Both these plots highlight the initial non-periodic sloshing motion that occurs when the excitation is applied directly from rest. This motion is the superposition of multiple excited wave-modes which are gradually damped as the system evolves. The rate at which these modes are damped is greatly affected by the spatial and temporal resolution of the numerical grid. In fact, Figures 5.2 and 5.3 reveal that the rate at which the higher-frequency waves are damped decreases as the grid becomes more refined. This is attributed to numerical diffusion in the coarsest grids, which generates additional damping for the sloshing motion, thus causing lower than expected wave amplitudes and leading to under-estimations for the duration of the initial transient regime.

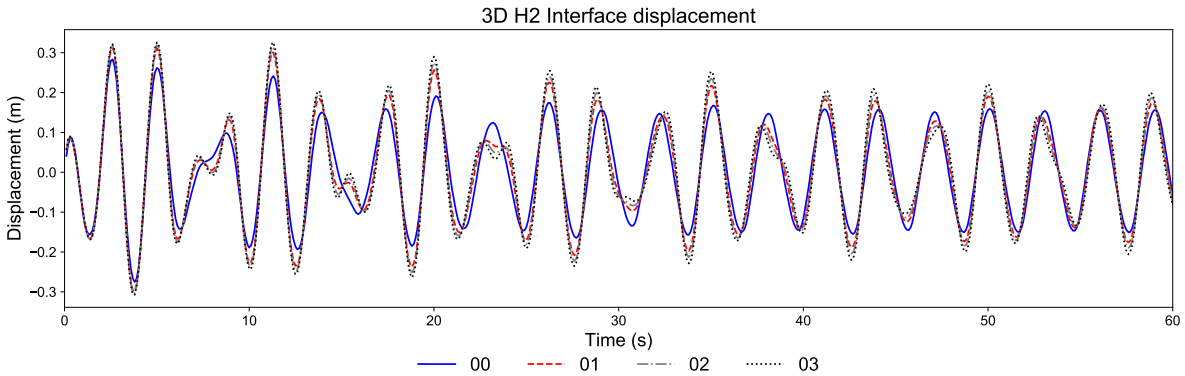

Figure 5.2: Contact line displacement in the initial sloshing moments for the H_2 container (0 to 60 seconds).

Although the initial fluid response appears to be quite sensitive to the spatial and temporal resolution,

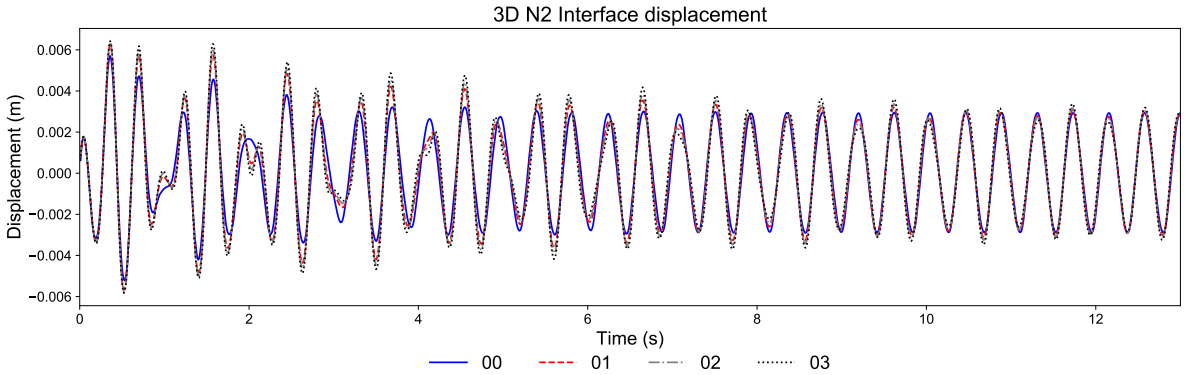

Figure 5.3: Contact line displacement in the initial sloshing moments for the N_2 container (0 to 13 seconds).

this appears to not be the case when the periodic sloshing motion fully sets in. This is seen in Figures 5.4 and 5.5, which show the contact line displacement for both the H_2 and N_2 containers in a more advanced time. At this point, all simulations produce identical results. The contact line displacement adopts an oscillatory periodic form, which is in very good agreement with the results given by the linearised potential theory (Equation 2.28).

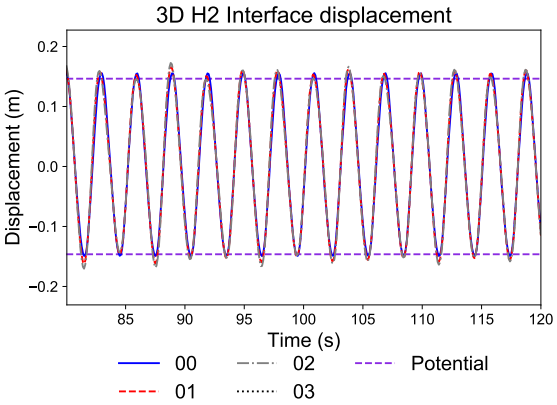

Figure 5.4: Periodic contact line displacement for the H_2 container (from 80 to 120 seconds).

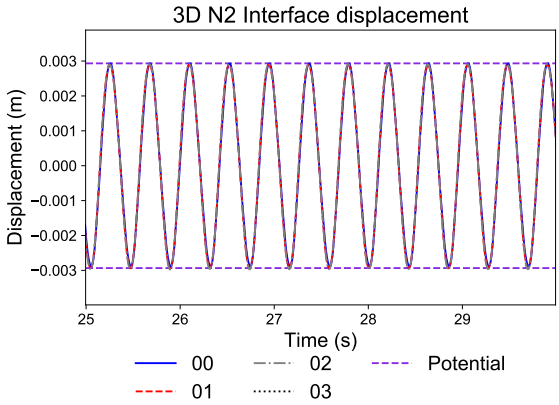

Figure 5.5: Periodic contact line displacement for the N_2 container (from 25 to 30 seconds).

Monitoring the sloshing force and moment yields identical results. However, when analysing the temporal evolution of these parameters, in Figures 5.6 and 5.7, they appear to have a more 'stable' response than the contact line displacement. In other words, the initial superposition of sloshing responses appears to have a smaller effect on the total force and moment evolution. A possible explanation for this occurrence is the fact that for planar waves the contact line displacement is mainly affected by the sloshing mass that is excited close to the interface, whereas the sloshing force and moment are calculated by integrating the pressure distribution and shear stress along the entire fluid volume. Thus, the smaller variations that occur at the surface level and that can be seen in Figures 5.2 and 5.3 will not cause enough of an impact in terms of pressure distribution or shear force to affect the total force measurement in the containers.

Figures 5.8 and 5.9 show the lateral sloshing force response for H_2 and N_2, respectively, for a more

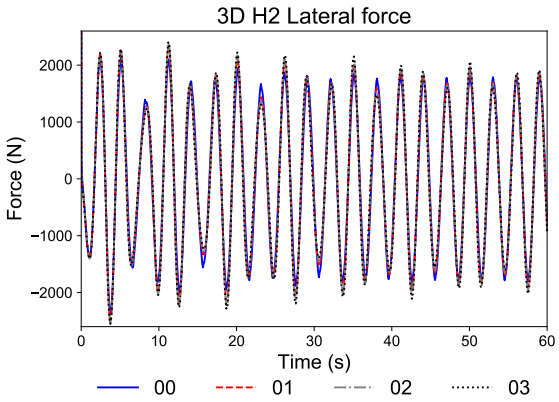

Figure 5.6: Lateral sloshing force for the H_2 container (from 0 to 60 seconds).

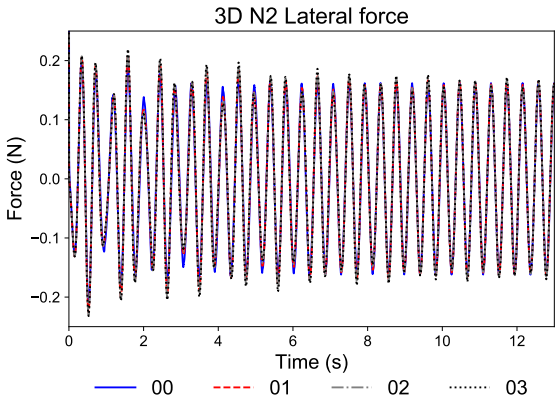

Figure 5.7: Lateral sloshing force for the N_2 container (from 0 to 13 seconds).

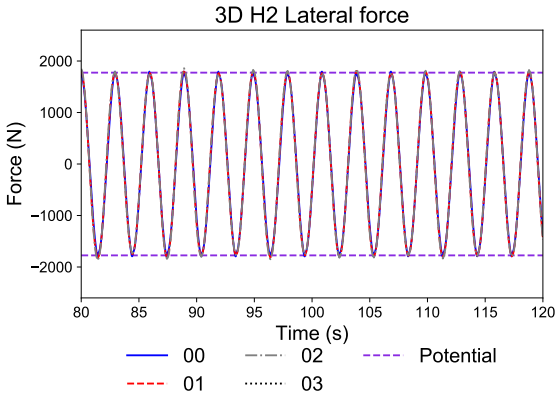

Figure 5.8: Lateral sloshing force for the H_2 container (from 80 to 120 seconds).

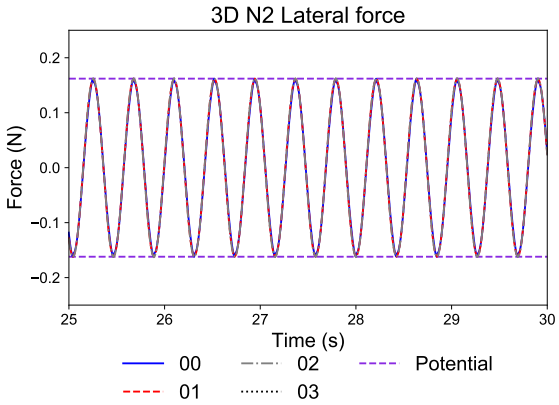

Figure 5.9: Lateral sloshing force for the N_2 container (from 25 to 30 seconds).

advanced point in time where the higher frequency waves are already damped. Once again, the results line up almost perfectly with the theoretical lateral force given by the linearised potential flow theory (Equation 2.30).

Figures 5.10 and 5.11 show the Discrete Fourier Transform (DFT) of the lateral sloshing force in the H_2 and N_2 containers, respectively. These results show the expected superposition of two wave signals at different frequencies, f_{11} and f_e.

For H_2, the Fourier analysis reveals the first spike to be the numerical estimate for the forced frequency, given in the most refined grid by f_e = 0.33 Hz, and the second spike to be the numerical natural frequency, f_{11} = 0.47 Hz. Similarly, the results for N_2 in the most refined grid yield f_e = 2.37 Hz, and f_{11} = 3.33 Hz. The frequency analysis confirms the fact that as the grid is refined, the intensity of the signal at f_{11} increases relative to signal at f_e for both the H_2 and N_2 facilities. This translates to a stronger presence of the higher frequency modes in the transient response.

To assess the effect of numerical diffusion on the initial transient response, the numerical damping ratio was computed by conducting free damping sloshing simulations. Utilizing the data from previous simulations, the sloshing motion was stopped and the fluid was allowed to enter free damping conditions,

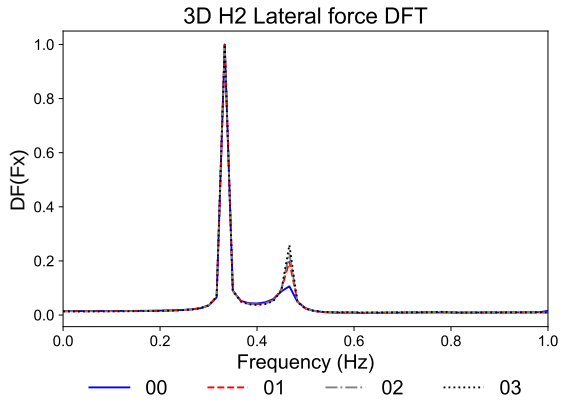

Figure 5.10: DFT for the H_2 lateral sloshing force signal from 0 to 60 seconds.

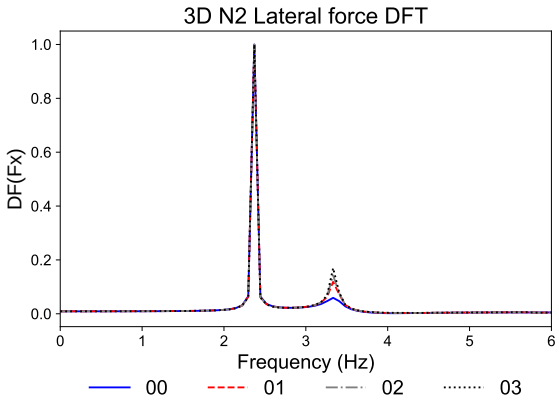

Figure 5.11: DFT for the N_2 lateral sloshing force signal from 0 to 13.5 seconds.

sloshing side-to-side while the wave amplitude gradually decreased. Figures 5.12 and 5.13 show the lateral force evolution for free damping conditions in the H_2 and N_2 containers, respectively. These plots confirm the fact that the damping rate of the system decreases as the grid is refined and the time-step reduced.

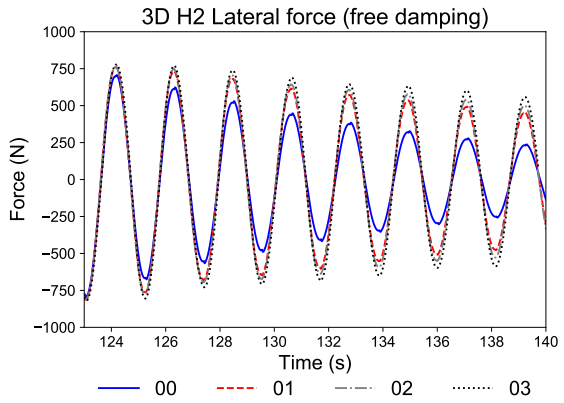

Figure 5.12: Lateral sloshing force for free damping conditions in the H_2 container.

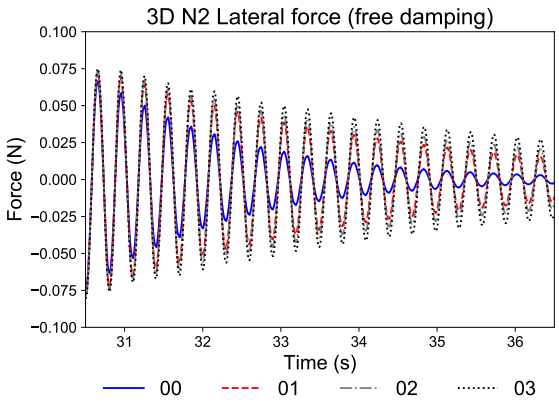

Figure 5.13: Lateral sloshing force for free damping conditions in the N_2 container.

The numerical damping rate of the system γ_{num} is calculated in a few steps. First, the local maxima of the lateral sloshing force $F_{max,i}$ in free damping conditions are extracted and matched alongside the current peak number, i. Then, the logarithm is applied to these values in order to relate $\ln(F_{max,i})$ with i. An exponential decay in amplitude yields a linear decrease of $\ln(F_{max,i})$ as i increases. The slope of this function is the logarithmic decrement of the system Λ_{num}:

$$\Lambda_{num} = \frac{1}{i} \ln\left(\frac{F_{max,0}}{F_{max,i}}\right), \tag{5.1}$$

which is used to obtain the numerical damping rate through Equation 2.42.

Figures 5.14 and 5.15 show the linear decrease of $\ln(F_{max,i})$ alongside the computed numerical damping rate for the different meshes used in the H_2 and N_2 cases. These results are summarized in Table 5.3 and compared with the empirical formula given by Equation 2.35.

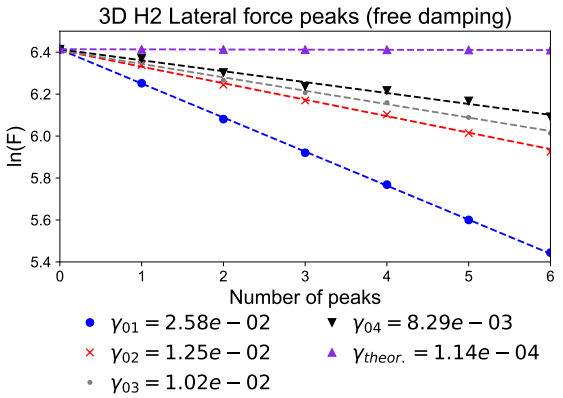

Figure 5.14: Logarithmic decrement for the lateral sloshing force in the H_2 container.

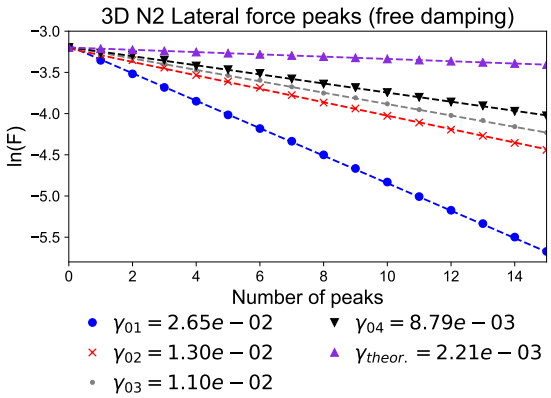

Figure 5.15: Logarithmic decrement for the lateral sloshing force in the N_2 container.

Table 5.3: Comparison of numerical and theoretical damping ratios for both the H_2 and N_2 sloshing facilities, where Λ is the logarithmic decrement, and γ is the damping ratio.

	H2 00	H2 01	H2 02	H2 03	N2 00	N2 01	N2 02	N2 03
Λ_{num}	0.162	0.079	0.064	0.052	0.167	0.082	0.069	0.055
γ_{num}	2.58e-2	1.25e-2	1.02e-2	8.29e-3	2.65e-2	1.30e-2	1.10e-2	8.79e-3
γ_{theor}	1.14e-4				2.21e-3			
$\gamma_{num}/\gamma_{theor}$	226.3	109.6	89.47	72.7	12	5.9	5	4

There are two main observations that can be made from Table 5.3. First, the numerical damping ratios for both the H_2 and N_2 simulations are considerably higher than the ones given by Equation 2.35. This is true especially for the H_2 case where the difference is almost two orders of magnitude even for the most refined grid. Second, although the theoretical damping rates for H_2 and N_2 are almost an order of magnitude different compared to each other, the numerical values are very similar among both cases (i.e. $\gamma_{H2_{00}} \sim \gamma_{N2_{00}}$, $\gamma_{H2_{01}} \sim \gamma_{N2_{01}}$, and-so-on).

These results suggest that numerical diffusion dominates the free vibration problem and that the damping shown in Figures 5.12 and 5.13 is actually a measure of the 'numerical damping'. Moreover, by examining the $\gamma_{num}/\gamma_{theor}$ parameter, it is estimated that the full-size H_2 facility and the N_2 sloshing cell should reach mesh independent states at different grid refinements. Since the full-size facility experiences smaller physical damping rates, a more refined grid must be used in this case in order to decrease numerical diffusion to lower values.

However, it should be noted that this analysis is only relevant if the transient regimes are of interest. For cases where only the periodic planar response is relevant, the results of this section show that the flow solution is identical across all the tested numerical grids.

5.1.1.2 Isothermal 3D similarity

This section is devoted to the analysis of the scaling laws for isothermal sloshing. To achieve this, the dimensionless interface displacement η^*, lateral force F_x^* and moment M_y^* are compared between the full-size H_2 facility and the N_2 sloshing cell. The non-dimensionalization of these flow parameters is based on the reference quantities used to scale the governing equations in Chapter 3. As such,

the interface displacement η is scaled with the reference length R, while the lateral sloshing force and moment are scaled with the reference dynamic pressure $\rho_0(A_0\Omega)^2$ integrated over the container's lateral walls with area $2\pi Rh$. The underlying assumption in this analysis is that pressure forces are dominant compared to shear forces, and thus the dynamic pressure scaling is adequate to evaluate the sloshing loads. The considered dimensionless flow parameters are given by Equation 5.2.

$$\eta^* = \frac{\eta}{R} \tag{5.2}$$

$$F_x^* = \frac{F_x}{\rho_0(X_0\Omega)^2 Rh} \tag{5.3}$$

$$M_y^* = \frac{M_y}{\rho_0(X_0\Omega)^2 Rh^2} \tag{5.4}$$

Figures 5.16, 5.17 and 5.18 show the dimensionless interface displacement, lateral sloshing force and moment for both the H_2 and N_2 containers using the 02 mesh configuration. These results show good similarity in the numerical simulations of both sloshing containers, especially when the stable sloshing regime is reached. For these conditions, the small-scale results can be scaled up in order to predict the flow response in the large container with great accuracy (Figures 5.17 and 5.18).

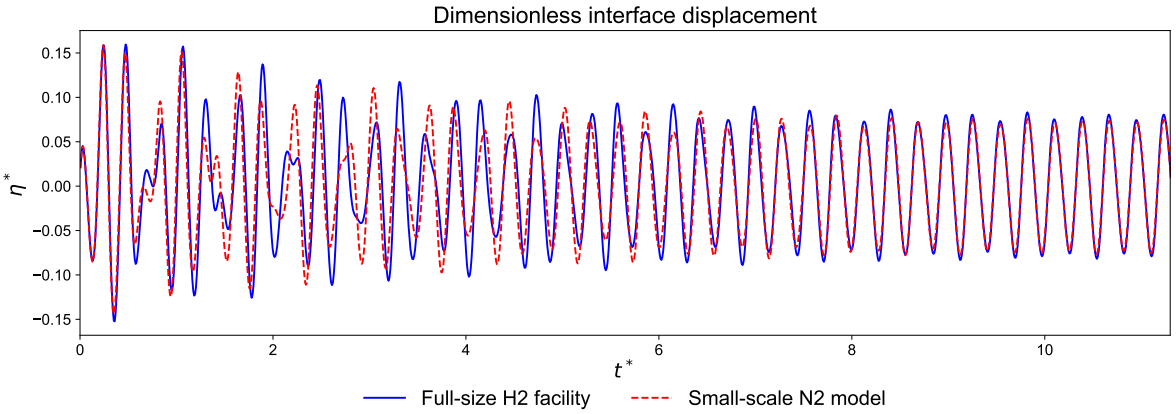

Figure 5.16: Dimensionless interface displacement for the H_2 and N_2 facilities between $t^* = 0$ and $t^* = 11.3$.

As was expected, the main differences lie within the initial transient regime, however even for this stage, the flow response very similar. The maximum interface displacement, sloshing force and moment are shown in Table 5.4, alongside the average ϵ_{avg} and maximum ϵ_{max} differences between both dimensionless solutions over time.

Table 5.4: Maximum values and deviations for the dimensionless interface displacement, lateral force and sloshing moment in the H_2 and N_2 containers.

	η^*_{max}	ϵ^{η}_{avg}	ϵ^{η}_{max}	$F^*_{x_{max}}$	$\epsilon^{F_x}_{avg}$	$\epsilon^{F_x}_{max}$	$M^*_{y_{max}}$	$\epsilon^{M_y}_{avg}$	$\epsilon^{M_y}_{max}$
H2	0.1597	0.0002	0.0703	112.050	0.069	77.58	66.667	0.066	71.892
N2	0.1588			112.384			66.749		

During the transient period, higher-frequency wave modes are excited and gradually damped. This

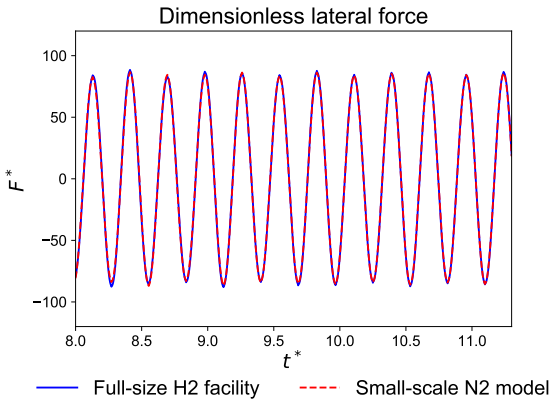

Figure 5.17: Dimensionless lateral force for the H_2 and N_2 facilities between $t^* = 8$ and $t^* = 11.3$.

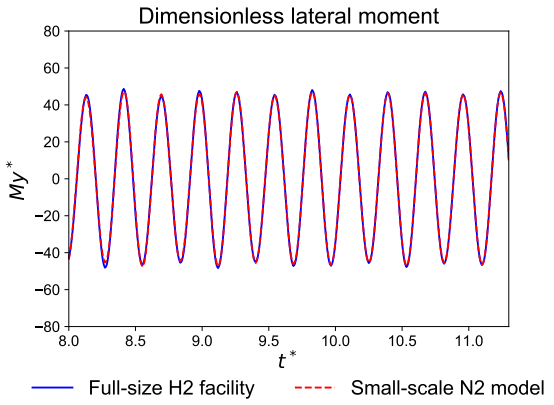

Figure 5.18: Dimensionless lateral moment for the H_2 and N_2 facilities between $t^* = 8$ and $t^* = 11.3$.

means that differences in the damping ratio of the system lead not only to distinct flow responses during this stage, but also to different durations of the transient state itself in both containers. The numerical damping rates for both systems are estimated as $\gamma_{H2\_02} = 0.0102$ and $\gamma_{N2\_02} = 0.011$. As mentioned in the previous section, even though these values are very similar between each other, they are one to two orders of magnitude higher than the theoretical values from Equation 2.35. It is believed that numerical diffusion dominates the problem and because of this, γ_{H2_02} and γ_{N2_02} are not accurate measures for the real damping in the system. As a result, one should be very critical of the flow similarity observed during the initial transient period.

The fact that these parameters are identical between each other suggests that both simulations show good similarity in the numerical sense. However, neither case is spatially or temporally refined enough to show the true viscous damping nature of the system. In order to further investigate this issue without greatly increasing the computational resources required, the next section continues this same analysis but with two-dimensional cases.

5.1.2 2D sloshing simulations

5.1.2.1 Effect of the grid refinement on the numerical diffusion

As a starting point for the two-dimensional simulations, the effect of the grid refinement on the numerical sloshing solution was assessed. The 2D nature of the problem allowed for higher spatial and temporal refinements to be considered than in the three-dimensional simulations. The tested numerical grids are shown in Figure 5.19 and the mesh parameters are summarized in Table 5.5.

The two-dimensional problem can be seen in three dimensions by considering a rectangular container where the third spatial dimension (normal to the plane seen in Figure 5.19) is much larger than the height or width. Thus, the expected damping in the 2D simulations is not the expected to be the same as in the 3D case. Nonetheless, this study was still conducted in order to have an order of magnitude for this issue without increasing too much the computational demand of the simulations. For these

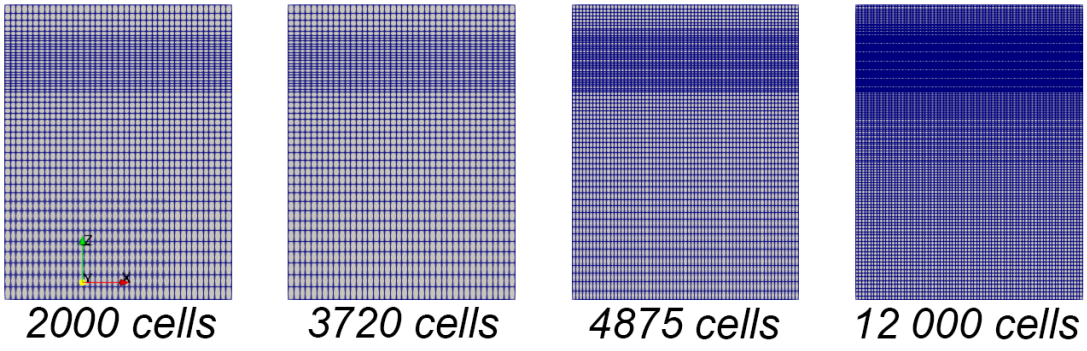

Figure 5.19: Numerical grids used for the 2D sloshing simulations and their respective hexahedral cell count.

conditions, the first asymmetrical natural frequency of the system is given by [24]:

$$\omega_{11}^2 = \frac{\pi g}{R} \tanh\left(\frac{\pi g h}{R}\right), \tag{5.5}$$

where R is the bottom length of the rectangular container. This yields ω_{11} = 2.77 rad/s for H_2 and ω_{11} = 19.62 rad/s for N_2. In order to make sure that the same point of the Miles diagram (Figure 2.7) is considered, the excitation frequency was adjusted in order to guarantee the same Ω/ω_{11} of the 3D simulations.

Table 5.5: 2D mesh parameters for time-step control.

	Number of cells	**dt (H2)**	**dt (N2)**	**max(Co)**
Mesh 01	2000	0.0056	0.0008	0.1
Mesh 02	3720	0.0046	0.0007	
Mesh 03	4875	0.0037	0.0005	
Mesh 04	12 000	0.0019	0.0003	

Figures 5.20 and 5.21 show the lateral sloshing force the H_2 and N_2 containers with the different tested grids for the first moments after sloshing. The solution is identical to the observed in the three-dimensional simulations. Moreover, applying the Discrete Fourier Transform (5.22 and 5.23) to these signals reveals that once again they are the result of the superposition of two elements: one constant amplitude wave excited at f_e, and an exponentially decaying wave at f_{11}. The increase in spatial and temporal resolution decreases the effect of numerical diffusion, thus increasing the damping time of the higher frequency wave. This is seen in Figures 5.22 and 5.23 where the amplitude of the signal at f_{11} increases alongside the grid refinement.

The numerical damping rates for the 2D cases shown in Figures 5.24 and 5.25 are computed with the method outlined in Section 5.1.1.1. These results are summarized and compared to the theoretical values in Table 5.6. Given the rectangular container shape, the theoretical damping rate is calculated with Equation 2.35 considering $C_1 = 1$ and $n = 1/2$ [36].

The higher grid refinement used for the 2D cases resulted in lower numerical damping rates than the 3D simulations. The results are particularly favourable for the N_2 sloshing cell, where γ_{num} becomes

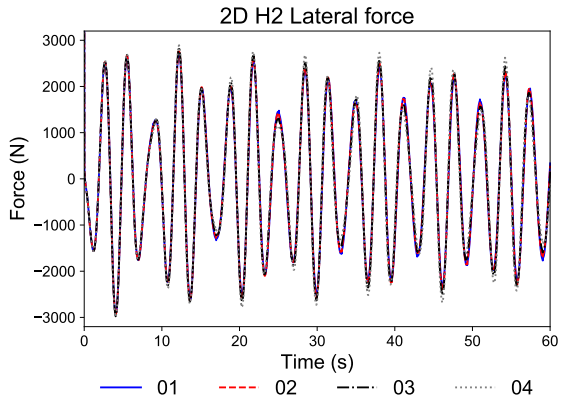

Figure 5.20: 2D H_2 lateral force signal from 0 to 60 seconds.

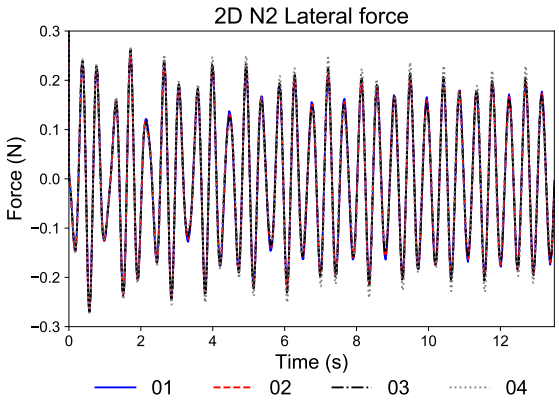

Figure 5.21: 2D N_2 lateral force signal from 0 to 13.5 seconds.

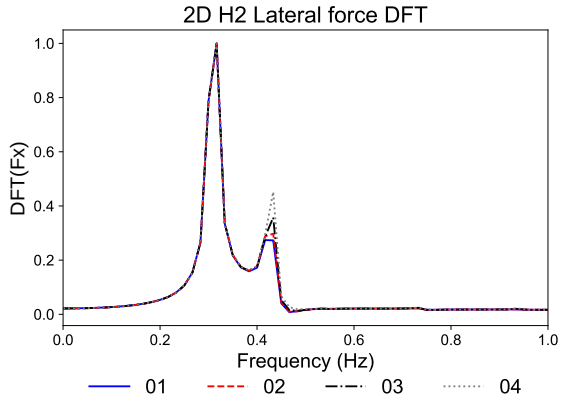

Figure 5.22: DFT for the 2D H_2 lateral force signal from 0 to 60 seconds.

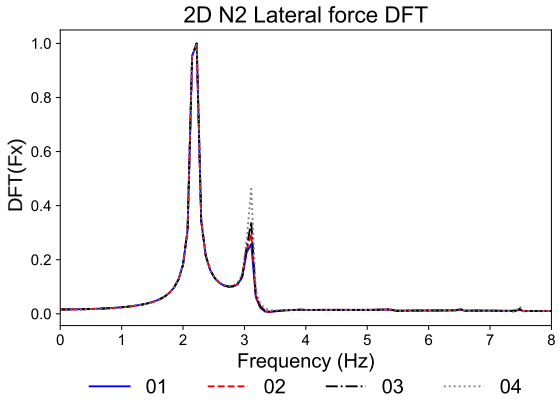

Figure 5.23: DFT for the 2D N_2 lateral force signal from 0 to 13.5 seconds.

very close to theoretical value as the grid is refined. For the full-size H_2 facility, the additional cells and reduced time-step help with decreasing γ_{num}, however there is still a difference of around one order of magnitude with respect to γ_{theor}.

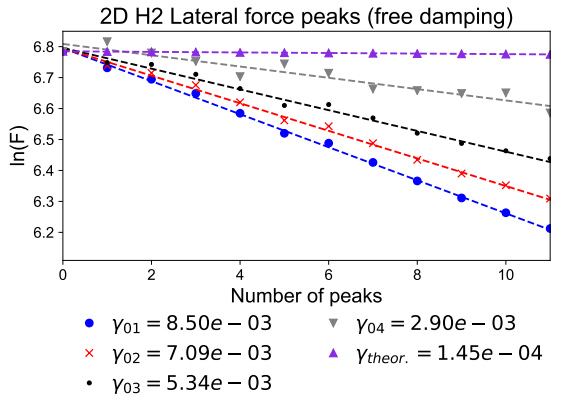

Figure 5.24: Logarithmic decrement for the lateral sloshing force in the H_2 container.

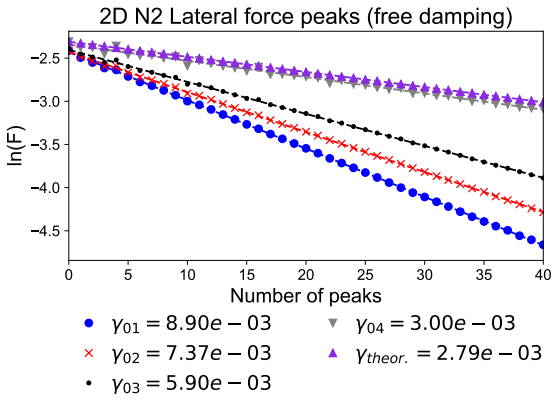

Figure 5.25: Logarithmic decrement for the lateral sloshing force in the N_2 container.

Table 5.6: Comparison of numerical and theoretical damping ratios for both the H_2 and N_2 sloshing facilities, where Λ is the logarithmic decrement, and γ is the damping ratio.

	H2 01	H2 02	H2 03	H2 04	N2 01	N2 02	N2 03	N2 04
Λ_{num}	0.053	0.045	0.034	0.018	0.056	0.046	0.037	0.019
γ_{num}	8.5e-3	7.09e-3	5.34e-3	2.9e-3	8.9e-3	7.37e-3	5.9e-3	3e-3
γ_{theor}	1.45e-4				2.79e-3			
$\gamma_{num}/\gamma_{theor}$	58.6	48.9	36.83	20	3.2	2.64	2.11	1.08

5.1.2.2 Effect of the wall resolution

As mentioned at the end of Chapter 4, the no-slip velocity boundary condition was selected for the container side-walls. As a result of this choice, the movement of the contact line is assured by the velocity stored at the centroid of the wall-adjacent cell. Thus, in order to assess the effect this has in the numerical solution, three different wall refinement configurations were tested in the N_2 sloshing cell. These can be seen in Figure 5.26. The grid refinement was applied in a specific region close to the walls defined as the Stokes boundary layer.

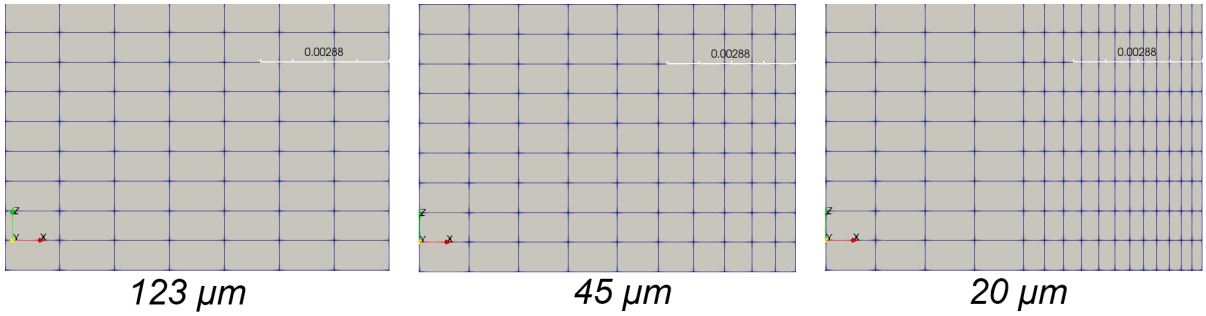

Figure 5.26: Close up on the different wall refinement configurations tested. The first cell thickness of each case is: 123 μm (left), 45 μm (center) and 20 μm (right).

According to theory of linear sloshing, the Stokes boundary layer is the region close to the wall where viscous dissipation takes place [36]. For this dynamic problem, the thickness of this boundary layer δ_s depends on the fluid's viscosity, the frequency of excitation, and is estimated by Equation 5.6.

$$\delta_s = 2\pi\sqrt{\frac{2\nu}{\Omega}} \tag{5.6}$$

For the N_2 sloshing cell excited at a frequency of Ω = 13.73 rad/s, δ_s is estimated to be equal to 2.88 mm (7.2% of the container radius). Table 5.7 summarizes the relevant information regarding the different wall refinement configurations tested. Mesh "N2 03" was considered as the base for this series of tests, which is now labelled as "A".

Table 5.7: Summary of the wall refinement configurations for the N_2 sloshing cell

Mesh	1st cell thickness (μm)	Stokes boundary layer thickness (mm)	N. cells inside Stokes boundary layer
A	123	2.88e-3	2
B	45		5
C	20		10

Figure 5.27 shows the interface displacement using the three mesh configurations mentioned above. By direction inspection, an appreciable difference between the different cases is not observed. The mean deviation between the solution given by mesh A and B is only 0.2%, and 0.7% for mesh B and C. However, the free damping simulations shown in Figures 5.28 and 5.29 confirm that the numerical damping ratio increases alongside the wall resolution. The increase between configuration A to B is 5.4%, and from B to C 6.3%.

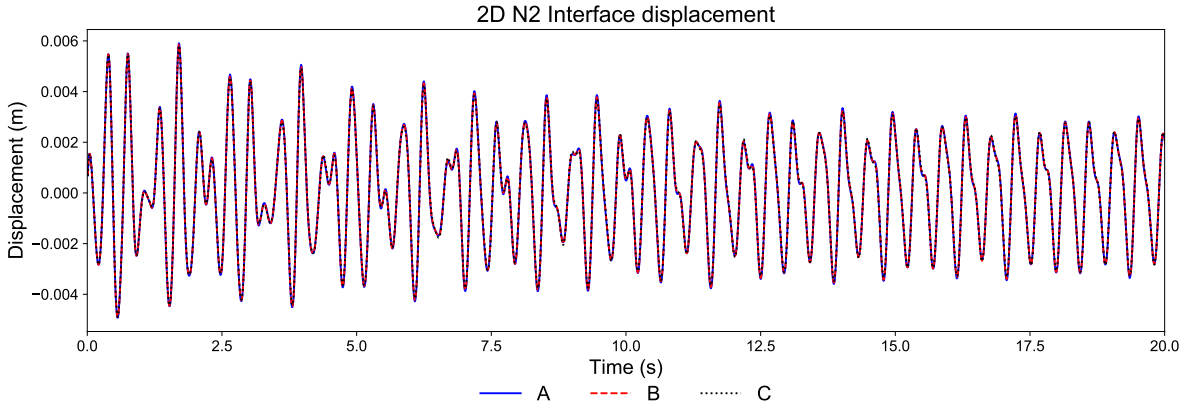

Figure 5.27: Interface displacement between 0 and 20 seconds in the N_2 sloshing cell for different lateral wall refinements.

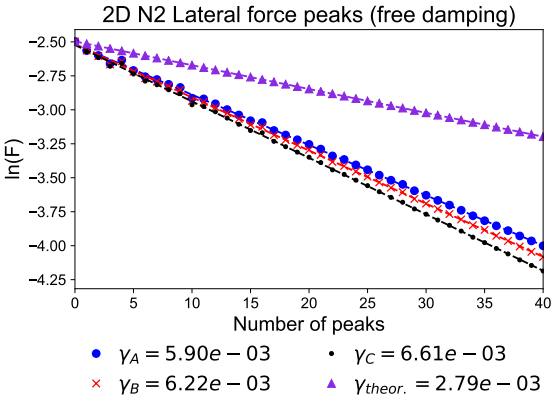

Figure 5.28: Logarithmic decrement for the lateral sloshing force in the N_2 container for different wall resolutions.

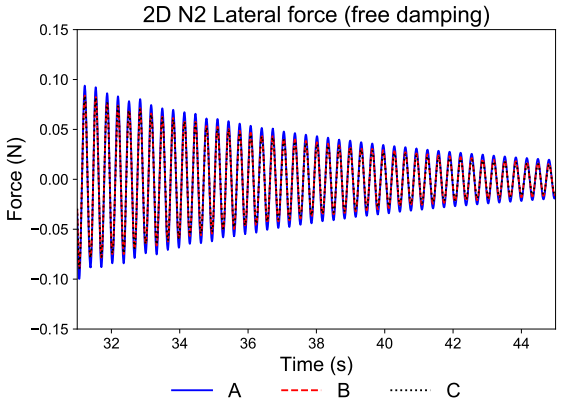

Figure 5.29: Lateral sloshing force for free damping conditions in the N_2 container for different wall resolutions.

These results show that for the tested configurations, although the no-slip velocity boundary condition introduces differences in the damping rate of the system, their effect on the observed sloshing response in negligible.

5.1.2.3 Effect of the temporal scheme

All previously shown simulations were performed using the first-order implicit Euler scheme. As a result, and in an effort to provide more accurate flow results, this section is devoted to studying the effects of using higher-order schemes for the temporal discretization of the governing equations. The base

numerical grid selected for this analysis was grid “N2 03”.

The Crank-Nicolson scheme is implemented in `OpenFoam-v1912` using a weighing coefficient $\gamma \in [0, 1]$ in order to combine both the forward (explicit) and backward (implicit) Euler time-stepping schemes. Equation 5.7 shows the temporal discretization of the generic ODE $\dot{y} = f(t, y)$ using the Crank Nicolson scheme [68]:

$$\frac{y_{n+1} - y_n}{\Delta t} = \gamma f(t_{n+1}, y_{n+1}) + (1 - \gamma) f(t_n, y_n) \tag{5.7}$$

Where, n and $n+1$ are the current and following time-steps, respectively. For $\gamma = 1$, the implicit Euler scheme is obtained, whereas for $\gamma = 0$, the explicit formulation is given. Lastly, if $\gamma = 1/2$, the classic second-order Crank Nicolson scheme is recovered. For stability reasons, OpenFOAM limits the range of the γ parameter to $[0.5, 1]$. Thus, in order to avoid values between 0 and 0.5, the user-input is introduced through an intermediary variable $c_0 \in [0, 1]$ defined as:

$$c_0 = \frac{1 - \gamma}{\gamma}. \tag{5.8}$$

In this formulation $c_0 = 1$ leads to $\gamma = 0.5$, and $c_0 = 0$ yields $\gamma = 1$.

Three different temporal discretizations were considered in this analysis: the implicit Euler scheme, and the Crank-Nicolson scheme with blending coefficients $c_0 = 0.5$ ($\gamma = 0.67$) and $c_0 = 0.9$ ($\gamma = 0.52$). Decreasing c_0 from 1 leads to an increase in numerical dissipation and makes it so the scheme is no longer second-order accurate, however it improves the stability of the solution [68]. Attempts were made to run the 2D sloshing problem with $c_0 = 1$, however the solutions diverged and the simulation crashed every time.

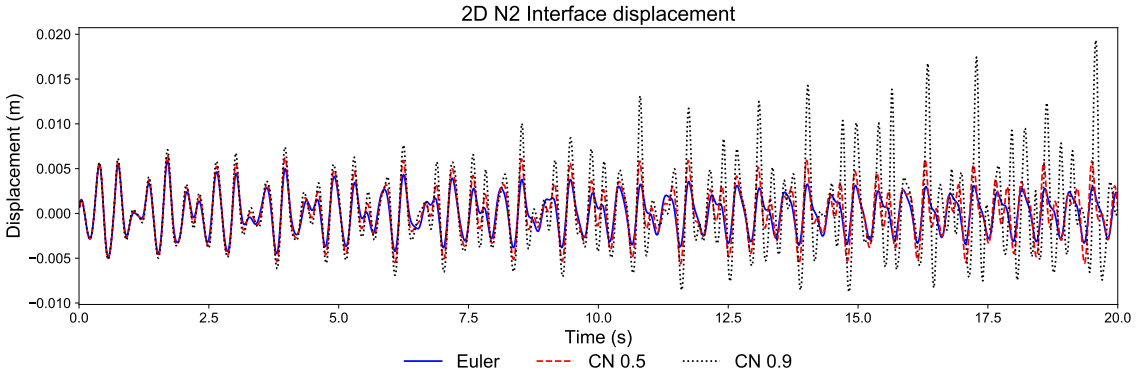

Figure 5.30: Interface displacement between 0 and 20 seconds in the N_2 sloshing cell for different temporal discretization schemes.

Figure 5.30 shows the interface displacement for the N_2 sloshing cell using these three discretization schemes. The Crank Nicolson scheme with $c_0 = 0.9$ yields unphysical results, leading to a rapid increase of the interface displacement as time progresses. On the other hand, $c_0 = 0.5$ shows good agreement with the expected response, with a gradual damping of the wave amplitude until the periodic sloshing condition is reached. Moreover, the rate at which the signal is damped appears to be lower than with the implicit Euler scheme, indicating that numerical dissipation is reduced in this approach.

In order to verify these statements regarding numerical diffusion, the free damping results are shown in Figures 5.31 and 5.32. For $c_0 = 0.9$ the flow continues to amplify its motion even though no excitation is present. However, for $c_0 = 0.5$ the damping characteristics are recovered, and the damping rate yields much lower values than with the first-order implicit Euler scheme (71.7% reduction).

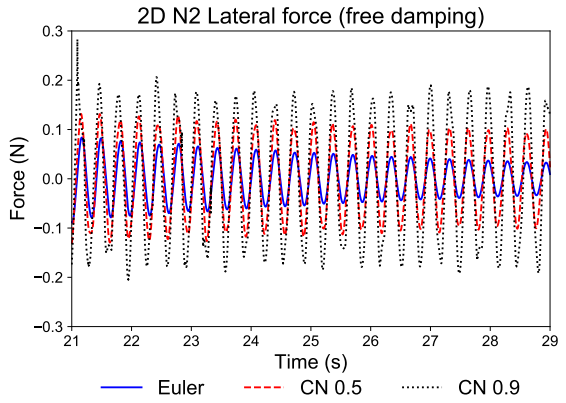

Figure 5.31: Logarithmic decrement for the lateral sloshing force in the N_2 container for different temporal discretization schemes.

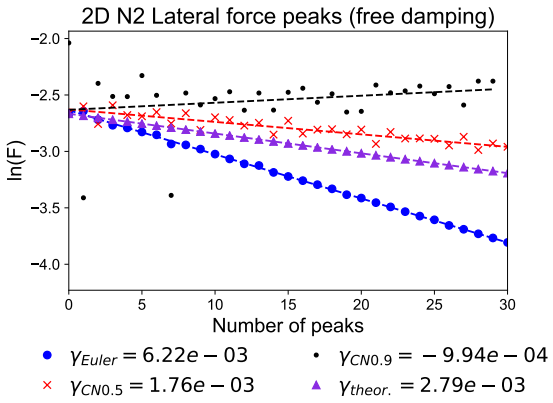

Figure 5.32: Lateral sloshing force for free damping conditions in the N_2 container for different temporal discretization schemes.

Comparing the numerical damping rate of $c_0 = 0.5$ with the theoretical expression from Equation 2.35 ($\gamma_{\text{theor}} = 2.79e-3$), it can be seen that now this numerical estimate is 36.9% lower than the theoretical value. This highlights the difficult nature of modeling viscous damping effects in sloshing problems, and demonstrates why experimental results are required in order to validate the numerical approach.

5.2 Non-isothermal sloshing

The non-isothermal analysis is decomposed in two steps. First, the thermal stratification problem is assessed using the simplified model detailed in Chapter 3. Then, utilizing this thermal field as an input, the non-isothermal sloshing simulations are performed in order to evaluate the similarity of the thermal mixing process in the full-size H_2 facility and in N_2 sloshing cell.

5.2.1 Thermal stratification

The thermal stratification simulations were performed by assuming an initial state where both the gas and the liquid regions have uniform temperatures, T_{gas} and T_{liq}, respectively (refer to Table 3.5). Fixed temperature boundary conditions were used for the top and bottom faces, whereas the lateral walls were considered to be adiabatic. The top face was considered to be at temperature T_{gas} and the bottom T_{liq}. Then, the system was allowed to evolve towards equilibrium, allowing heat transfer to take place between the two phases. The stopping point for these preliminary simulations was based on the Fourier number of the liquid phase:

$$\text{Fo}_{\text{liq}} = \frac{\alpha_{\text{liq}} t}{h^2}. \tag{5.9}$$

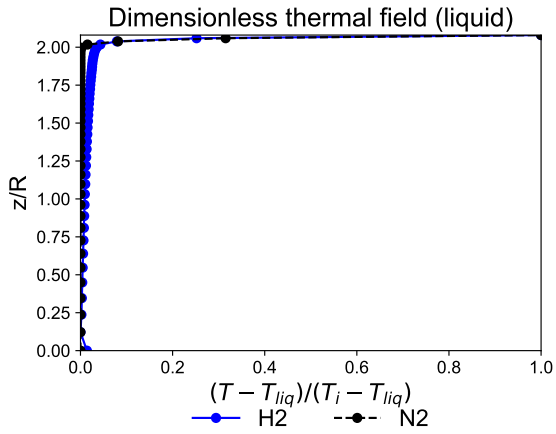

Figure 5.33: Dimensionless H_2 and N_2 thermal profile in the liquid for $Fo_{liq} = 7.16E - 5$.

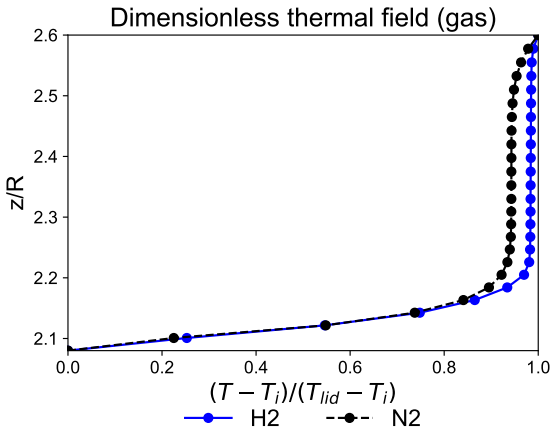

Figure 5.34: Dimensionless H_2 and N_2 thermal profile in the gas for $Fo_{liq} = 7.16E - 5$.

Where h is the liquid height inside the container. This parameter characterizes transient heat conduction problems by relating the rate of diffusive transport with the rate of energy storage [33]. The H_2 thermal stratification simulation was executed for a total of 33 minutes and 20 seconds of physical simulation time, resulting in Fo = $7.16E - 5$. To achieve the same result, the N_2 case only needed to be executed for 1.35 seconds.

Figures 5.33 and 5.34 show the dimensionless thermal profiles for H_2 and N_2 in both the liquid and gas phases at the same liquid-based Fourier time. Good similarity is observed for these fields, however it must be noted that for the full-size H_2 facility, the thermal field was changing very slowly from time-step to time-step. This was not the case for the N_2 sloshing cell, where the fluid experienced fairly drastic changes beyond the 1.35 second mark and only stabilised after t = 100s (Figures 5.35 and 5.36).

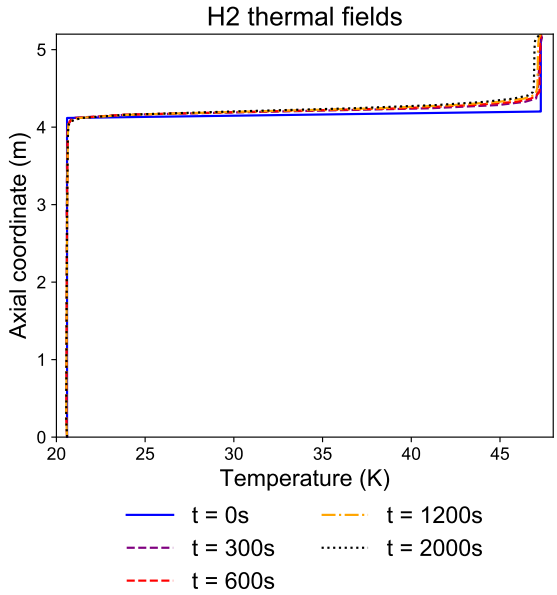

Figure 5.35: Evolution of the thermal fields in the full-size H_2 facility.

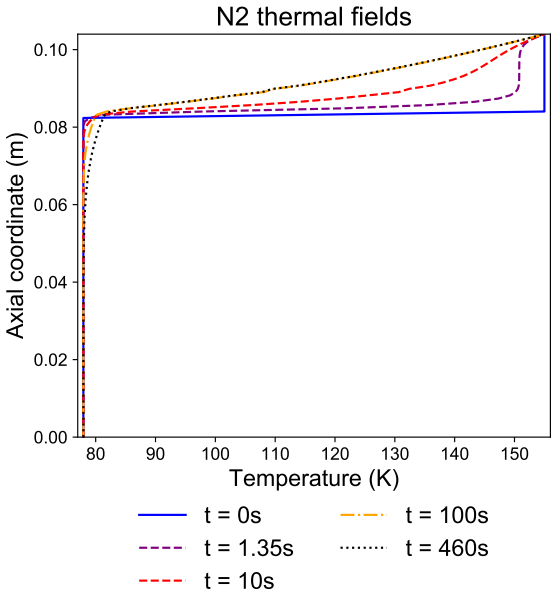

Figure 5.36: Evolution of the thermal fields in the full-size H_2 facility.

This is attributed to the large difference between the container dimensions which causes the thermal

information to propagate significantly slower in the full-size facility. The Fourier number scales with $1/h^2$, which means that in order to keep this parameter similar across both cases, the physical time must be kept over two orders of magnitude smaller in N_2 sloshing cell. This is shown in Figures 5.37 and 5.38 for both the liquid-based and gas-based Fourier numbers.

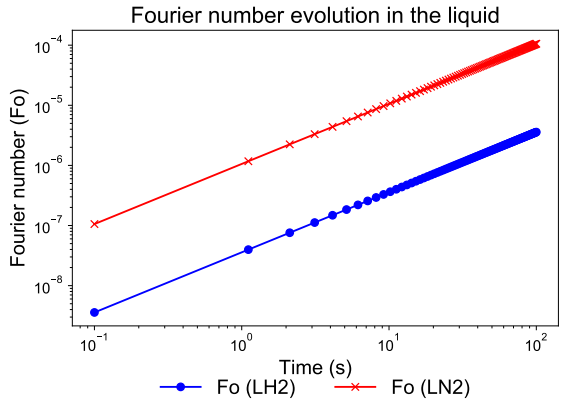

Figure 5.37: Fourier number evolution for the H_2 and N_2 containers in the liquid.

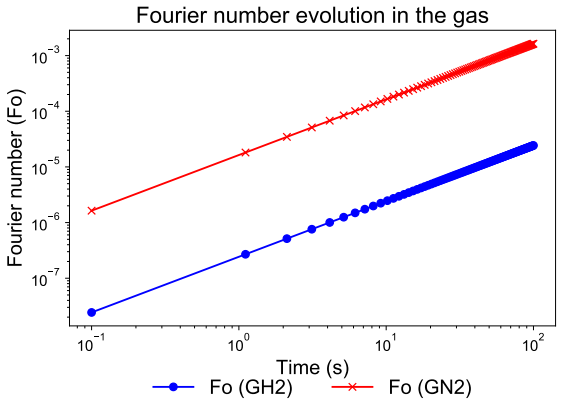

Figure 5.38: Fourier number evolution for the H_2 and N_2 containers in the gas.

Starting the N_2 thermal mixing simulations at t = 1.35s guarantees similarity in terms of the liquid-based Fourier number. Moreover, the dimensionless temperature fields obtained for this point are very similar between the N_2 and H_2 facilities. However, as demonstrated in Figure 5.36, for that instant, the system is still evolving very quickly and very far from equilibrium conditions. As a result, in order to provide additional insights on the effects of the duration of the thermal stratification process on the sloshing-induced mixing, the N_2 thermal field at t = 460s was also be considered as an additional test case.

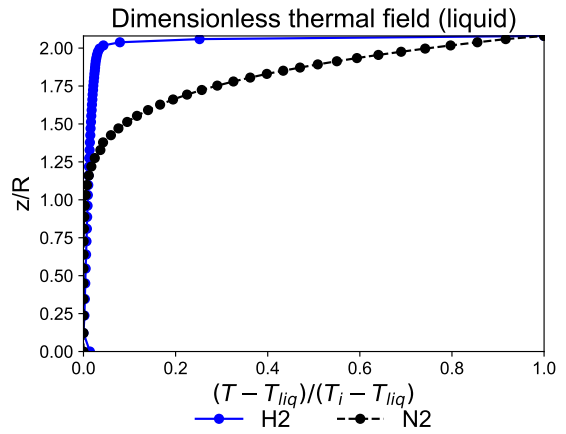

Figure 5.39: Dimensionless thermal fields in the liquid, t_{H2} = 2000s ($Fo_{H2_{liq}}$ = 7.16$E-5$) and t_{N2} = 460s ($Fo_{N2_{liq}}$ = 2.54$E-4$).

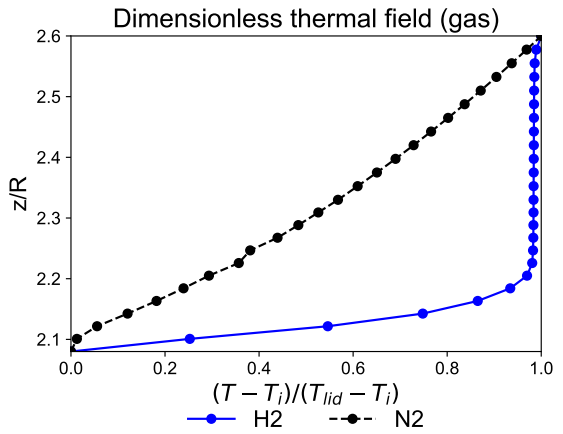

Figure 5.40: Dimensionless thermal fields in the gas, t_{H2} = 2000s ($Fo_{H2_{liq}}$ = 7.16$E-5$) and t_{N2} = 460s ($Fo_{N2_{liq}}$ = 2.54$E-4$).

Therefore, three distinct thermal fields were considered as inputs for the thermal mixing simulations:

1. H_2 thermal field with Fo_{liq} = 7.16$E-5$

2. N_2 thermal field with $Fo_{liq} = 7.16E-5$

3. N_2 thermal field with $Fo_{liq} = 2.54E-4$

5.2.2 Thermal mixing in the chaotic sloshing regime

5.2.2.1 Effect of the wall boundary conditions

These thermal mixing simulations were performed using thermal fields 1 and 2 obtained in the previous section, as the initial conditions. The chosen numerical grid was the three-dimensional '02' configuration (refer to Table 5.1), and unlike previous cases, the simulations were performed in the chaotic sloshing regime with $\Omega/\omega_{11} = 0.9$ and $A_0/R = 0.045$. This allows for the highest degree of mixing to be observed inside the container, thus serving as an indication of the worst-case scenario that might be expected in real world conditions.

Since the solid container is not modeled in the numerical approach of the non-isothermal problem, the effect of different wall boundary conditions is assessed in two different configurations. The two test cases are defined as A and B, and they model two extreme situations for the thermal response of the lateral walls.

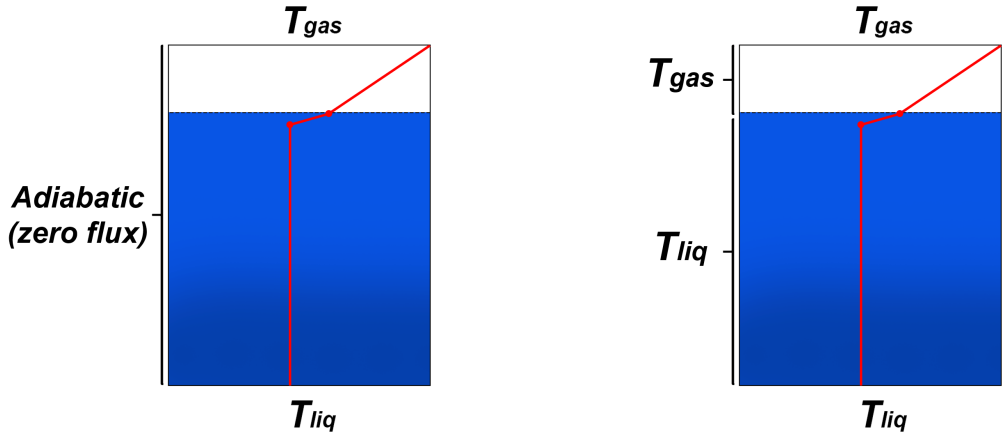

Figure 5.41: Sketch of both sets of boundary conditions to be tested in the thermal mixing analysis. a) Test case A b) Test case B.

Case A considers the lateral walls to be adiabatic, while case B assumes that these are at fixed temperatures. The portion originally in contact with the gas is fixed at T_{gas}, whereas the liquid region is at T_{liq}. In both cases, the upper and the bottom tank walls are assumed to remain at uniform temperature T_{gas} and T_{liq} respectively. The initial thermal fields used for this analysis were the ones obtained for the same liquid-based Fourier number shown in Figures 5.33 and 5.34 (t_{H2} = 2000s and t_{N2} = 1.35s).

The sloshing motion observed for these excitation conditions is decomposed in three main stages:

1. Initial lateral oscillatory displacement of the gas-liquid interface, with a growing wave amplitude until the top of the container is reached. The intensity of the thermal mixing between the gas and liquid phases grows as the wave amplitude increases.

2. High amplitude lateral motion, with the sloshing wave repeatedly reaching the top of the container. This leads to the highest observed rate of thermal mixing between the gas and the liquid, and as a result the thermal fields become more homogeneous.

3. As the high amplitude waves decrease in amplitude, a *swirling* wave motion sets in the containers. The exact starting point for this behaviour varies on a case-by-case basis, depending on the working fluid and the thermal field.

The average dimensionless temperature of the interface, given by:

$$T_i^* = \frac{T_i - T_{liq}}{T_{gas} - T_{liq}} \tag{5.10}$$

was monitored throughout the simulation, and its evolution is plotted alongside the dimensionless time $t^* = tA_0\Omega/R$ in Figure 5.42. The solid lines correspond to the case where the side-walls are adiabatic (case A) and the dotted ones are for the fixed temperature situation (case B). An initial temperature drop is observed until $t^* \approx 0.82$ for both H_2 cases and for the N2(A) configuration, after which point a strong oscillatory behaviour is registered. The N_2 case with the fixed temperature side-walls (B) experiences a very sharp drop in interface temperature until $t^* = 0.19$ followed by a slight increase until $t^* \approx 0.82$.

In spite of the registered oscillations, the interface temperature tends to decrease in both H_2 configurations (A and B) over time. However, for the N_2 case, two different behaviours are observed depending on the side-wall boundary conditions. For the N2(A) configuration, the start of the oscillatory period is accompanied by a considerable increase of T_i^* until $t^* \approx 1.48$. After this point and until $t^* \approx 5.32$ the oscillations appear to be centered around a fixed value. Then after $t^* \approx 5.32$, a steady decrease of T_i^* is observed. On the other hand, for the N2(B) configuration the oscillatory behaviour persists throughout the full simulation duration, with an overall increase of T_i^* as time progresses.

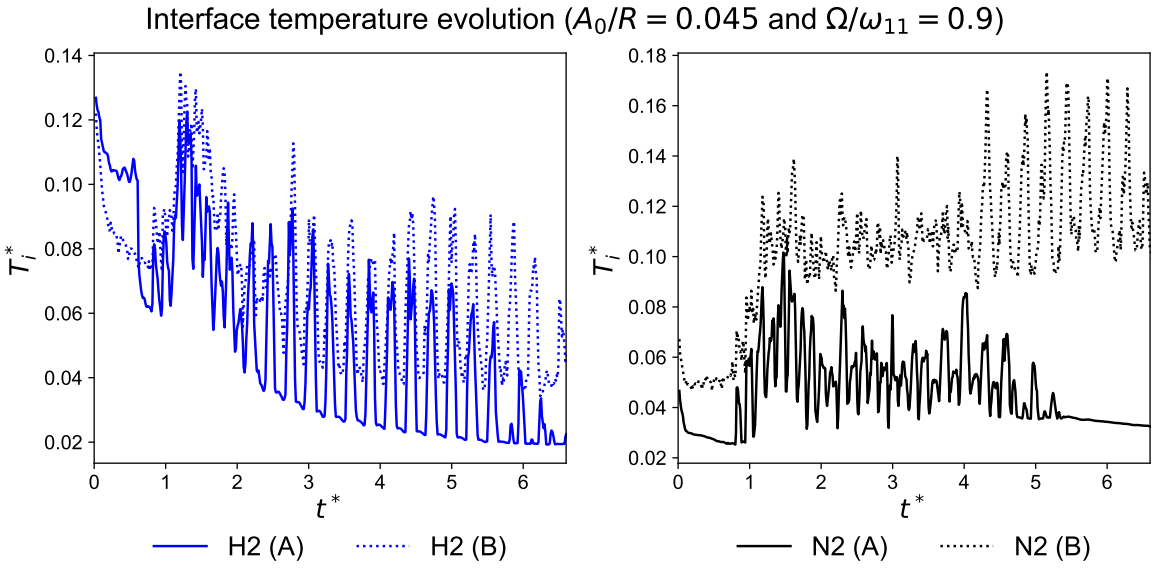

Figure 5.42: Dimensionless interface temperature evolution for the H_2 and N_2 containers in chaotic sloshing conditions. Case A: adiabatic tank side-walls, case B: fixed-temperature tank side-walls.

These diverging results for the evolution of the interface temperature between the H_2 and N_2 facilities are problematic because, as mentioned in Chapter 2, the interface is considered to be at saturation conditions $T_{sat} = T_i$. Following the Clausius-Clapeyron law (Equation 2.17), the saturation temperature of the system directly affects the pressure of the vapour phase, which means that a decrease in T_{sat} causes a decrease in p_{vap} and *vice-versa*. This means that for the current scaled-down configuration, this mechanism is not working accordingly to what was expected from the full-size facility results. Therefore, condensation and evaporation effects would likely differ significantly between the full-size and scaled-down facilities if they were taken into account in this analysis.

The relative pressure drop p/p_0, where p_0 is the initial tank pressure prior to sloshing, is shown in Figure 5.43 for all tested cases. As mentioned previously, condensation or evaporation effects are not taken into account in this modeling approach. Therefore, the drop in pressure is only attributed to the decrease of the gas' density due the cooling down of this region promoted by the sloshing-induced thermal mixing.

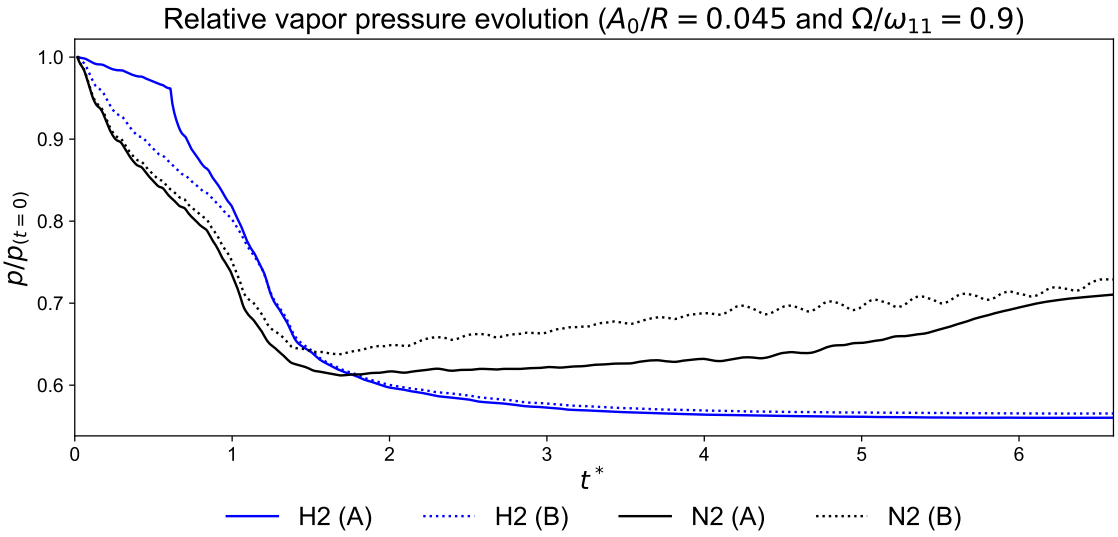

Figure 5.43: Relative tank pressure evolution for the H_2 and N_2 containers with different wall boundary conditions applied.

Figure 5.43 shows that the sloshing-induced thermal mixing causes a steady drop in pressure both tested configurations of the full-size H_2 facility (A and B). The main difference lies in the first instants of sloshing up to $t^* \approx 1.07$. For this period, case (B) registers a lower relative vapour pressure than case (A). This is in agreement with the results from Figure 5.42 since it corresponds to the initial stage where the dimensionless interface temperature decreases very rapidly, which suggests that the ullage is being cooled down at a high rate. Figures 5.44 and 5.45 show the interface position and the dimensionless temperature fields for configurations H2(A) and H2(B) for the first instants of sloshing. The dimensionless temperature field is obtained as:

$$T^* = \frac{T - T_{liq}}{T_{gas} - T_{liq}}. \tag{5.11}$$

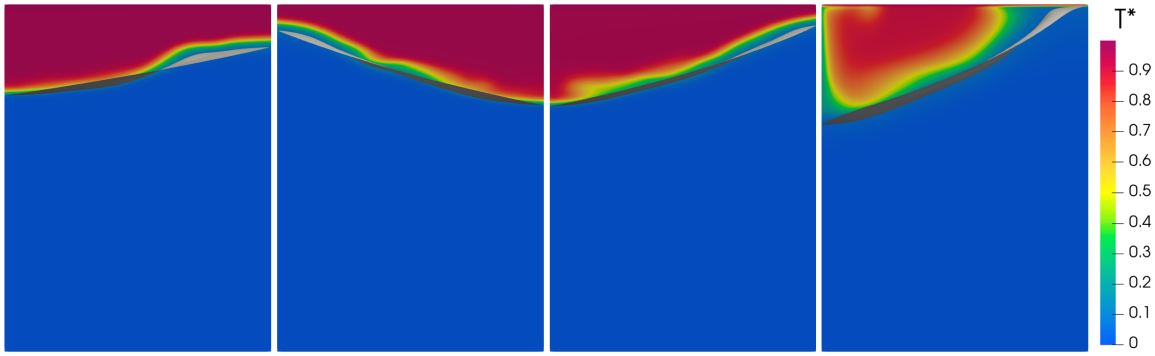

Figure 5.44: Dimensionless thermal fields and interface position for the H2(A) case at t^* = 0.27 (far left), t^* = 0.40 (center left), t^* = 0.53 (center right) and t^* = 0.81 (far right).

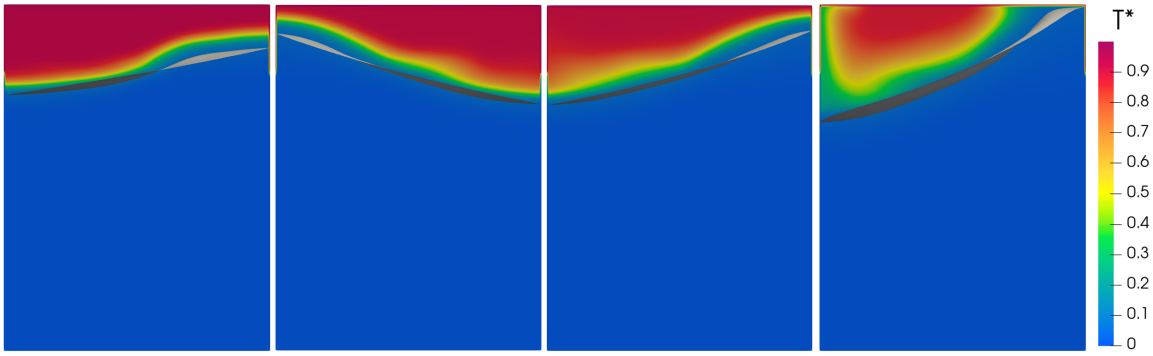

Figure 5.45: Dimensionless thermal fields and interface position for the H2(B) case at t^* = 0.27 (far left), t^* = 0.40 (center left), t^* = 0.53 (center right) and t^* = 0.81 (far right).

These figures show that the H_2 gas phase is cooled down more efficiently in case (B) than (A) during the initial instants of sloshing. The existence of two fixed-temperature regions in the container side-walls causes the fluid to warm up while passing through the portion at T_{gas} and to cool down in portion at T_{liq}. For the H2(B) configuration, the sloshing-induced thermal mixing and the choice of values for T_{gas} and T_{liq} are such that the cooling down of the ullage due to thermal mixing is more effective.

Figure 5.46 shows the velocity field generated by the sloshing-induced thermal mixing that takes place below the interface. This process allows for the warmer liquid at the free-surface to mix with the colder bulk, hence decreasing the value of T_i.

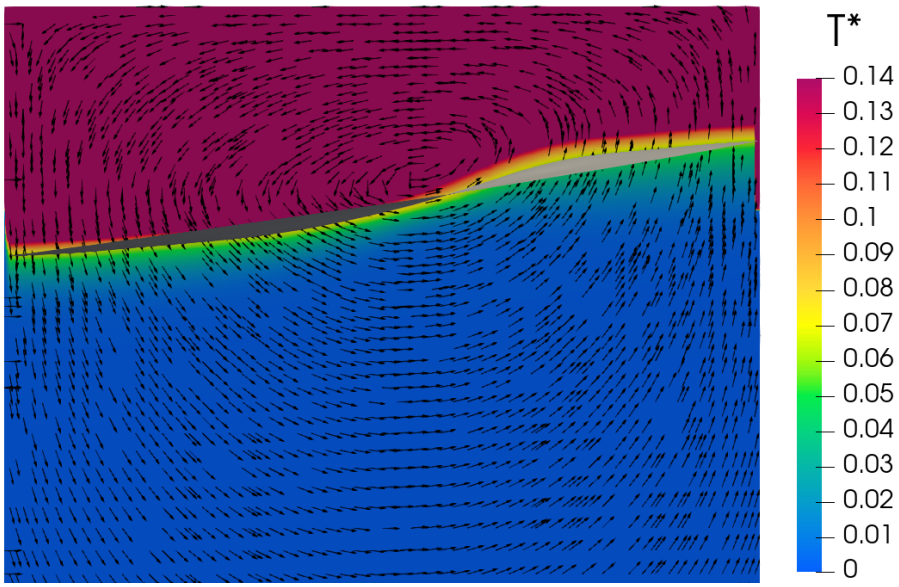

Figure 5.46: Dimensionless thermal and velocity fields for the H2(A) case at $t^* = 0.26$.

These are the mechanisms which trigger the large pressure drop, and decrease in interface temperature observed in the initial stages of Figure 5.43 and 5.42. After this point, the amplitude of the sloshing wave grows to the point where it reaches the top of the container at fixed temperature T_{gas}. This period is observed until $t^* \approx 5.84$ and is characterized by high amplitude waves which very quickly and effectively mix the thermal field. At this stage, as shown by Figure 5.43, although the relative vapour pressure evolution is nearly identical between both H_2 configuration, the pressure drop is slightly stronger for test case (A). Once again this is in agreement with Figure 5.42, which shows that T_i^* is higher for test case (B) throughout the high amplitude sloshing stage.

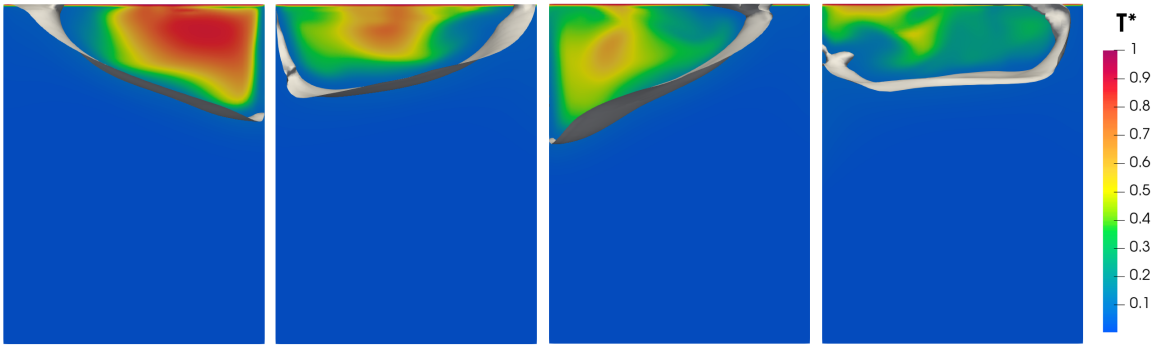

Figure 5.47: Dimensionless thermal fields and interface position for the H2(A) case at $t^* = 0.96$ (far left), $t^* = 1.08$ (center left), $t^* = 1.13$ (center right) and $t^* = 1.21$ (far right).

The start of the swirling motion in both cases of the H_2 facility starts at $t^* \approx 5.84$. At this point, the thermal fields are already de-stratified and the vapour pressure achieves a very stable value ($\approx$ 56% of the initial pressure). The high intensity lateral waves gradually decrease their amplitude and adopt an axial rotating motion. After some periods, the interface becomes approximately flat and the *swirling* motion becomes much better defined. The de-stratified fields and the *swirl* waves are shown in Figure 5.49 between $t^* = 6.09$ and $t^* = 6.26$ for case H2(A). For clearer visualization purposes, as the thermal

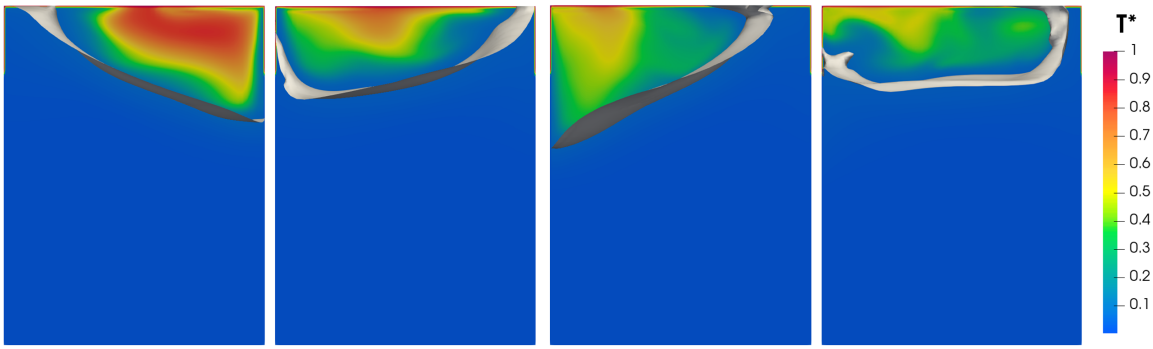

Figure 5.48: Dimensionless thermal fields and interface position for the H2(B) case at t^* = 0.96 (far left), t^* = 1.08 (center left), t^* = 1.13 (center right) and t^* = 1.21 (far right).

field is very homogeneous at this point, the dimensionless temperature scale was adjusted to be between 0 and 0.025.

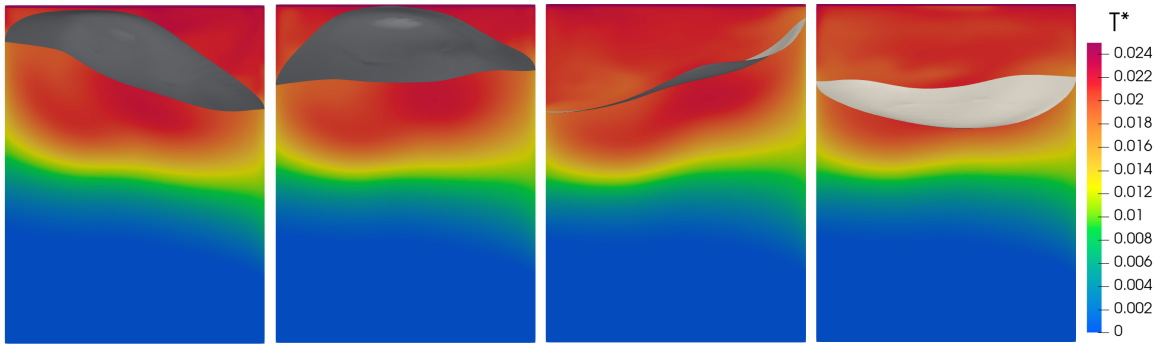

Figure 5.49: Dimensionless thermal fields and interface position for the H2(A) case at t^* = 6.09 (far left), t^* = 6.14 (center left), t^* = 6.20 (center right) and t^* = 6.26 (far right).

Regarding the two N_2 configurations, Figure 5.43 shows that the relative pressure drop is slightly higher for case N2(B) during the initial sloshing period. This is in accordance with the dimensionless interface temperature evolution shown in Figure 5.42, which indicates T_i^* to be higher for case N2(B). Figures 5.50 and 5.51 show the dimensionless thermal fields for case N2(A) and N2(B) in the initial moments of sloshing until the rising wave reaches the top of the container. Appreciable differences are not found between both sets of images, which is in agreement with the fact that the pressure evolution, although slightly higher in case N2(B), is very similar between both configurations.

After the sloshing wave reaches the top of the container, the high amplitude lateral displacement stage is reached. Similarly to what was observed in the H_2 facility, the thermal mixing effect is very strong in this period, leading to the rapid homogenization of the thermal field between t^* = 0.82 and t^* = 1.7. This can be observed in Figures 5.52 and 5.53.

However, unlike what was observed in the full-size facility, after $t^* \approx 1.7$ the presence of the warmer walls at T_{gas} coupled with the high amplitude sloshing leads to a gradual increase in the ullage temperature which in turn causes the pressure in the tank to steadily increase (Figure 5.43). This is particularly noticeable for case N2(B), where not only the top is at temperature T_{gas} but also the upper portion (20%) of the side-walls. This is attributed to the smaller container scale, which makes it so that thermal information travels more quickly throughout the domain due to diffusion compared to the full-size facility. This

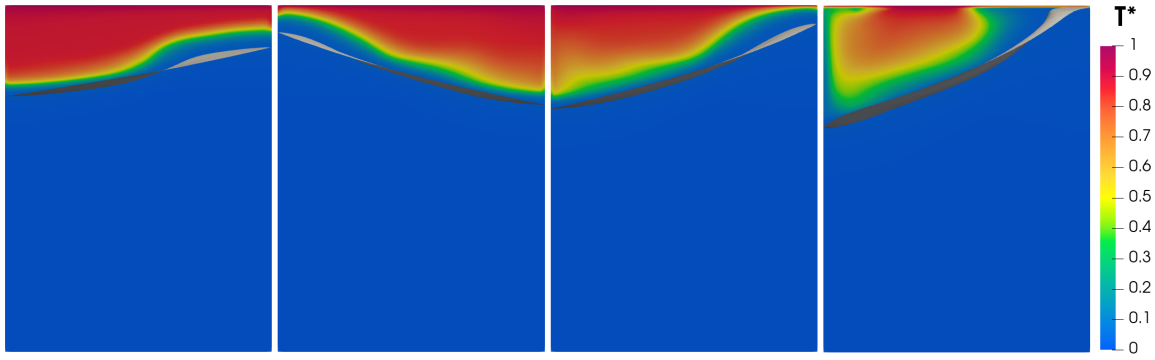

Figure 5.50: Dimensionless thermal fields and interface position for the N2(A) case at t^* = 0.27 (far left), t^* = 0.40 (center left), t^* = 0.53 (center right) and t^* = 0.81 (far right).

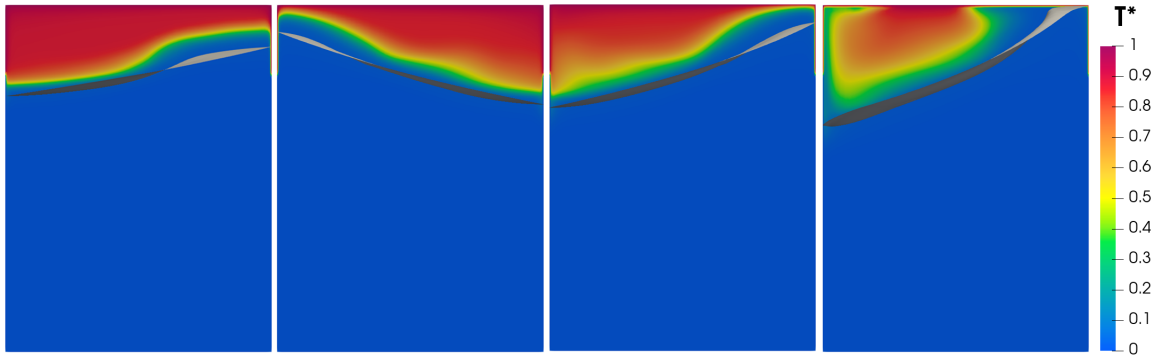

Figure 5.51: Dimensionless thermal fields and interface position for the N2(B) case at t^* = 0.27 (far left), t^* = 0.40 (center left), t^* = 0.53 (center right) and t^* = 0.81 (far right).

is the same effect that was discussed in the thermal stratification simulations performed in Section 5.2.1. As a result, the N_2 sloshing cell is found to be much more sensitive to the wall-boundary conditions than the full-size H_2 tank.

The swirling motion is observed in case N2(A) at $t^* \approx 4.52$ and $t^* \approx 5.99$ for N2(B). Thermal mixing is still observed near the interface, as evidenced by the evolution of T_i^* in Figure 5.42. However, the top section of the tank is not mixed as effectively as in the previous stages. As a result, warm gas can be seen travelling downwards from the heated walls at T_{gas}. This partly undoes the mixing that was performed previously in the high amplitude stage and leads to an additional increase in vapour pressure due to the warming up process of the ullage. Figures 5.54 and 5.55 show the *swirling* motion in the N_2 alongside the warmer gas travelling downward from the walls at fixed temperature T_{gas}.

In summary, the results of this section reveal that although an initial pressure drop is observed in all test cases, the behaviour observed for these excitation conditions in scaled-down N_2 facility is considerably different than one that takes place in full-size H_2 tank. The N_2 sloshing cell appears to be significantly more sensitive to the presence of the warmer walls, leading to a gradual heating up of the gas and liquid phases during the high amplitude sloshing stage.

The non-isothermal scaling approach was based on the buoyancy of the liquid through the $(\pi_3)_{liq}$ parameter, which is the main mechanism for thermal mixing only in the initial sloshing moments until the wave reaches the top of the container. Up until this point, cases H2(A), H2(B) and N2(A) operate quite similarly, as shown in Figures 5.42, 5.43, 5.44, 5.45 and 5.50. However, after that, the heat transfer

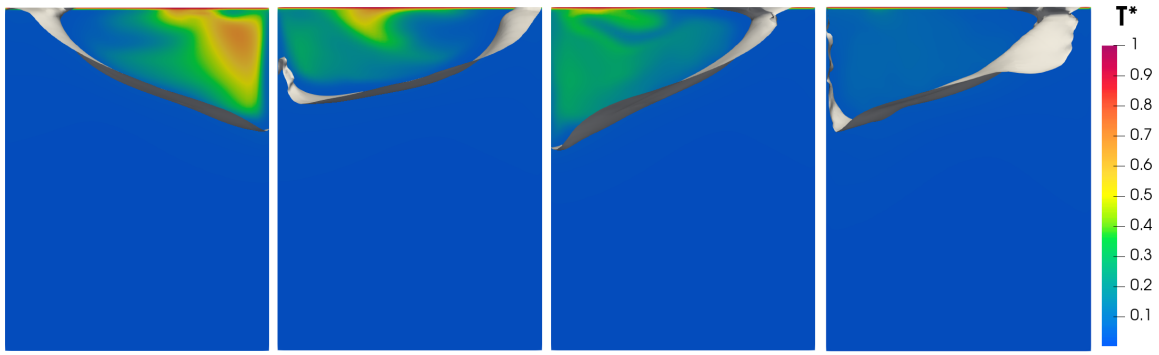

Figure 5.52: Dimensionless thermal fields and interface position for the N2(A) case at t^* = 0.96 (far left), t^* = 1.08 (center left), t^* = 1.13 (center right) and t^* = 1.7 (far right).

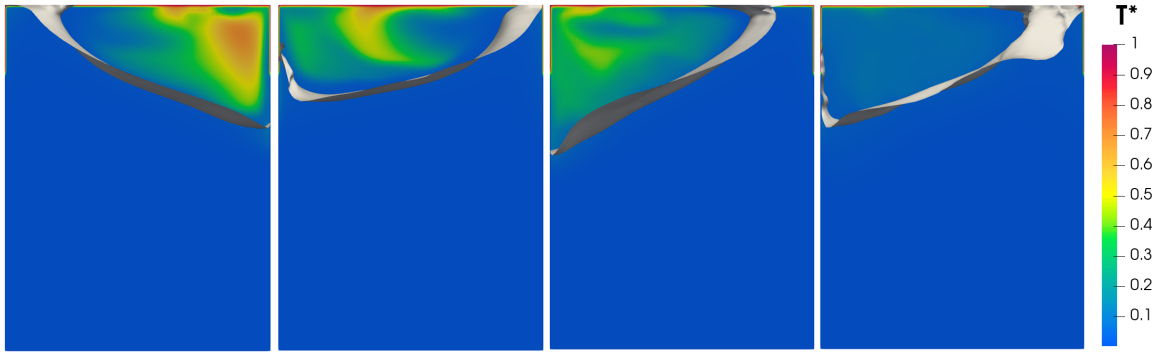

Figure 5.53: Dimensionless thermal fields and interface position for the N2(B) case at t^* = 0.96 (far left), t^* = 1.08 (center left), t^* = 1.13 (center right) and t^* = 1.7 (far right).

mechanisms become more complex due to the active participation of the fixed temperature walls, and due to stronger convective gas fluxes in the ullage volume. Thus, since these are not directly accounted for in the scaling approach, the current model is not well equipped to deal with this.

5.2.2.2 Effect of the initial temperature field

The goal of this section is to compare the effects of considering different thermally stratified thermal fields as inputs for the thermal mixing simulations. As a result, three cases are compared in this analysis:

- N_2 with adiabatic side-walls and initial thermal field 2 ($Fo_{liq} = 7.16E-5$) (A2)
- N_2 with fixed temperature side-walls and initial thermal field 2 ($Fo_{liq} = 7.16E-5$) (B2)
- N_2 with fixed temperature side-walls and initial thermal field 3 ($Fo_{liq} = 2.54E-4$) (B3)

The longer thermal stratification duration considered in simulation (B3) leads to a thermal field which is closer to equilibrium conditions than cases (A2) and (B2) (refer to Figure 5.36). As a result, the thermal gradients in gas and liquid phases are smaller in case (B3). Therefore, during the initial sloshing moments before the rising wave reaches the top of the container, the thermal mixing that takes place below the interface, and that is responsible for the initial pressure drop and decrease in interface temperature, is not as effective in case (B3). This is confirmed in Figure 5.56, where the dimensionless interface temperature in case (B3) only suffers a very gradual decrease compared to the sharp drop seen for initial instants in cases (A2) and (B2).

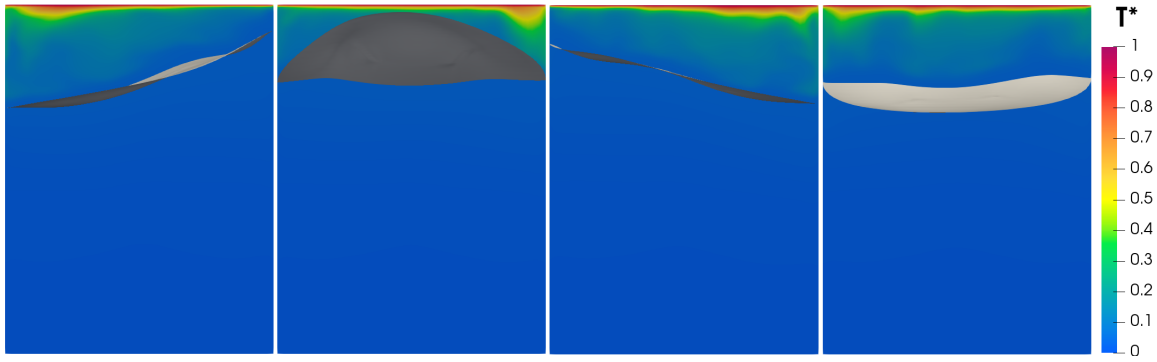

Figure 5.54: Dimensionless thermal fields and interface position for the N2(A) case at t^* = 5.56 (far left), t^* = 5.64 (center left), t^* = 5.7 (center right) and t^* = 5.78 (far right).

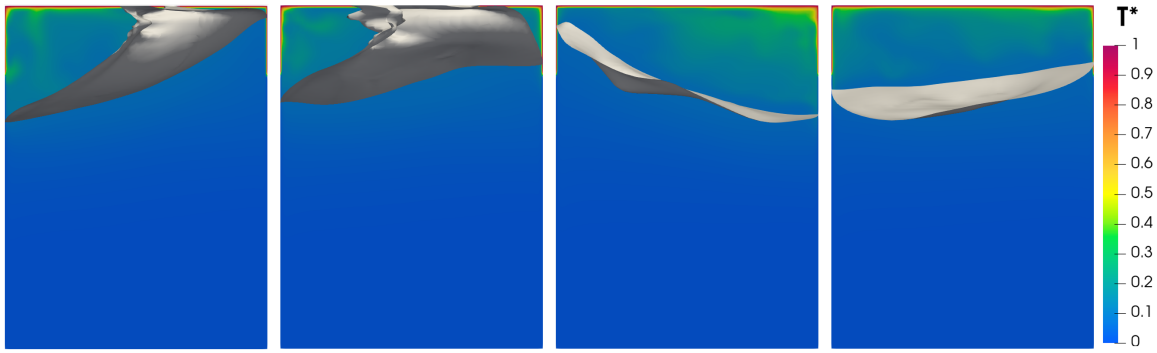

Figure 5.55: Dimensionless thermal fields and interface position for the N2(B) case at t^* = 6.5 (far left), t^* = 6.55 (center left), t^* = 6.63 (center right) and t^* = 6.71 (far right).

Moreover, Figure 5.57 shows that the pressure drop is not as severe for the case with the more developed initial thermal field. Once again, this is explained by the smaller difference in temperature between the gas and the liquid, which causes the mixing near the interface to not be as effective as in the other cases.

As the high amplitude sloshing stage sets in, the interface temperature and vapor pressure evolutions in case (B3) are identical to the ones observed in (A2) and (B2). The high amplitude mixing, alongside the initial thermal field are shown in Figure 5.58 for case N2(B3). As the wave height starts to decrease at $t^* \approx 4.52$, the interface adopts a *swirling* motion. This causes the interface temperature to gradually stabilize (Figure 5.56), while also allowing for heat to travel from the walls at T_{gas}, hence warming up the ullage and leading to a greater rate of pressure increase (similar to case (A2)).

5.2.3 Thermal mixing in the planar waves sloshing regime

With the objective of analysing the validity of the non-isothermal scaling approach for different sloshing regimes, the thermal mixing simulations were also performed for the planar waves regime with dimensionless excitation parameters: A_0/R = 0.045 and Ω/ω_{11} = 0.7.

5.2.3.1 Effect of the wall boundary conditions

The tested boundary condition configurations are the same ones that were described in Section 5.2.2.1. Once again, initial thermal fields 1 and 2 are used for the full-size facility and small-scale model, respec-

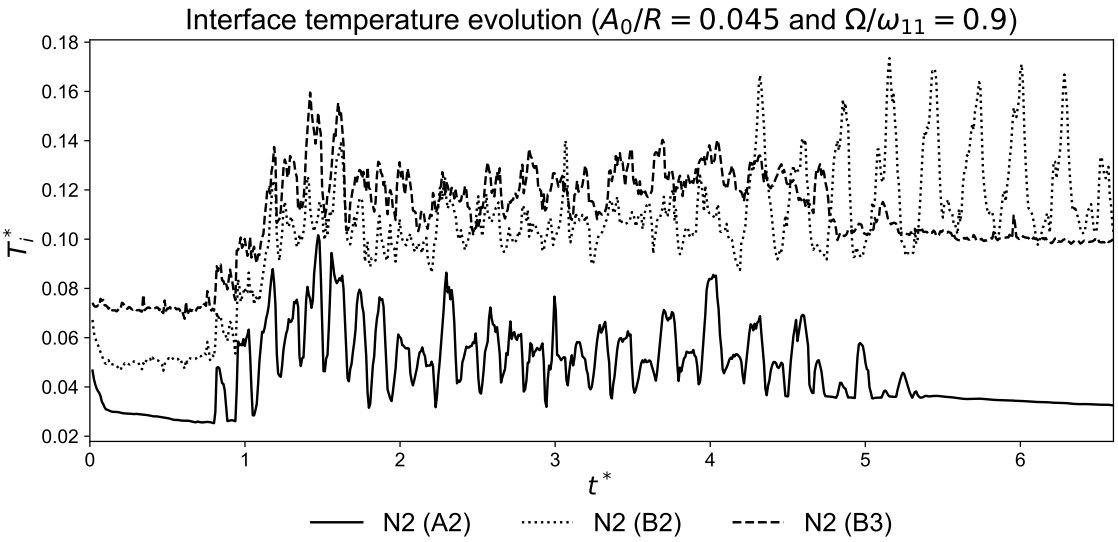

Figure 5.56: Dimensionless interface temperature evolution for the H_2 and N_2 containers in chaotic sloshing conditions for different durations of initial thermal stratification.

tively. The only difference in terms of setup lies in the dimensionless excitation conditions, and on the observed sloshing regime. For this section, only linear sloshing and planar waves are expected.

For these conditions, thermal mixing between the gas and liquid phases is mainly achieved through the mechanism shown in Figure 5.46. The fluid in the downward side of the planar wave is pushed to the bottom of the container, where it is cooled down by the bulk, and the fluid in the upward side of the planar wave receives colder liquid from the bottom, thus decreasing its temperature.

Figure 5.59 shows the evolution of the dimensionless interface temperature as the sloshing motion evolves throughout time. Cases H2(A) and H2(B) are characterized by an overall decrease in interface temperature, which slows down as the time thermal field approaches equilibrium. Case N2(A) presents a very sharp initial temperature drop until $t^* \approx 0.1$, then it increases slightly until $t^* \approx 0.76$, and afterwards, a very gradual decrease is observed until the end of the simulation. On the other hand, case N2(B) presents a behaviour that is very different from all other tested situations. For this situation, there is an initial sharp drop until $t^* = 0.08$, which is followed by a progressive increase of T_i^* until the the end.

The relative pressure evolution for the H_2 and N_2 test cases is shown in Figure 5.60. The behaviour shown in this plot is in agreement with the observations made regarding the T_i^* evolution. Cases H2(A), H2(B) and N2(A) all show an overall decrease in T_i^* during this simulation. This suggests that the sloshing-induced thermal mixing promotes a general cooling down of the ullage due to the presence of the colder liquid. As a result, these three cases are all characterized by a steady pressure drop. The biggest decrease in pressure takes place in the N2(B) facility (87% of the initial value). It should be noted that the pressure drops observed in this sloshing regime are significantly lower than the ones observed for the chaotic regime from Figure 5.43. This is attributed to higher mixing rate that is promoted by the higher amplitude waves in that situation.

On the other hand, case N2(B) shows an overall increase in T_i^* as well as p/p_0 during the simulation. This case models the extreme scenario in which the portion of the side-walls initially in contact with the

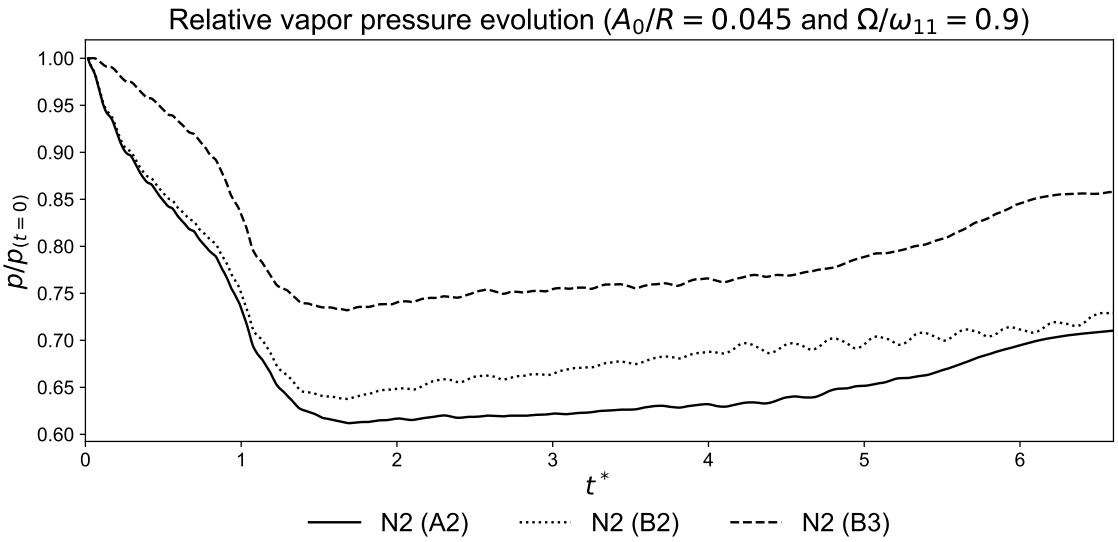

Figure 5.57: Relative tank pressure evolution in the H_2 and N_2 containers for different durations of initial thermal stratification.

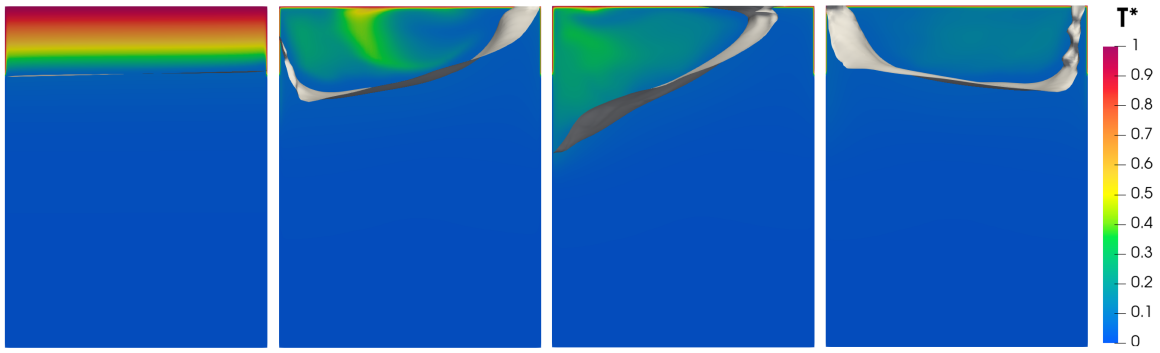

Figure 5.58: Dimensionless thermal fields and interface position for the N2(B3) case at t^* = 0.01 (far left), t^* = 1.08 (center left), t^* = 1.13 (center right) and t^* = 1.2 (far right).

gas (top 20%) has fixed temperature T_{gas}, and the remaining portion (bottom 80%) is at T_{liq}. These results suggest that, for the current excitation conditions, the presence of the warmer walls overcomes the sloshing-induced thermal mixing, causing an increase in the ullage temperature. This is the opposite of what is expected from the full-size facility results.

Figures 5.61 and 5.62 show the thermal fields and the gas-liquid interface for the N2(A) and N2(B) cases, respectively, for different time instants. The N2(A) sequence of images shows the gradual cooling down of the ullage due to the presence of the colder liquid. The thermal mixing that happens below the interface allows for the free surface to remain cold, while gradually exchanging heat with the gas to decrease its temperature. On the other hand, in case N2(B), the presence of the lateral and top walls at T_{gas} counteracts the cooling mechanism of the liquid, leading to a gradual increase in temperature from the top of the container to the bottom.

This section reveal that for planar sloshing conditions, reasonable results are obtained in terms of the similarity of the thermodynamic evolution of the system except for case N2(B) due to the extreme wall boundary conditions. The scaling approach adopted in this work seems to be more well suited to these

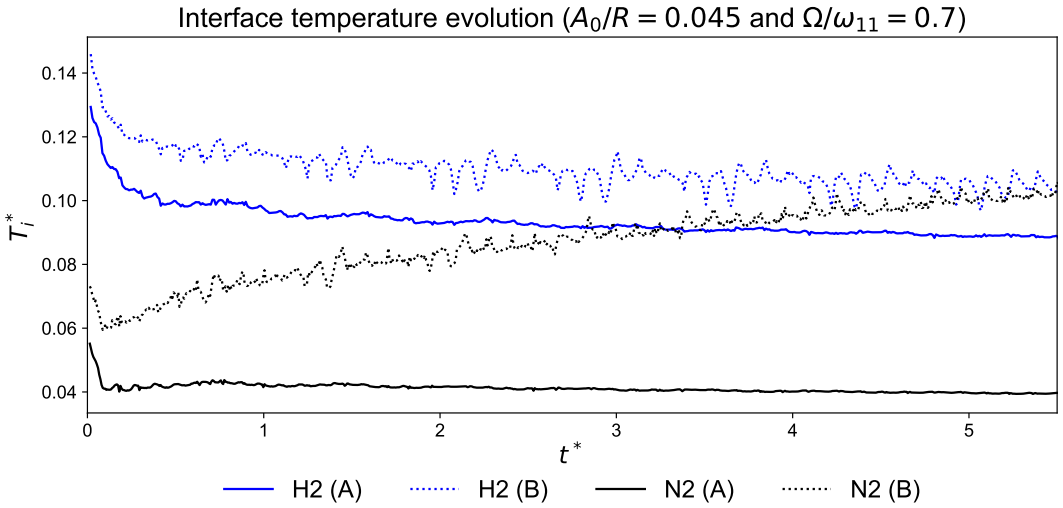

Figure 5.59: Dimensionless interface temperature evolution for the H_2 and N_2 containers in planar sloshing conditions.

lower excitation situations. The logical next step would be to perform this same analysis while modeling the solid tank walls in order to account for conjugate heat transfer, and thus determine the true impact of the wall's properties in real life conditions.

5.2.3.2 Effect of the initial temperature field

With the objective of comparing the effects of considering different thermally stratified thermal fields as inputs for the thermal mixing simulations, the same test cases from Section 5.2.2.2 (A2,B2,B3) were considered.

The dimensionless interface temperature for cases N2(A2), N2(B2) and N2(B3) is shown in Figure 5.63. The plot reveals that the more developed initial thermal field of case N2(B3) leads to a higher increase in T_i^* as time progresses. Moreover, from Figure 5.64, the relative tank pressure in this case doesn't show a drop at all. Instead the ratio p/p_0 tends to increase since the start of the simulation.

Figure 5.65 shows the evolution of the dimensionless thermal fields and interface position as time progresses in the N2(B3) case. From these images, it is clear that, similarly to what happened in case N2(B2), the presence of the warmer walls at T_{gas} is overcoming the cooling effect of the thermal mixing below the interface. Moreover, since the initial thermal field started from a more developed situation, the thermal gradients near the interface are lower, which translates to a reduction of the mixing effect. As a result, the cooling of the ullage due to the liquid mixing is reduced, meaning that the heating effect of the warm walls is felt with more intensity.

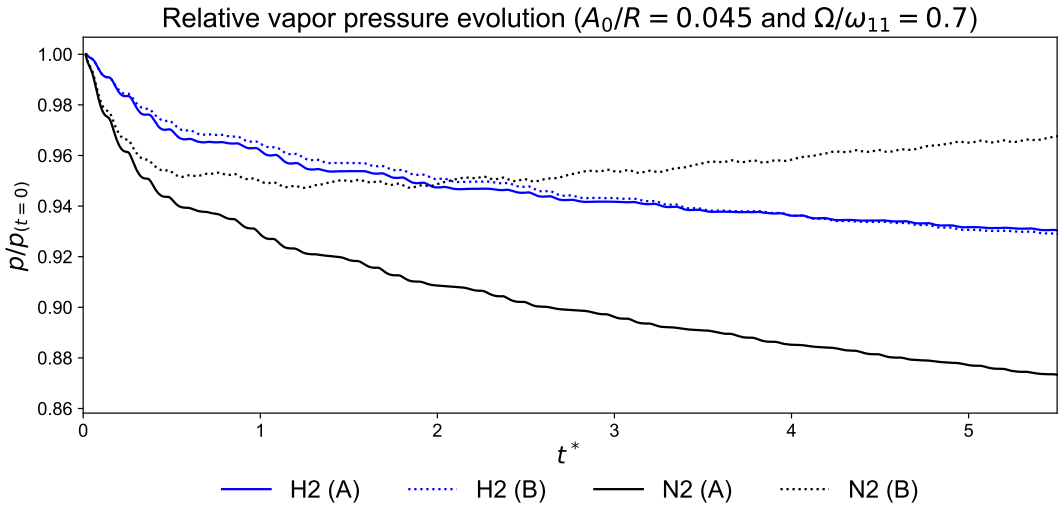

Figure 5.60: Relative tank pressure evolution for the H_2 and N_2 containers, in planar waves conditions, with different wall boundary conditions applied.

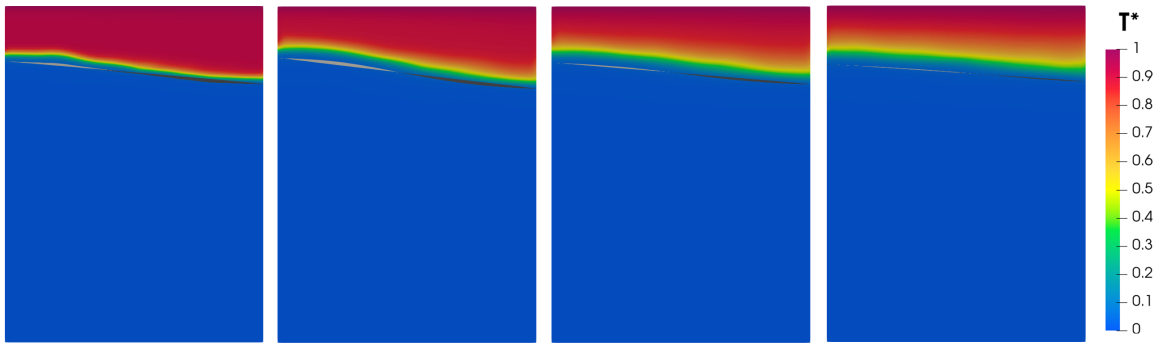

Figure 5.61: Dimensionless thermal fields and interface position for the planar N2(A) case at t^* = 0.16 (far left), t^* = 1.23 (center left), t^* = 3.05 (center right) and t^* = 5.53 (far right).

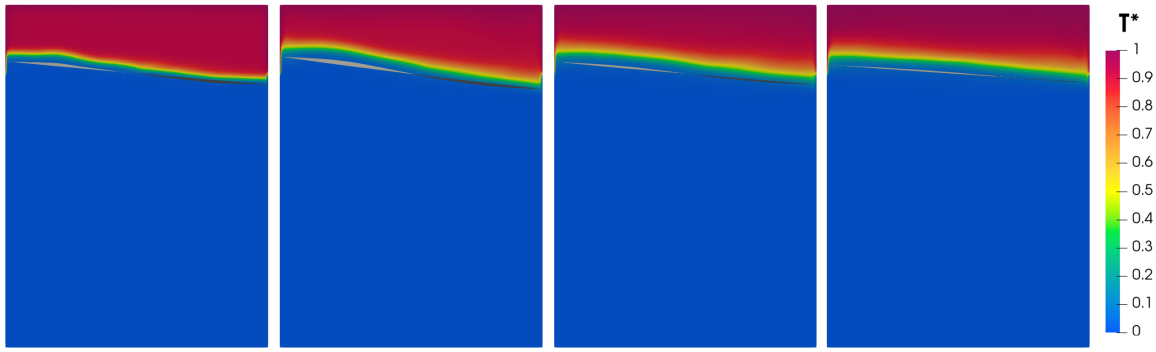

Figure 5.62: Dimensionless thermal fields and interface position for the planar N2(B) case at t^* = 0.16 (far left), t^* = 1.23 (center left), t^* = 3.05 (center right) and t^* = 5.53 (far right).

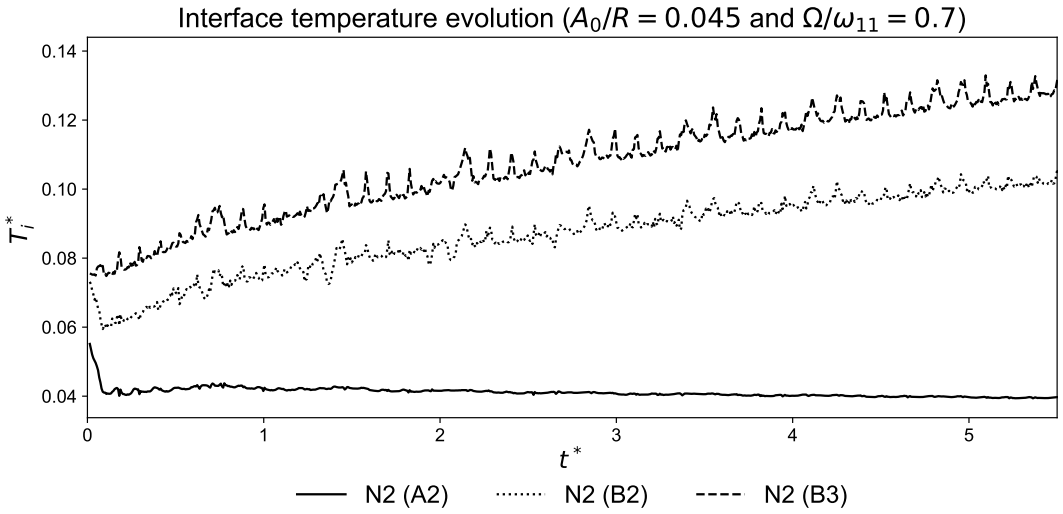

Figure 5.63: Dimensionless interface temperature evolution for the H_2 and N_2 containers in planar sloshing conditions for different durations of initial thermal stratification.

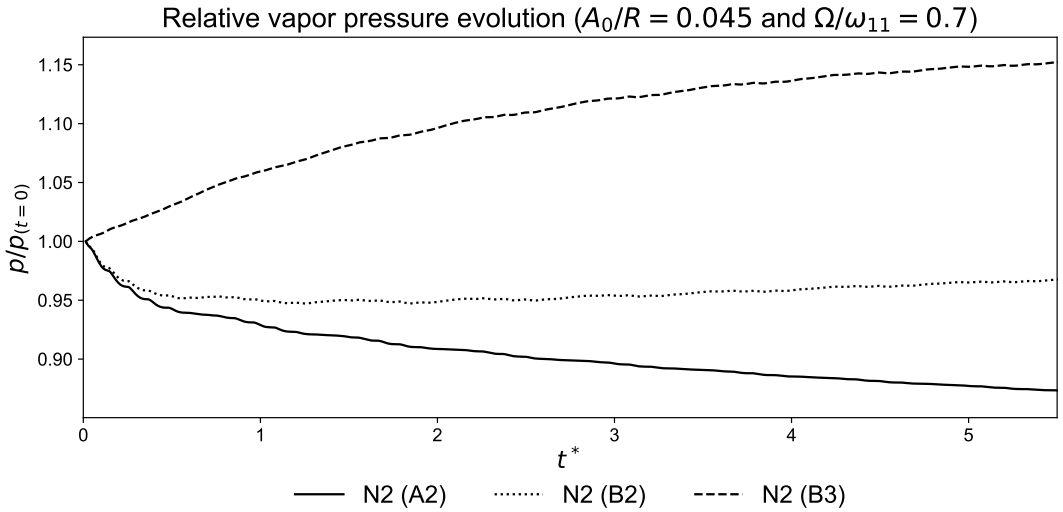

Figure 5.64: Relative tank pressure evolution for the H_2 and N_2 containers in planar sloshing conditions for different durations of initial thermal stratification.

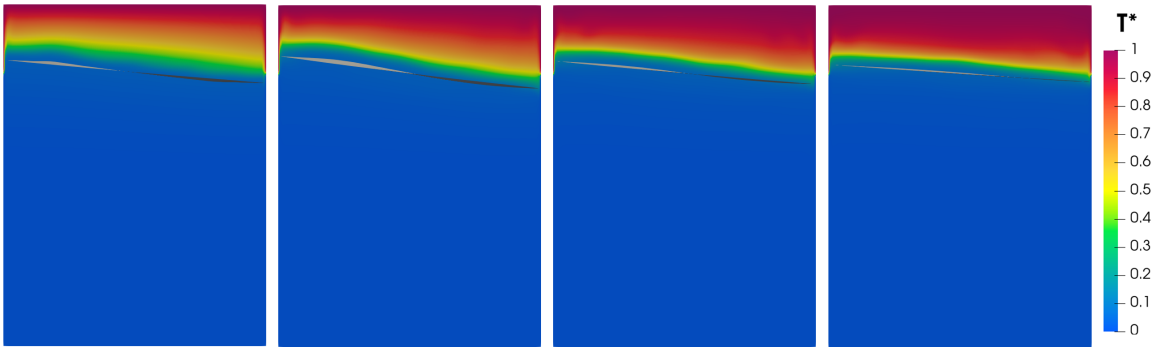

Figure 5.65: Dimensionless thermal fields and interface position for the planar N2(B3) case at t^* = 0.16 (far left), t^* = 1.23 (center left), t^* = 3.05 (center right) and t^* = 5.53 (far right).

Chapter 6

Conclusions and Future work

6.1 Conclusions

The purpose of the work developed in this master thesis was to study the scaling problem for non-isothermal sloshing with the OpenFOAM CFD code. This was achieved by scaling down a full-size facility with dimensions comparable to the cryogenic stages of launch vehicles in order to recreate the system's response in laboratorial conditions.

As a first step in the numerical analysis, isothermal simulations were performed in order to better understand the effect of the numerical discretization on the dynamics of the flow, and to study the isothermal scaling problem. Both 3D and 2D simulations were conducted in the planar waves sloshing regime, with a moving numerical grid to excite the system. The planar waves response of the system was found to be composed by an initial transient regime, which is gradually damped until a steady harmonic motion is achieved. The duration of this transient regime was found to depend on the temporal and spatial resolution of the numerical grid, as well as on the temporal discretization scheme. Moreover, due to the moving contact problem explained in Chapter 4, the placement of the first cell adjacent to the wall also affected the measured numerical damping rates of the system. Good similarity was found between the full-size facility and the scaled-down model for the steady periodic regime in planar sloshing. However, the initial transient state could not be truly compared between both cases due to the presence of excessive numerical dissipation in the three-dimensional grids tested. A great deal of computational resources are required in order to spatially and temporally refine the numerical grids in order match the theoretical damping rates of the systems.

The non-isothermal problem was split in two different components. First, the thermal stratification problem was approached with simplified model detailed in Chapter 3. Then, the thermal fields obtained in this step were used as inputs for the thermal mixing simulations. For these simulations, only the fluids were modeled, and the effect of the solid lateral walls was treated with two extreme cases of boundary conditions (adiabatic or fixed temperature). The thermal mixing problem was analysed in both the chaotic and planar waves regimes. For each of these regimes, similarity between the full-size facility and the scaled-down modeled was assessed with: different wall boundary conditions; different thermally

stratified fields as inputs.

The results of the non-isothermal sloshing analysis reveal that the scaling approach adopted in Chapter 3 is not adequate for the chaotic sloshing regime since it relies too heavily on the liquid being the driving force for the thermal mixing. High amplitude waves are observed in the chaotic regime, which interact directly with the warmer container walls, hence adding complexity the heat transfer mechanisms that take place in the system. Moreover, strong convective fluxes are also observed in the gas, which further contribute to the thermal mixing effect. Thus, the small-scale simulations revealed a greater sensitivity towards the presence of warm walls in the container.

The results of the planar waves simulations show that when adiabatic conditions are used for the container's side walls, the thermodynamic evolution of the system is similar between the full-size facility and the scaled-down model. Due to the sloshing-induced thermal mixing, the pressure decreased $\approx$ 6% in H2 tank and $\approx$ 12% in the N2 sloshing cell. For both these cases, a continuous cooling of the ullage was observed throughout the duration of the excitation. This is attributed to the fact that, for these conditions, the scaling approach takes into account the driving mechanisms for the thermal mixing (i.e. mixing between the warmer interface and the colder liquid from the bulk). However, when the fixed temperature boundary conditions are considered in the small-scale sloshing cell, the similarity is negatively affect and the effect of the warmer walls dominates the problem.

6.2 Future work

The work performed in this master thesis should be further developed by incorporating the effect of the solid walls and the gas into the scaling approach. Moreover, the computational modeling should be extended in order to account for conjugate heat transfer between the fluid phases, the solid walls and any exterior heat fluxes which might be present.

Another aspect which should be considered is the modeling of mass transfer effects between the liquid and the vapour in order to obtain a more complete understanding of the thermodynamic evolution of the system, namely the pressure drop.

Bibliography

[1] Peter Fortescue and John Stark. *Spacecraft Systems Engineering*, volume 3. Wiley, 2003.

[2] Encyclopedia Astronautica. Saturn V. http://www.astronautix.com/s/saturnv.html. Accessed: 2020-03-28.

[3] Encyclopedia Astronautica. Ariane 5 ECA. http://www.astronautix.com/a/ariane5eca.html. Accessed: 2020-03-28.

[4] Encyclopedia Astronautica. Atlas V. http://www.astronautix.com/a/atlasv.html. Accessed: 2020-03-28.

[5] Encyclopedia Astronautica. Space shuttle. http://www.astronautix.com/s/spaceshuttle.html. Accessed: 2020-03-28.

[6] Qingzhao Li, Baiquan Lin, Huaming Dai, and Shuai Zhao. Explosion characteristics of h2/ch4/air and ch4/coal dust/air mixtures. *Powder Technology*, 229:222 – 228, 2012.

[7] Michael Dreyer. Propellant behavior in launcher tanks: an overview of the compere program. *EUCASS Proceedings Series*, 1:253–266, September 2009.

[8] Tim Arndt. *Sloshing of Cryogenic Liquids in a Cylindrical Tank under normal Gravity Conditions*. PhD thesis, Bremen Univseristy, 2011.

[9] Paul Fjeld. The First Lunar Landing. https://www.hq.nasa.gov/alsj/a11/a11.landing.html. Accessed: 2020-05-12.

[10] Space Launch Report. SpaceX Falcon Data Sheet. https://www.spacelaunchreport.com/falcon.html. Accessed: 2020-05-12.

[11] Charlotte Hoppe. LH2 Tank performance analysis. *KTH Vetenskap och Konst*, 2013.

[12] Philipp Behruzi and Mark Michaelis. Behavior of the cryogenic propellant tanks during the first flight of the ariane 5 esc-a upper stage. July 2006.

[13] Christophe Montsarrat. Fluid motion analysis in the cryogenic tanks of the upper stage of Ariane 5 during the ascent phase. *KTH Vetenskap och Konst*, 2017.

[14] J. Lacapere, B. Vieille, and B. Legrand. Experimental and numerical results of sloshing with cryogenic fluids. 1, 2009.

[15] Takehiro Himeno, Daizo Sugimori, Katsutoshi Ishikawa, and Yutaka Umemura. Heat Exchange and Pressure Drop Enhanced by Sloshing. pages 1–40, 2011.

[16] Martin Konopka, Philipp Behruzi, Sebastian Schmitt, and Michael Dreyer. Phase change in cryogenic upper stage tanks. July 2014.

[17] Sebastian Schmitt. *Experimental and Numerical Investigations of Two-Phase Flow with Non-Isothermal Boundary Conditions under Microgravity Conditions*. PhD thesis, Bremen University, 2017.

[18] Helmut F. Bauer. *Fluid oscillations in the containers of a space vehicle and their influence upon stability*. NASA, Huntsville, Alabama, 1964.

[19] H. Norman Abramson, Franklin T. Dodge, Helmut F. Bauer, George W. Brooks, Wen-Hwa Chu, John F. Dalzell, Daniel D. Kana, William C. Reynolds, Hugh M. Satterlee, and Sandor Silverman. *The Dynamic Behavior of Liquids in Moving Containers*. NASA, 1966.

[20] John W. Miles. Resonantly forced surface waves in a circular cylinder. *Journal of Fluid Mechanics*, 149:15–31, 1984.

[21] Matthew E Moran, Nancy B Mcnelis, Maureen T Kudlac, Mark S Haberbusch, Brook Park, and George A Satomino. Experimental Results of Hydrogen Slosh in a 62 Cubic Foot (1750 Liter) Tank. 1994.

[22] Arnold Van Foreest. Modeling of cryogenic sloshing including heat and mass transfer. (July):1–20, 2010.

[23] André Da and Luz Moreira. Comparison between CFD and experimental results of the sloshing rising wave in a microgravity environment. Master's thesis, Linköping University, 2019.

[24] M. Hansinger. Numerical simulation of cryogenic fuel in simplified space propulsion reservoir. *von Karman Institute for Fluid Dynamics, Project Report 2016-14*, 2016.

[25] Matthäus Jäger. Fuel tank sloshing simulation using the finite volume method. M(July), 2019.

[26] Juan Agui and Jeffrey Moder. Modeling of non-isothermal cryogenic fluid sloshing. July 2015.

[27] O. Kartuzova and M. Kassemi. Validation of a Cfd Model Predicting the Effect of High Level Pressure Drop in a Small-Scale Tank in Normal Gravity. pages 1–21, 2018.

[28] Frank M. White. *Fluid mechanics*. University of Rhode Island, 4 edition, 1998.

[29] Tobias Holzmann. *Mathematics, Numerics, Derivations and OpenFOAM®*. November 2019.

[30] Hiroaki Nishikawa. *I do like CFD, VOL.1: Governing Equations and Exact Solutions*. February 2017.

[31] Michael E. Dreyer. *Free Surface Flows under Compensated Gravity Conditions*, volume 221. Springer, Bremen, 2003.

[32] Edwin N. Lightfoot R. Byron Bird, Warren E. Stewart. *Transport Phenomena*, volume Revised 2nd Edition. John Wiley and Sons, Inc, 2006.

[33] Frank P. Incropera, David P. Dewitt, Theodore L. Bergman, and Adrienne S. Lavine. *Fundamentals of Heat and Mass Transfer*. John Wiley & Sons, Los Angeles, California, 6th edition, 207.

[34] Michael J. Moran, N. Shapiro, Howard, Daisie D. Boettner, and Margaret B. Bailey. *Fundamentals of Engineering Thermodynamics*, volume 53. John Wiley & Sons, 7 edition, 2011.

[35] Thomas A Lance. Analysis of Propellant Slosh Dynamics and Generation of an Equivalent Mechanical Model for Use in Preliminary Voyager Autopilor Design Studies. *National Aeronautics and Space Administration*, Technical(No. 33-306), 1966.

[36] Raouf A. Ibrahim. *Liquid sloshing dynamics*. 2005.

[37] Michael Dreyer. Propellant behavior in launcher tanks: an overview of the compere program. *EUCASS Proceedings Series*, 1:253–266, September 2009.

[38] Jiann-Woei (Jimmy) Jang, Abran Alaniz, Lee Yang, Joseph Powers, and Charles Hall. Mechanical slosh models for rocket-propelled spacecraft. August 2013.

[39] Marta Lazzarin, Marco Manente, Daniele Pavarin, Alberto Bettella, and Roberto Da Forno. Analytical sloshing model and cfd analysis for the exomars mission. July 2013.

[40] I. E. Sumner. Experimental investigation of stability boundaries for planar and nonplanar sloshing in spherical tanks. January 1966.

[41] Aude Royon-Lebeaud, Emil Hopfinger, and Alain Cartellier. Liquid sloshing and wave breaking in cylindrical and square-base containers. *Journal of Fluid Mechanics*, 577:467 – 494, April 2007.

[42] M. Ruzicka. On dimensionless numbers. *Chemical Engineering Research and Design*, 86:835–868, August 2008.

[43] Nikolai Kulev, Steffen Basting, Eberhard Bänsch, and Michael Dreyer. Interface reorientation of cryogenic liquids under non-isothermal boundary conditions. *Cryogenics*, 62:48–59, 2014.

[44] Malte Stief, Jens Gerstmann, and Michael E. Dreyer. Reorientation of Cryogenic Fluids Upon Step Reduction of Gravity. *Pamm*, 5:553–554, 2005.

[45] Zhan Liu, Yuyang Feng, Gang Lei, and Yanzhong Li. Fluid thermal stratification in a non-isothermal liquid hydrogen tank under sloshing excitation. *International Journal of Hydrogen Energy*, 43(50):22622–22635, 2018.

[46] Arianespace. Ariane 5 User's Manual. (5 Revision 2), 2016.

[47] Lei Wang, Tian Yan, Jiaojiao Wang, Shixuan Ye, Yanzhong Li, Rui Zhuan, and Bin Wang. CFD investigation on thermodynamic characteristics in liquid hydrogen tank during successive varied-gravity conditions. *Cryogenics*, 103(January):102973, 2019.

[48] Tim Arndt and Michael Dreyer. Damping behavior of sloshing liquid in laterally excited cylindrical propellant vessels. *Journal of Spacecraft and Rockets*, 45(5):1085–1088, 2008.

[49] Siderius D.W. Krekelberg W.P. Shen, V.K. and H.W. Hatch. *NIST Standard Reference Database Number 173, National Institute of Standards and Technology, Gaithersburg MD, 20899*, volume 3. NIST Standard Reference Simulation Website, Retrieved: 2020-05-21.

[50] Michael H. Rausch, Lorenz Kretschmer, Stefan Will, Alfred Leipertz, and Andreas P. Fröba. Density, surface tension, and kinematic viscosity of hydrofluoroethers HFE-7000, HFE-7100, HFE-7200, HFE-7300, and HFE-7500. *Journal of Chemical and Engineering Data*, 60(12):3759–3765, 2015.

[51] C.W Hirt and B.D Nichols. Volume of fluid (vof) method for the dynamics of free boundaries. *Journal of Computational Physics*, 39(1):201 – 225, 1981.

[52] Silje Kreken Almeland. Implementation of an air-entrainment model in interFoam. 2018.

[53] Santiago Márquez Damiáno. An extended mixture model for the simultaneous treatment of small-scale and large-scale interfaces. *International Journal for Numerical Methods in Fluids*, (75):547–574, 2014.

[54] J.U Brackbill, D.B Kothe, and C Zemach. A continuum method for modeling surface tension. *Journal of Computational Physics*, 100(2):335 – 354, 1992.

[55] Henrik Rusche. Computational Dispersed Two-Phase Dynamics Flows of At Phase Fractions. (December 2002), 2003.

[56] Bjarke Eltard Larsen, David R. Fuhrman, and Johan Roenby. Performance of interFoam on the simulation of progressive waves. *Coastal Engineering Journal*, 61(3):380–400, 2019.

[57] Steven T Zalesak. Fully multidimensional flux-corrected transport algorithms for fluids. *Journal of Computational Physics*, 31(3):335 – 362, 1979.

[58] OpenCFD Ltd. OpenFOAM: User Guide v1912. `https://www.openfoam.com/documentation/guides/latest/doc/guide-fos-field-CourantNo.html`. Accessed: 2020-06-29.

[59] H. K. Versteeg and W. Malalasekera. *An Introduction to Computational Fluid Dynamics: The Finite Volume Method*, volume 2nd Edition. Harlow, England: Pearson Education Ltd, 2007.

[60] Heng Jin, Yong Liu, Huajun Li, and Qiang Fu. Numerical analysis of the flow field in a sloshing tank with a horizontal perforated plate. *Journal of Ocean University of China*, 16(4):575–584, 2017.

[61] Jacco H. Snoeijer and Bruno Andreotti. Moving Contact Lines: Scales, Regimes, and Dynamical Transitions. *Annual Review of Fluid Mechanics*, 45(1):269–292, 2013.

[62] Chun Huh and L.E Scriven. Hydrodynamic model of steady movement of a solid/liquid/fluid contact line. *Journal of Colloid and Interface Science*, 35(1):85 – 101, 1971.

[63] Hanna. Holmgren, Gunilla. Kreiss, Stefan. Turek, and Uppsala universitet. Teknisk-naturvetenskapliga vetenskapsomradet. *Modelling of Moving Contact Lines in Two-Phase Flows*. 2017.

[64] M.K. Andrews and P.D. Harris. Damping and gas viscosity measurements using a microstructure. *Sensors and Actuators A: Physical*, 49(1):103 – 108, 1995.

[65] L. Bocquet. Slipping of a fluid on a surface of controlled roughness. *C. R. Acad. Sci.*, 316:7 – 12, 1993.

[66] D. Legendre and M. Maglio. Comparison between numerical models for the simulation of moving contact lines. *Computers and Fluids*, 113:2–13, 2015.

[67] Ren Weiqing and E. Weinan. Boundary conditions for the moving contact line problem. *Physics of Fluids*, 19(2), 2007.

[68] Sopheak Seng, Charles Monroy, and Sime Malenica. On the use of Euler and Crank-Nicolson time-stepping schemes for seakeeping simulations in OpenFOAM. May 2017.

[69] M Jadidi, Moussa Tembely, Sara Moghtadernejad, and Ali Dolatabadi. Coupled Level Set and Volume of Fluid method in OpenFoam with application to compressible two-phase flow. *22nd Annual Conference of the CFD Society of Canada*, (September 2015), 2014.

Appendices

Appendix A

Theoretical derivations

A.1 Constitutive relation for incompressible fluids

For incompressible Newtonian fluids, the shear stress tensor can be expressed through Equation A.1 [29]. This expression is the 'constitutive relation' that relates local velocity gradients in the flow with the fluid's dynamic viscosity, μ.

$$\mathbb{T} = \mu \left[\nabla \otimes \mathbf{u} + (\nabla \otimes \mathbf{u})^T \right] = \mu \begin{bmatrix} 2\frac{\partial u_x}{\partial x} & \frac{\partial u_y}{\partial x} + \frac{\partial u_x}{\partial y} & \frac{\partial u_z}{\partial x} + \frac{\partial u_x}{\partial z} \\ \frac{\partial u_x}{\partial y} + \frac{\partial u_y}{\partial x} & 2\frac{\partial u_y}{\partial y} & \frac{\partial u_z}{\partial y} + \frac{\partial u_y}{\partial z} \\ \frac{\partial u_x}{\partial z} + \frac{\partial u_z}{\partial x} & \frac{\partial u_y}{\partial z} + \frac{\partial u_z}{\partial y} & 2\frac{\partial u_z}{\partial z} \end{bmatrix} \tag{A.1}$$

If the dynamic viscosity is constant in space, the shear stress term can be developed by applying the divergence operator on the tensor field [29, 30].

$$\nabla \cdot \mathbb{T} = \mu \begin{bmatrix} 2\frac{\partial^2 u_x}{\partial x^2} + \frac{\partial}{\partial y}\left(\frac{\partial u_y}{\partial x} + \frac{\partial u_x}{\partial y}\right) + \frac{\partial}{\partial z}\left(\frac{\partial u_z}{\partial x} + \frac{\partial u_x}{\partial z}\right) \\ \frac{\partial}{\partial x}\left(\frac{\partial u_x}{\partial y} + \frac{\partial u_y}{\partial x}\right) + 2\frac{\partial^2 u_y}{\partial y^2} + \frac{\partial}{\partial z}\left(\frac{\partial u_z}{\partial y} + \frac{\partial u_y}{\partial z}\right) \\ \frac{\partial}{\partial x}\left(\frac{\partial u_x}{\partial z} + \frac{\partial u_z}{\partial x}\right) + \frac{\partial}{\partial y}\left(\frac{\partial u_y}{\partial z} + \frac{\partial u_z}{\partial y}\right) + 2\frac{\partial^2 u_z}{\partial z^2} \end{bmatrix} \tag{A.2}$$

Developing the terms above for an incompressible fluid, where $\nabla \cdot \mathbf{u} = 0$, leads to the vectorial Laplacian shown in Equation A.3.

$$\nabla \cdot \mathbb{T} = \mu \begin{bmatrix} \frac{\partial^2 u_x}{\partial x^2} + \frac{\partial^2 u_x}{\partial y^2} + \frac{\partial^2 u_x}{\partial z^2} \\ \frac{\partial^2 u_y}{\partial x^2} + \frac{\partial^2 u_y}{\partial y^2} + \frac{\partial^2 u_y}{\partial z^2} \\ \frac{\partial^2 u_z}{\partial x^2} + \frac{\partial^2 u_z}{\partial y^2} + \frac{\partial^2 u_z}{\partial z^2} \end{bmatrix} = \mu \nabla^2 \mathbf{u} \tag{A.3}$$

A.2 Linearised potential equation of motion

This section contains the derivation of the linearised equation of motion for potential flow based on the approach from Ibrahim (2005) [36] and Lance (1966) [35]. Neglecting the viscous term, the momentum

balance from Equation 2.5 is simplified into:

$$\rho\left(\frac{\partial \mathbf{u}}{\partial t} + \mathbf{u}(\nabla \cdot \mathbf{u})\right) = -\nabla p + \rho \mathbf{g}. \tag{A.4}$$

Consider the decomposition of the total fluid velocity, $\mathbf{u}$, such that:

$$\mathbf{u} = \tilde{\mathbf{u}} + \mathbf{U_0}. \tag{A.5}$$

Where $\tilde{\mathbf{u}}$ is the fluid velocity with respect to the moving container, and $\mathbf{U_0} = \dot{X}_0 \mathbf{e_x}$ is the container velocity relative to the inertial reference frame. The material derivative is developed taking this decomposition into account:

$$\frac{\mathrm{D}\mathbf{u}}{\mathrm{D}t} = \frac{\mathrm{D}\tilde{\mathbf{u}}}{\mathrm{D}t} + \frac{\mathrm{D}\mathbf{U_0}}{\mathrm{D}t} = \frac{\partial \tilde{\mathbf{u}}}{\partial t} + (\tilde{\mathbf{u}} \cdot \nabla)\tilde{\mathbf{u}} + \frac{d\mathbf{U_0}}{dt}. \tag{A.6}$$

The convective term is neglected due to assumptions (1) and (4):

$$\tilde{\mathbf{u}}(\nabla \cdot \tilde{\mathbf{u}}) = \underbrace{\frac{1}{2}\nabla(\tilde{\mathbf{u}} \cdot \tilde{\mathbf{u}})}_{\text{=0, 2nd order term}} - \underbrace{\tilde{\mathbf{u}} \times (\nabla \times \tilde{\mathbf{u}})}_{\text{=0, irrotational flow}} \approx 0. \tag{A.7}$$

Thus, combining Equations A.4, A.6 and A.7 results in:

$$\frac{\partial \tilde{\mathbf{u}}}{\partial t} + \frac{d\mathbf{U}_0}{dt} = -\frac{1}{\rho}\nabla p + \mathbf{g}. \tag{A.8}$$

The introduction of the potential function to describe the local fluid velocity, $\tilde{u}$, leads to:

$$\nabla\frac{\partial \Phi}{\partial t} + \frac{d\mathbf{U}_0}{dt} = -\frac{1}{\rho}\nabla p + \mathbf{g}. \tag{A.9}$$

Now, noticing that the container and gravitational accelerations can, respectively, be written as $d\mathbf{U}_0/dt = \nabla(\ddot{X}_0 x)$, and $\mathbf{g} = \nabla(gz)$, Equation A.9 is rewritten as:

$$\nabla\left(\frac{\partial \Phi}{\partial t} + \ddot{X}_0 x + \frac{p}{\rho} - gz\right) = 0 \tag{A.10}$$

Equation A.10 is always satisfied provided that the terms inside the brackets are invariant in space. As a result, they should be equal to a certain function of time, $C(t)$.

$$\frac{\partial \Phi}{\partial t} + \ddot{X}_0 x + \frac{1}{\rho}\nabla p - gz = C(t) \tag{A.11}$$

Absorbing this temporal function in the definition of the velocity potential leads to the linearised equation of motion for lateral sloshing (Equation A.12).

$$\frac{\partial \Phi}{\partial t} + \frac{p}{\rho} - gz + \ddot{X}_0 x = 0. \tag{A.12}$$

Given the shape of the container, cylindrical coordinates are used. As a result, by setting $x = r\cos(\theta)$

Equation 2.19 is obtained.

$$\frac{\partial \Phi}{\partial t} + \frac{p}{\rho} - gz + \ddot{X}_0 r\cos(\theta) = 0 \tag{A.13}$$

A.3 Natural frequency derivation

The natural frequencies are determined by studying the equation of motion of the free surface without external excitations, $\ddot{X}_0 = 0$. For this, consider Equation 2.19 written around the originally undisturbed surface, at $z = 0$.

$$\left(\frac{\partial \Phi}{\partial t} + \frac{p}{\rho}\right)_{z=0} - g\eta = 0 \tag{A.14}$$

Where η is the free surface displacement with respect to the originally undisturbed interface. At the free surface, the fluid pressure can be considered equal to the vapour pressure if surface tension effects are neglected (i.e. $p_{\text{liq}} = p_{\text{gas}}$). However, if surface tension effects are present, the Young-Laplace equation must be introduced in order to account for the pressure difference between the liquid and vapour phases [31].

$$\left(\frac{\partial \Phi}{\partial t} - \frac{\sigma\kappa}{\rho}\right)_{z=0} - g\eta = 0 \tag{A.15}$$

Consider now the free surface boundary condition, $\partial z/\partial t = -\left(\partial\Phi/\partial z\right)_{z=0}$ and differentiate Equation A.15 with respect to time:

$$\left(\frac{\partial^2 \Phi}{\partial t^2} - \frac{\sigma}{\rho}\frac{\partial \kappa}{\partial t} + g\frac{\partial \Phi}{\partial z}\right)_{z=0} = 0. \tag{A.16}$$

According to the work of Ibrahim (2005) [36], the temporal derivative of the free surface curvature is given by:

$$\frac{\partial \kappa}{\partial t} = \left(\frac{\partial^3 \Phi}{\partial z^3}\right)_{z=0}. \tag{A.17}$$

Thus, the free surface kinematic condition is given by Equation A.18.

$$\left(\frac{\partial^2 \Phi}{\partial t^2} + \frac{\sigma}{\rho}\frac{\partial^3 \Phi}{\partial z^3} + g\frac{\partial \Phi}{\partial z}\right)_{z=0} = 0 \tag{A.18}$$

Assuming a harmonic shape for the velocity potential function, $\Phi \sim \Phi e^{i\omega t}$, the equation above is solved directly to find the free surface natural frequencies.

$$\omega_{mn}^2 = \left(\frac{g\xi_{mn}}{R} + \frac{\sigma}{\rho}\frac{\xi_{mn}^3}{R^3}\right)\tanh\left(\frac{\xi_{mn}h}{R}\right) \tag{A.19}$$

A.4 Forced lateral sloshing potential function

For forced lateral excitation conditions, the velocity potential function can be assumed to be of the form $\Phi(r,\theta,z,t) \sim \Phi(r,\theta,z)e^{i\Omega t}$, where Ω is the imposed oscillation frequency.

$$\Phi(r,\theta,z,t) = \sum_{n=1}^{\infty} \alpha_{mn}\cos(m\theta)J_m\left(\frac{\xi_{mn}r}{R}\right)\frac{\cosh\left[\xi_{mn}(z+h)/R\right]}{\cosh\left(\xi_{mn}h/R\right)}e^{i\Omega t} \tag{A.20}$$

The free surface kinematic condition is written identically to Equation A.16, with the addition of the forced oscillation term on the right hand side of the equation:

$$\left(\frac{\partial^2\Phi}{\partial t^2} + \frac{\sigma}{\rho}\frac{\partial^3\Phi}{\partial z^3} + g\frac{\partial\Phi}{\partial z}\right)_{z=0} = -\dddot{X}_0 r\cos(\theta). \tag{A.21}$$

Where $\dddot{X}_0 = -A_0\Omega^3\cos(\Omega t)$. Then, combining Equations A.20 and A.21 leads to:

$$\sum_{n=1}^{\infty}(\omega_{mn}^2 - \Omega^2)\alpha_{mn}\cos(m\theta)J_m\left(\frac{\xi_{mn}r}{R}\right)\cos(\Omega t) = A_0\Omega^3\cos(\Omega t)r\cos(\theta). \tag{A.22}$$

Equation A.22 can be solved to determine the modal amplitude α_{mn} for $m = 1$. This is done by expanding the radial coordinate, r, through a Bessel series, as is shown in Equation A.23 [18, 35]:

$$r = \sum_{n=1}^{\infty}\frac{2R}{(\xi_{1n}^2 - 1)}\frac{J_1\left(\xi_{1n}r/R\right)}{J_1\left(\xi_{1n}\right)} \tag{A.23}$$

Thus, the potential amplitude for the first sloshing mode $m = 1$ is given by:

$$\alpha_{1n} = \frac{2R}{(\xi_{1n}^2 - 1)J_1(\xi_{1n})}\frac{A_0\Omega^3}{(\omega_{1n}^2 - \Omega^2)}. \tag{A.24}$$

Finally, the complete expression for the velocity potential of the first asymmetrical sloshing mode is provided in Equation A.25.

$$\Phi(r,\theta,z,t) = \sum_{n=1}^{\infty}\frac{2R}{(\xi_{1n}^2 - 1)}\frac{A_0\Omega^3}{(\omega_{1n}^2 - \Omega^2)}\frac{J_1(\xi_{1n}r/R)}{J_1(\xi_{1n})}\frac{\cosh\left[\xi_{1n}(z+h)/R\right]}{\cosh\left(\xi_{1n}h/R\right)}\cos(\theta)\cos(\Omega t) \tag{A.25}$$

Appendix B

Numerical algorithms

B.1 The interFoam algorithm in OpenFOAM

Algorithm 1 `interFoam` solver algorithm in `OpenFOAM-v1912`

1. Create fields for the initial flow conditions
2. Start runtime loop
   (a) Update solution time
   (b) Update mesh (if using dynamic mesh)
   (c) Correct cell face fluxes for the new mesh
3. **PIMPLE loop** until `nOuterCorrectors` iterations are performed. This loop combines the SIMPLE (SIMPLEC) and PISO algorithms in order to solve the pressure-velocity coupling problem that is characteristic of incompressible fluids [29].
   (a) Solve α equation with the MULES scheme
   (b) Update mixture properties for the α field (density and kinematic viscosity)
   (c) If `momentumPredictor` option is enabled, solve the momentum predictor equation to obtain a new momentum-satisfying velocity field
4. **PISO loop** until `nCorrectors` iterations are performed.
   (a) Solve pressure correction equation for `nOrthogonalCorrectors` iterations. The purpose of this step is to correct for non-orthogonality in the numerical grid.
   (b) Correct pressure field
   (c) Correct cell face fluxes based on the new pressure field
   (d) Correct turbulence properties
5. Return to Step (2.a) until the final solution time is reached

B.2 The compressibleInterDyMFoam solver

The pressure-based `compressibleInterDyMFoam` solver handles compressibility effects in the flow through Equation B.1.

$$\rho_{\mathrm{i}} = \rho_{\mathrm{i},0} + \psi_{\mathrm{i}} p \tag{B.1}$$

Where $\rho_{i,0}$ is the nominal density of phase *i*, and $\psi_\mathrm{i} = (RT)_\mathrm{i}^{-1}$. The ideal gas law is obtained by setting $\rho_{i,0} = 0$ [69]. The compressible volumetric phase fraction advection equation for phase *i* is given by:

$$\frac{D}{Dt}(\rho_\mathrm{i}\alpha_\mathrm{i}) = \frac{\partial \rho_\mathrm{i}\alpha_\mathrm{i}}{\partial t} + \nabla \cdot (\rho_\mathrm{i}\alpha_\mathrm{i}\mathbf{u}) = 0. \tag{B.2}$$

Splitting the terms inside the material derivative with the product rule yields Equation B.3, which is the volumetric phase fraction advection equation solved by OpenFOAM:

$$\frac{\partial \alpha_\mathrm{i}}{\partial t} + \nabla \cdot (\alpha_\mathrm{i} U_i) = -\frac{\alpha_\mathrm{i}}{\rho_\mathrm{i}} \cdot \frac{D\rho_\mathrm{i}}{Dt} \tag{B.3}$$

$$\frac{D\rho_\mathrm{i}}{Dt} = \psi_\mathrm{i} \frac{Dp}{Dt} \tag{B.4}$$

Inserting Equation B.4 in B.3 yields:

$$\frac{\partial \alpha_\mathrm{i}}{\partial t} + \nabla \cdot (\alpha_\mathrm{i}\mathbf{u}) = -\frac{\alpha_\mathrm{i}\psi_\mathrm{i}}{\rho_\mathrm{i}} \cdot \frac{Dp}{Dt} \tag{B.5}$$

Summing Equation B.5 for α_1 and α_2:

$$\frac{D}{Dt}(\alpha_1 + \alpha_2) + (\alpha_1 + \alpha_2)\nabla \mathbf{u} = -\left(\frac{\alpha_1\psi_\mathrm{i}}{\rho_1} + \frac{\alpha_2\psi_\mathrm{i}}{\rho_2}\right) \cdot \frac{Dp}{Dt} \tag{B.6}$$

Recalling that for a two-phase flow $\alpha_1 + \alpha_2 = 1$, the mass conservation equation solved by OpenFOAM is obtained:

$$\nabla \mathbf{u} = -\left(\frac{\alpha_1\psi_\mathrm{i}}{\rho_1} + \frac{\alpha_2\psi_\mathrm{i}}{\rho_2}\right) \frac{Dp}{Dt} \tag{B.7}$$

Then, keeping this result in mind, the volumetric-phase-fraction advection equation that is solved is the following:

$$\frac{\partial \alpha_1}{\partial t} + \nabla(\alpha_1\mathbf{u}) + \nabla(\alpha_1(1-\alpha_1)\mathbf{u}_r) = \alpha_1(1-\alpha_1)\left(\frac{\psi_2}{\rho_2} - \frac{\psi_1}{\rho_1}\right)\frac{\mathrm{D}p}{\mathrm{D}t} + \alpha_1\nabla\mathbf{u}. \tag{B.8}$$